Carbon Nanotube and Carbon Fibre Based Radiation Dosimetry

by

Jiazhi Ma

A thesis
presented to the University of Waterloo
in fulfilment of the
thesis requirement for the degree of
Doctor of Philosophy
in
Systems Design Engineering

Waterloo, Ontario, Canada, 2008

I hereby declare that I am the sole author of this thesis. This is a true copy of the thesis, including any required final revisions, as accepted by my examiners.

I understand that my thesis may be made electronically available to the public.

Abstract

The principle of radiobiology and, hence, clinical outcomes in radiotherapy are inherently dependent on accurate radiation dosimetry. Over the last few decades, ionization chambers, thermoluminescence dosimeters (TLDs), film dosimeters, and semiconducting dosimeters have been commonly used in radiotherapy. However, the shortcomings of each type of dosimeter limit their applications for *in vivo* radiation measurements for provision of accurate and precise dosimetric information in real-time. The objective of this thesis is to explore a new generation of radiation dosimeters by using state-of-the-art nanomaterials and technologies to realize real-time monitoring of dose delivery in radiotherapy.

This thesis investigates the use of carbon nanotubes (CNTs) and carbon fibres as sensing materials for dosimetric measurements. First, a parallel plate ionization chamber with CNT electrodes was designed to study the ionization collection efficiency of the CNTs. The prototype chamber had two stainless steel electrodes, which were customized to accommodate the CNT samples. Experiments, such as saturation characteristics, linearity, and electrode separation, were performed to characterize the prototype chamber. Secondly, dosimeters based on the resistance change of CNTs and carbon fibres were studied. The proposed dosimeters, based on carbon fibre sheets and CNT films, were designed and fabricated. Dose rate, dose, and field size measurements were carried out to evaluate these novel dosimeters that were able to provide dose rate and dose information at the same time. Thirdly, a transparent and flexible CNT-based film dosimeter was investigated. The flexible dosimeter can perform dosimetric measurements when it was bent to fit the curvature of the measured

surface. Finally, a dosimeter array system, consisting of a CNT-based film dosimeter array, a readout circuit, and user interface software, was designed and implemented. The array with the parallel electrode structure and a 3×3 mm^2 sensing area for each pixel provided good signal responses. The array system displayed excellent repeatability in the measurements.

Acknowledgments

First, I would like to express my deep gratitude to my supervisor, Dr. John Yeow, and co-supervisor, Dr. Rob Barnett, for their boundless insight, invaluable guidance, and continuous encouragement. My sincere appreciation also goes to Dr. James Chow for his inspiring discussions. He has always been available and supportive. Without them, this work would not have been possible.

I would like to thank my Ph.D advisory committee members, Dr. Keith Hipel, Dr. Eihab Abdel-Rahman, and Dr. William Melek, for their valuable advices and helpful suggestions for my research. I am also grateful to Dr. Kevin Jordan for serving as the external examiner.

My acknowledgement of the team members of the Biomems lab is important. I am specially thank Jethro Ma for helping the readout circuit and software implementation, Yanhui Bai for assisting the array electrode fabrication, and Dr. Runqing Jiang and Physicist Andre Fleck from the Grand River Regional Cancer Centre for helpful discussions. I would like to extend my appreciation to the graduate coordinator, Ms. Vicky Lawrence, for her kindness and help.

I would like to acknowledge the funding agencies from the Natural Science and Engineering Research Council of Canada (NSERC), Ontario Centres of Excellence (OCE), Ontario Graduate Scholarship (OGS), University of Waterloo President's Scholarship, and Grand River Regional Cancer Centre.

Last but not least, I would like to thank my husband and my parents for their continuous love and support, which kept me motivated to reach my goals.

Dedication

To

my beloved family...

Contents

List of Figures

List of Tables

Chapter 1

Introduction

1.1 Background

Cancer is a public health problem worldwide. According to the World Health Organization (WHO), every year, more than 10 million people are diagnosed with cancer. Radiation therapy, also called radiotherapy, is one of the most effective methods in cancer treatment. Radiotherapy is a clinical process that uses ionizing radiation such as x-rays and gamma rays for the treatment to eradicate or slow down the growth of cancer cells [1]. In radiotherapy, the dose of radiation must be accurately and precisely delivered: insufficient dosages can impact the efficiency and outcome of the radiotherapy, leading to a recurrence of the disease, and excessive dosages can damage healthy tissues, resulting in unacceptable side effects and long-term complications.

Ionizing radiation is generally administrated to radiation oncology patients using three techniques: external beam, brachytherapy, and systemic injection. External beam radiotherapy is the most common form of radiotherapy for the treatment of cancer. During this procedure, radiation source is at a fixed distance

from the patient, and the target within the patient is irradiated with an external radiation beam [2]. In brachytherapy, sealed radioactive sources are implanted directly into or near the target volume and deliver a high radiation dose to the tumor with a rapid dose fall-off in the surrounding normal tissue [3]. For the systemic injection technique, soluble radioactive substances are administered to the body by injection. This treatment is less common. Depending on the half-life and initial activity of the radioactivity administered, it can take days or even weeks for the radioactivity to decrease to the point where the patient is not a radiation danger to bystanders [4].

1.2 Research Motivation

The aim of radiotherapy is to deliver a very accurate dose of radiation to a well-defined target volume with minimal damage to the surrounding healthy tissues. Radiation dosimetry plays an important role in verification of prescribed dose. One of the major challenges is to realize accurate and precise real-time dose measurements during the radiation treatment. In the meantime, the effectiveness of the radiation treatments should not be affected by the existence of the dosimeters. For example, radiation beams are attenuated when they pass through the dosimeter. In addition, the scattering and reflection of the radiation due to the existence of the dosimeters can complicate the determination of dose to soft tissues.

Different effects of ionizing radiation in matter have been utilized for the quantification of radiation dosages. Ionization chambers [5], thermoluminescence dosimeters (TLDs) [6], radiographic [7] and radiochromic films [8], and semiconductor silicon diodes and metal-oxide-semiconductor field effect

transistor (MOSFET) dosimeters [9, 10, 11] are four commonly used detectors for radiation dosimetry.

- **Ionization Chambers**: The operation of ionization chambers is based on ionization produced in the active volume. Depending on the physical phase, gas or liquid, of the active volume medium, ionization chambers can be classified as a gas- or liquid-filled. This type of dosimeter offers high sensitivity for absorbed dose measurements. However, the ionization chambers usually require a high bias voltage in order to achieve acceptable ionization collection efficiency. Their large physical size means that they cannot achieve good spatial resolution. Therefore, ionization chambers are not suitable for *in vivo* dosimetry.

- **TLDs**: TLDs are based on the radio-thermoluminescence property of materials. When the materials have previously been exposed to ionizing radiation, light is emitted when the materials are heated. The emitted amount of light is proportional to the irradiated dose. The disadvantages of TLDs include sensitivity to the environmental conditions, handling procedures, and heating conditions. When TLDs are routinely used, their accuracy is low, and information is destroyed during the readout process. Real-time measurements cannot be performed, and no information is given about the dose rate.

- **Film Dosimeters**: Radiographic and radiochromic film dosimeters are usually used as relative dosimeters rather than absolute dosimeters. The operation of film dosimeters depends on a colour change due to the radiosensitive emulsion. The dose of the radiation is related to the darkening of the film, which is referred to as the optical density (OD). For

radiographic films, silver in silver bromide is reduced to metallic silver because of the ionizing radiation. For radiochromic films, the radiochromic material turns blue on irradiation due to a direct polymerization process. One common disadvantage of film dosimeters is their non-linear response to the radiation dose. In addition, radiographic and radiochromic films are not tissue equivalent. Another disadvantage of radiographic films is their radiation energy dependence. The high atomic number of the active material (silver bromide) leads to a distinct over-response to low-energy x-rays. Radiochromic films are self-developing. However it takes several hours for the colour change to stabilize sufficiently for an evaluation. The variation of the OD with time is also temperature dependent and displays an increase in the OD. Ultraviolet (UV) light can cause a colour change of radiochromic films without exposure to ionizing radiation.

- **Semiconducting Dosimeter**: Semiconductor silicon diodes and MOSFET dosimeters are solid-state dosimeters. Typically, they are based on silicon, where the average energy required to produce an electron-hole pair in is smaller than that of air by a factor of 10. Silicon diodes and MOSFET dosimeters are physically small, and can be used for the measurement of the delivered dose in patients by being placed on the patient's skin or within body cavities. However, silicon is not a tissue equivalent material, resulting in a non-linear dose response with radiation quality. The temperature dependency and limited life span of semiconducting dosimeters also limit their applications in clinical environments.

The technology in radiotherapy has been evolving rapidly over the last two decades with the introduction of dynamic multileaf collimation (DMLC), intensity-modulated radiation therapy (IMRT), and image guided radiation therapy (IGRT). The introduction of such techniques pose new challenges for dose measurements. However, the dose measurement techniques are not developing rapidly enough to keep up-to-date with the changes in radiotherapy.

For example, *in vivo* dosimetry is vital for assessing deviations between prescribed and delivered dose for complicated techniques such as IMRT, but current dosimetry systems are limited to measurements with tissue equivalent phantoms or single points on the patient. Although TLDs and film dosimeters can be used for *in vivo* dose measurements [12, 13], the measured results of these dosimeters can be read only after finishing one treatment fraction. No real-time dose delivery information is provided. MOSFET dosimeters can provide real-time signal readouts [14]; however, the dosimeters exhibit a temperature and an energy dependence [15] and are unable to provide two-dimensional (2D) beam distribution profiles [16]. Video-based systems have been used as an additional aid to patient positioning in treatment recently [17, 18, 19, 20], but the record on the external surface of the patient is not very precise, and no dose information is provided.

Therefore, it is essential to develop new technologies, offering accurate and distributed dose monitoring throughout the treatment process to improve the accuracy of the treatment delivery.

1.3 Objectives

The objective of this thesis is to explore a new generation of radiation dosimetry by using state-of-the-art nanomaterials and technologies to realize real-time monitoring of the dose delivery in radiotherapy, which will enable the treatment staff to make timely decisions during the patient treatments. This thesis investigates the use of carbon nanotubes (CNTs) and carbon fibres as sensing materials for dosimetric measurements. Various structures and fabrication processes are studied to evaluate the performance of the proposed dosimeters.

The objectives that the proposed dosimeters should achieve include the following.

- Real-time Dose Monitoring: The signals from the proposed dosimeters can be read from an electrometer or a readout circuit in real-time. Dosimetric information can be accessed immediately as the radiation is being delivered.
- Providing 2D Beam Profile Information: The carbon fibre sheet-based dosimeter and the CNT-based film dosimeter can be fabricated side-by-side to form a dosimeter array. As a result, 2D high-resolution beam profile monitoring can be achieved.
- Low Bias Voltage: The proposed dosimeters should require only a very low bias voltage (not harmful to the human body) to complete the collection of ions and electrons generated by the high-energy radiation beams. The unique physical structure and electrical properties of CNTs allow the proposed dosimeters to be operated in a very low bias voltage.
- Tissue Equivalent: CNTs and carbon fibres consist of carbon atoms with

an atomic number (Z) equal to 6, they could be regarded as tissue equivalent materials (The human body consists of fat, bone, muscle, and critical organs. Approximately 66% of the human body is water. The effective atomic number of water is 7.51).

- Minimum Attenuation to Radiation Beams: The sensing layer of the proposed carbon fibre sheet-based dosimeter and CNT-based film dosimeter is very thin (< 1 mm); the attenuation on the radiation beams due to the existence of such layers is minor. Therefore, the efficiency and effectiveness of the treatment is not reduced significantly, when the proposed dosimeters are implemented for *in vivo* radiation measurements.

- Easy Operation: The handling procedures of the proposed dosimeters are simple and convenient.

- Cost Effective: The materials for the proposed dosimeters, CNTs and carbon fibres, are readily available. The fabrication process of the dosimeters can be completed at room temperature. No clean room environment is required.

1.4 Thesis Organization

This thesis is organized into six chapters, each dealing with a self-contained subject area.

- Chapter 1 describes the motivation, objectives, and organization of the thesis.

- Chapter 2 provides the fundamentals of the underlying physics, treatment machine, and dose measurement technology. Radiation interactions with

matter are introduced, followed by the operation principles and major components of the medical linear accelerator. Radiation detection mechanisms of four types of commonly used dosimeters are also covered.

- Chapter 3 gives relevant details of CNTs to enable a thorough understanding of the methods and results presented in Chapter 4 and 5, respectively. After the synthesis, purification, and properties of the CNTs are presented, the applications, which indicate their potential in radiation dosimetry, are highlighted.

- Chapter 4 contains information on the newly designed and fabricated parallel plate ionization chamber with CNT electrodes. Extensive experiments, including signal saturation characteristics, linearity, and electrode separation, were carried out to characterize the dosimeter. Experimental results with square- and irregular-shaped CNT electrodes are presented and discussed.

- Chapter 5 covers the dosimeters and dosimeter arrays based on resistance change. The design and fabrication of the carbon fibre sheet-based dosimeter, CNT-based film dosimeter, and CNT-based film dosimeter array are presented in detail. The performances of each type of dosimeter are evaluated.

- Chapter 6 summarizes the contributions of this research and suggests future work.

Chapter 2

Background of Radiation Dosimetry

2.1 Introduction

Ionizing radiation is used to eradicate cancer cells as the primary goal of radiotherapy. However, the radiation beams typically traverse normal healthy tissues, when external beam techniques are used. Consequently, the ionizing radiation can damage normal tissue cells and result in unacceptable side effects and long-term complications. A drawing of dose response curves for tumor and normal tissue responses are shown in Fig 2.1 [1].

The solid line in Fig 2.1 indicates the tumor control curve. With the increase of dose, a threshold dose is reached, where tumor eradication is possible. With a further increase in dose, a high possibility of tumor control can be achieved. However, the risk of normal tissue damage also increases. Therefore, the radiation dosage should be delivered to maximize tumor control and minimize normal tissue damage. Also, the dose response curves in Fig 2.1 reflect that the small changes

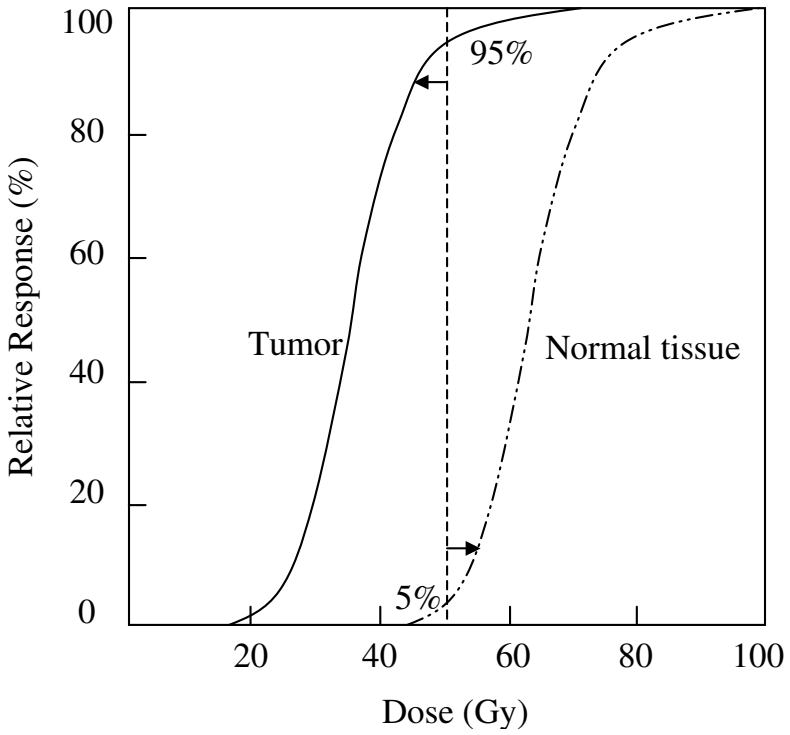

Figure 2.1: Dose response curves for tumor and normal tissue responses [1]

in the dosage will result in significant changes in the tumor and normal tissue responses. Clearly, high accuracy and precision in dose delivery are critical in the cancer treatment.

Radiation dosimetry is a measurement process for determining the energy absorbed per unit mass resulting from the interaction of ionizing radiation with matter. This interaction causes a measurable change in the properties of the matter [21]. The change can be the measured charge (ionization chambers, semiconducting dosimeters), measured light output (TLDs), or visible polymeric chemical reaction (radiochromic films). A brief overview of photon and electron interactions with matter is presented next, which is helpful to understand the

detection mechanism of different types of dosimeters.

2.2 Fundamentals of Radiation Physics

X-ray beams and electron beams, which consist of photons and electrons, respectively, are good examples of ionizing radiation and are widely used in radiotherapy. Thus, it is important to understand the interactions of photons and of electrons with matter.

2.2.1 Photon Interactions with Matter

Attenuation Coefficients

One characteristic of the interactions of a photon beam with matter is that the beam is attenuated due to the absorption or scattering of each individual photon when it passes through matter. The attenuation of the photon beam, ΔN, is proportional to the thickness that photons travel through, Δx, and the initial number of photons, N.

$$\Delta N = -\mu N \Delta x, \tag{2.1}$$

where μ is called the linear attenuation coefficient (cm^{-1}), which is dependent on the density of the matter and the energy of the photons. Generally, the higher the energy of the incident photons and the less dense the matter, the lower the corresponding linear attenuation coefficient is. In this case, upon integrating,

$$N = N_0 e^{-\mu x}. \tag{2.2}$$

Typically, the energy range of photon beams in most medical radiation applications is less than 20 MeV. In this energy range, the interactions of the

photons with matter are mainly due to three processes: (i) photoelectric effect, (ii) Compton scattering, and (iii) pair production.

Photoelectric Effect

In a photoelectric process, a photon of energy $h\nu$ transfers its energy to a bound electron. The kinetic energy of the electron is given by Einstein's photoelectric equation,

$$E = h\nu - E_s, \tag{2.3}$$

where $h\nu$ is the initial photon energy, and E_s is the binding energy of the shell from which the electron is ejected. The atom is left in an excited state and emits characteristic radiation and Auger electrons, as the atom returns to the ground state.

Compton Scattering

A Compton scattering involves an interaction between a photon and an electron. The photon transfers part of its energy to the electron, resulting in the ionization and scattering of the incident photon with degraded energy. When the energy of the photon is between 10 and 100 MeV, most energy is transferred to the electron and very little is scattered. It means that the Compton process decreases with an increase in energy. When the energy of photons is in the range of 100 keV to 10 MeV, Compton scattering is much more important than the photoelectric effect and pair production in soft tissues.

Pair Production

When the energy of incident photons is greater than 1.022 MeV, the absorption of photons occurs through the mechanism of pair production. The production of an electron and positron can take place near the nucleus of the atom or an electron. In the process, no net electronic charge is created. If the photon has an energy greater than 1.022 MeV, the excess energy is shared between the positron and the electron. When the positron combines with a free electron in an annihilation process, two photons, each with 0.511 MeV, are produced.

Fig 2.2 illustrates the processes in which photons interact with matter. The directions of the energy transfer between the photons and electrons are also indicated.

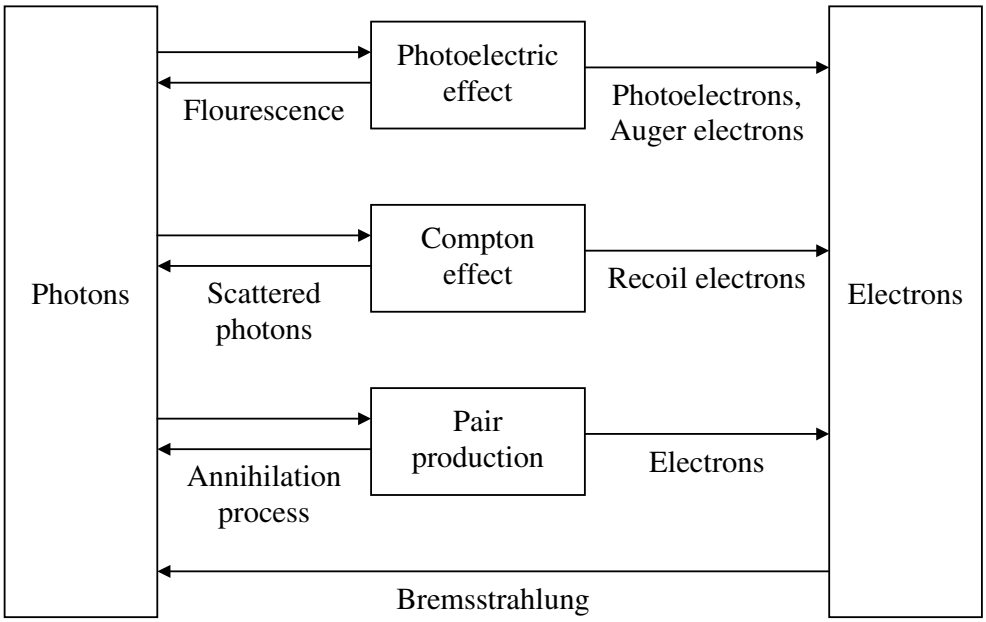

Figure 2.2: Processes in which photons interact with matter

2.2.2 Electron Interactions with Matter

Energy Loss by Collision

When an electron passes through matter, an energy loss occurs because of the interactions with atomic electrons, resulting in either the excitation or ionization of the atom. Since the collisions are between two electrons with the same mass, large energy losses happen due to the significant changes in the directions. The rate of energy loss by this mechanism depends on the electron energy and the ionization energy of the atoms in the medium. When the incident electron transfers a large proportion of the energy to an orbital electron, large energy losses occur.

Energy Loss by Radiation - Bremsstrahlung

Since an electron is a negative charged particle, it may interact with the electric field of the nucleus, when the electron passes close to the nucleus of an atom. The closer the distance between the electron and the nucleus, the stronger the coulomb field. This fact leads to a rapid deceleration of the incident electron. The deceleration of the incident electron is so fast that some of its energy is radiated away as bremsstrahlung. The maximum energy of the bremsstrahlung photon cannot be greater than that of the incident electron, and a spectrum of photon energies below this value is produced.

Electron Stopping Power

The energy transferred from the electron to the medium by collision and radiation is quantified by the use of stopping power, which is defined as the amount of energy that is lost per unit length along the track of the electron , dE/dx. A more useful quantity is the mass stopping power, which makes stopping power

mass independent. The mass stopping power is equal to the energy loss per unit thickness divided by the density of the medium, $(1/\rho)(dE/dx)$. The unit of mass stopping power is MeVcm^2/g. The total mass stopping power is equal to the sum of the mass stopping power by collision, S_{col}, and the mass stopping power by radiation, S_{rad}, and is computed by

$$S_{tot}/\rho = S_{col}/\rho + S_{rad}/\rho. \tag{2.4}$$

2.2.3 Kerma and Absorbed Dose

When photons interact with matter, the photon energy is transferred through a two-step process. First, the energy is transferred to the secondary electrons through various photon interactions, such as photoelectric effect, Compton scattering, and pair production. Secondly, these secondary electrons transfer their energy to the medium through atomic excitation and ionization. The transfer of energy happened in the first step is related to kerma. The energy transfer happened in the second step is related to absorbed dose.

Kerma stands for kinetic energy released in the medium and is defined as the kinetic energy transferred from photons to the electrons, dE_{tr}, in a matter with mass of dm,

$$K = \frac{dE_{tr}}{dm}. \tag{2.5}$$

Absorbed dose is defined as the energy absorbed per unit mass in the volume medium.

$$D = \frac{dE_{ab}}{dm}, \tag{2.6}$$

where dE_{ab} is the energy absorbed in a matter of mass dm.

The unit for kerma and absorbed dose is the same, which is gray (Gy) and defined as joule per kilogram. 1 Gy = 1 J/kg = 100 cGy. The relationship between kerma and absorbed dose is illustrated in Fig 2.3 [22].

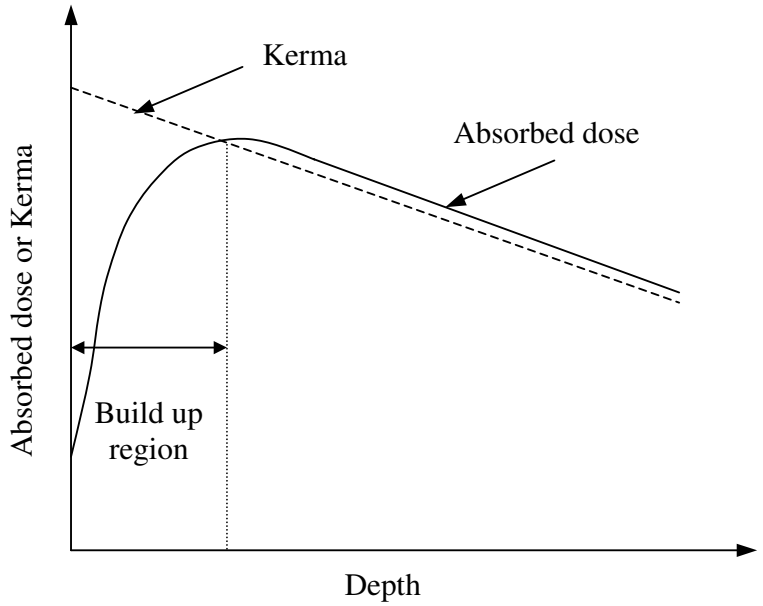

Figure 2.3: Kerma and absorbed dose as a function of depth in an irradiated medium [22]

As shown in Fig 2.3, the kerma has the maximum at the surface of the irradiated medium because the photon intensity is highest at the surface and causes the maximum number of interaction with the medium. As the primary photons interact on their way through the medium, they are attenuated so that the intensity of the photons reduces gradually. The electrons set into motion during the photon interaction at the surface travel a certain distance in depth before their energy is completely absorbed. These electrons add to the ionization produced by the photon interaction occurring at further depths. Therefore, the absorbed dose increases in the build up region before reaching the greatest dose

at the depth of maximum dose, d_{max}. Beyond d_{max}, the absorbed dose decreases gradually. At depth greater than d_{max}, the kerma curve falls below the absorbed dose curve because kerma reflects the photon intensity at each depth, whereas absorbed dose reflects the photon intensity at shallower depths.

2.3 Medical Linear Accelerator

Ionizing radiation at different energy levels is needed in clinical treatments. Usually, kilovoltage radiation beams and electron beams are used for the treatment of superficial skin cancers. Megavoltage photon beams are used to treat tumors that are deep-seated in the human body.

Initially, x-ray beams were produced by conventional x-ray tubes, consisting of anodes and cathodes with a high potential (30 to 150 kV) applied across them. The energy of the x-ray generated by this method is in the kilovoltage level. The kilovoltage radiation beams can be used effectively for the treatment of superficial tumors. However, they do not penetrate enough to treat deep-seated tumors effectively.

In the 1950s, cobalt-60 machines were developed, which can produce megavoltage radiation beams. The beam generated from cobalt-60 machines has two photo-peaks, at 1.17 and 1.33 MeV, which give a mean photon energy of about 1.25 MeV. The maximum dosage is achieved at a 0.5 cm depth [23]. But the beams in this energy level still cannot treat the tumor inside the body without overdose on the patient's surface.

With the appearance of microwave generators, such as magnetrons and klystrons, the modern medical linear accelerator (linac) was developed and has gone through five generations to the present. The first 100-cm source-to-axis

distance (SAD), fully isocentric linac was manufactured in 1961 [24]. Magnetrons and klystrons are capable of establishing intense electromagnetic fields in microwave cavities so that electrons can be accelerated to velocities close to the speed of light. High-energy x-rays are produced, when the high-speed electrons strike a target. Nowadays, linacs have become the most widely used radiation source in modern radiotherapy.

There are several features that make linacs so popular.

- Linacs can provide both electron and photon beams with multiple energies from the same treatment unit, which allow physicians to select beams to treat tumors at various depths.
- High dose rates are available so that the treatment times can be shortened.
- X-ray beams produced by linacs have a sharper dose fall-off at the beam edge than cobalt beams.

The x-ray beams used in this study were produced by the Varian Clinac 21 EX medical linear accelerator as shown in Fig 2.4. Therefore, the following sections will be focused on introducing the operation principles and major components of the linac.

2.3.1 Operation Principles

Typically, a linac consists of several major components. They are the power source, modulator, microwave generator, electron gun, accelerator waveguide, bending magnet, target and flattening filter, beam collimating and monitoring components, and gantry. A block diagram of a typical medical linac is illustrated in Fig 2.5 [25].

Figure 2.4: Varian Clinac 21 EX medical linear accelerator installed at the Grand River Regional Cancer Centre, Kitchener, Ontario, Canada

A power source provides DC power to a modulator, which supplies high-voltage DC pulses with flat tops to the cathode of a microwave generator, such as a magnetron or a klystron. The microwave generator then produces pulsed microwaves, which are delivered to an accelerator waveguide. An electron gun produces low-energy electrons and injects them into the accelerator waveguide at one end. The electrons are accelerated along the waveguide to speeds approaching the speed of light and then enter a bending magnet, where they are redirected towards the centre of the beam's gantry axis of rotation. The high-energy electron beams after passing a scattering foil can be used for treating superficial tumors, or can be operated to strike a target for x-ray production. Before the electron or x-ray beams emerge from the exit window of

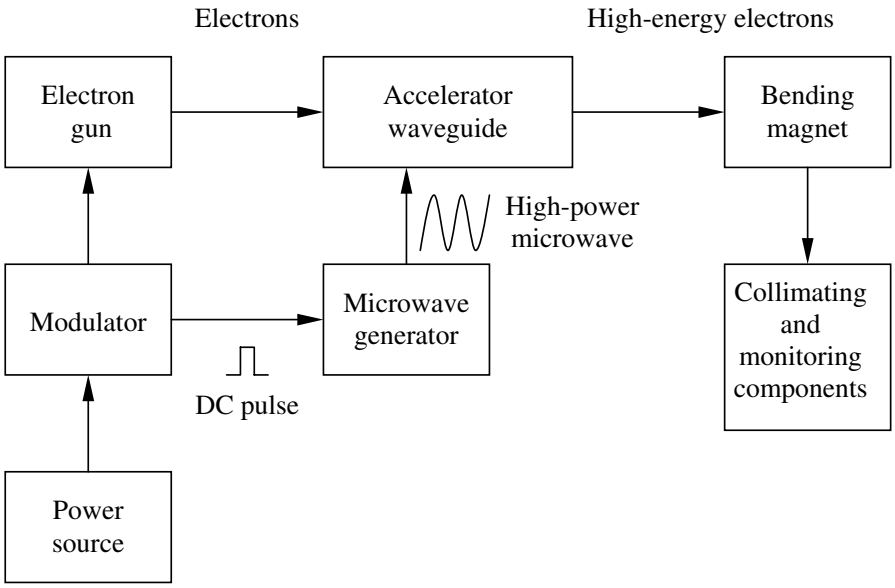

Figure 2.5: Block diagram of a typical medical linac [25]

the linac head, they have to pass collimators and dose monitoring chambers, which to collimate the beam and monitor the dose rate, integrated dose, and field symmetry. More details of each block in Fig 2.5 are provided in the following sections.

Besides the previous components which are directly involved with electron acceleration, other auxiliary systems are also critical to the linac function. The auxiliary supporting systems of the linac include the following [26]:

- A water cooling system to control the temperature of the linac components, such as the accelerator waveguide, target, and microwave generator.
- A vacuum pumping system to provide a vacuum environment for the electron gun, accelerator waveguide, and microwave generator.

- An air pressure system for the pneumatic drives. For example, the movement of the target and other beam shaping components.
- A gas system to improve the dielectric strength of the transmission waveguide.

2.3.2 Magnetron and Klystron

The magnetron is a device that produces microwaves. As shown in Fig 2.6 [23], the magnetron usually has a cylindrical shape with a cathode in the centre and an outer anode. The anode is a whole piece of metal with several resonant cavities machined onto it. A static magnetic field, $\boldsymbol{H}$, is applied perpendicularly to the plane of the cross-section of the cavities. The electrons emitted from the cathode are accelerated towards the anode by a pulsed electric field, $\boldsymbol{E}$, which is applied between the cathode and the anode. Due to the existence of the magnetic field, the electrons move in complex spiral manners. The energy loss of the electrons is radiated in the form of microwaves.

The klystron is a microwave amplifier. It is driven by a low-power microwave oscillator and amplifies the low-power microwaves to high-power microwaves. Fig 2.7 is a schematic diagram of a two-cavity klystron [23].

Low-power microwaves produced by an oscillator set up an alternating electric field between the walls of the first cavity, called the buncher cavity. The electrons generated by the cathode enter the buncher cavity and their velocities are altered to various degrees due to the alternation of the electric field. Some electrons are sped up, while some are slowed down. This process causes bunches of electrons to form.

The electron bunches travel along the drift tube and arrive at the catcher

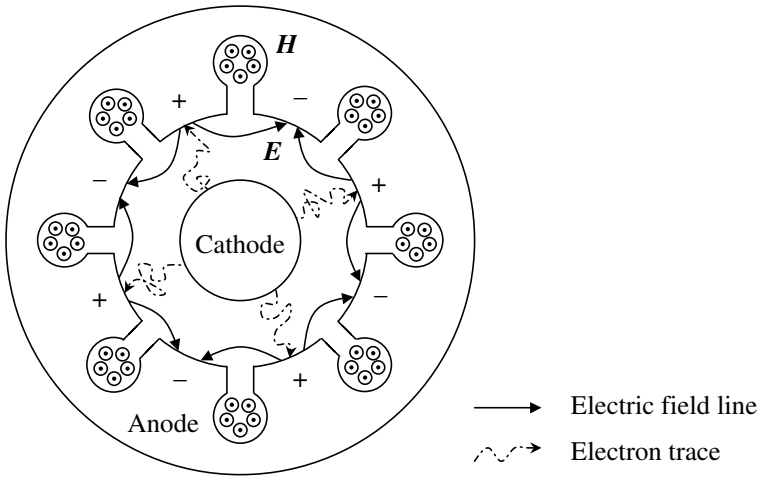

Figure 2.6: Cross-section of a magnetron used to generate microwaves [23]

cavity, where electrons encounter a retarding electric field and are decelerated. During this process, the kinetic energy of the electrons is transferred to the electric field by the principle of the conservation of energy. The energy is extended in the form of amplified microwaves.

The microwave power conveyed from a magnetron or klystron enters an accelerator waveguide through a transmission waveguide, which is filled with pressed gas to prevent arcing. Two isolators, which are transparent to microwaves but block the reflected radiation moving in the opposite direction, are inserted into the transmission waveguide. Another function of the isolators is to separate the pressed gas from the vacuum maintained in the magnetron/klystron and the vacuum maintained in the accelerator waveguide.

Generally, klystrons are more expensive than magnetrons due to their larger physical size, heavier weight, and longer life span. In addition, klystrons are capable of delivering higher power levels. Therefore, linacs providing radiation

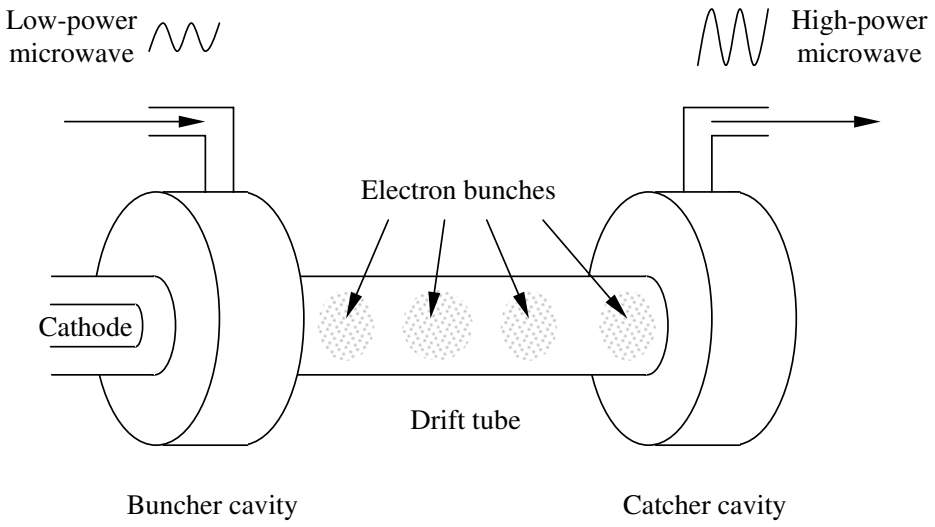

Figure 2.7: Schematic diagram of a two-cavity klystron [23]

beams approaching 20 MeV or higher usually use klystrons to increase the amplification of the microwaves [23].

2.3.3 Electron Gun

An electron gun provides electrons for the accelerator waveguide. Typically, it consists of an indirectly heated cathode, an anode, and a gun grid (see Fig 2.8 [23]). Compared with a conventional directly heated cathode, the indirectly heated cathode can be operated at a lower voltage and offers an enhanced emission of electrons. A grid placed in front of the cathode controls the flow of electrons from the cathode to the anode by altering the voltage in a range of -150 to +180 V. The electrons arrive in the cone-shaped anode and escape through a port into the accelerator waveguide. The electron gun and the microwave source are usually

driven by the same pulses.

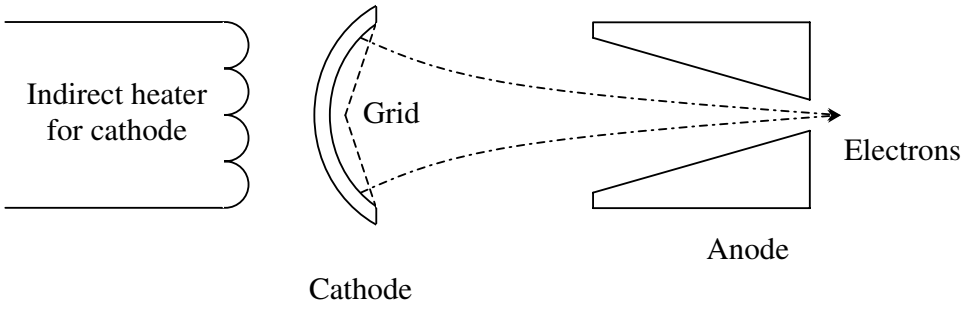

Figure 2.8: Simple form of an electron gun [23]

2.3.4 Accelerator Waveguide

The function of an accelerator waveguide, as suggested by its name, is to accelerate the electrons to very high speeds. It is a hollow pipe with isolated cylindrical electrodes to form individual cavities. The cavities provide a suitable electric field for the acceleration of the electrons. Usually, there is a very high vacuum (typically 10^{-6} torr, 1 torr = 133.3 pascal) maintained inside the waveguide in order to prevent electron loss and arcing.

In the first few cavities of the accelerator waveguide, electrons injected from the electron gun are captured and bunched by the microwaves provided by the klystron or magnetron. In later cavities, the electrons gain energy from the high power microwaves and are accelerated to approach a velocity close to the speed of light.

There are two types of accelerator waveguides: the standing waveguide and the travelling waveguide. Linacs provide beams with energy up to about 6 MV

using low-energy standing waveguides. This kind of waveguide is short (about 0.4 m) and can be mounted vertically in the gantry. For linacs which provide beams with an energy higher than 6 MV, travelling waveguides or high-energy standing waveguides are used. They are longer and must be mounted horizontally within the gantry. A bending magnet is needed in this kind of setup to guide the accelerated electrons toward the patient.

2.3.5 Beam Delivery

When the high-speed electrons emerge from the accelerator waveguide, a bending magnet, a target and flattening filter, and ionization chambers are needed to deliver the radiation beams. The function of each part is briefly described as follows.

Bending Magnet Assembly

A 270 degree bending magnet is used in many modern linacs. A schematic drawing of such a bending magnet is shown in Fig 2.9 [23]. Electrons from the accelerator waveguide have slightly different velocities though their speeds are all close to the speed of light. When the electrons are exposed to the magnetic field, they have different paths due to the effect of the Lorentz force. Energy filters are placed inside the bending magnet assembly to remove the electrons that are not within 5% of the nominal peak accelerated electron energy. Since the radius of the curvatures of the electrons with less or more energy are different, the energy filters can block them from the beam path. Therefore, the electron beam emerging from the bending magnet has a tight distribution of energy and direction.

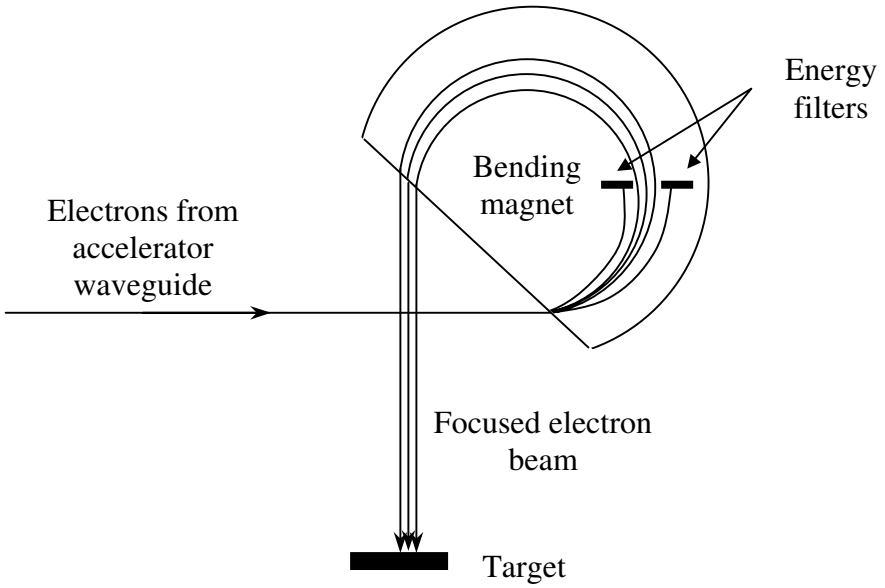

Figure 2.9: Schematic drawing of a 270 degree bending magnet [23]

Target and Flattening Filter

The focused electron beam produces a broad x-ray beam by striking a target, which usually is made of copper. Since the energy of the electrons is in the megavoltage range, the x-ray intensity is peaked in the forward direction. A flattening filter is inserted in the path of the beam in order to make the beam intensity uniform across the field. The flattening filter has a cone-shape with the point of the cone facing the target and is made of tungsten, lead, steel, or combinations of them.

If an electron beam is used in treatments, the target will be removed and an electron scattering foil will be placed in the beam depth instead of the flattening filter. Usually, the scattering foils are mounted on a circular tray at the same level

as the flattening filter.

Internal Monitoring Ionization Chamber

Ionization chambers are used to monitor the dose rate and total dose. The chambers usually are sealed so that their responses are independent of the ambient pressure and temperature variation. For patient safety, most linacs have two separately sealed ionization chambers with completely independent biasing power supplies and readout circuits. If the primary chamber fails during a treatment, the backup chamber will terminate the irradiation at a small margin beyond the prescribed dose. If both ionization chambers fail, the linac timer will shut down the machine at a preset time. Of course the operator can stop beam delivery at any time by using the beam OFF button on the control console in the control room or emergency buttons located in multiple locations inside and outside the treatment room.

In addition to monitor dose information, the ionization chambers also monitor beam flatness and symmetry. The outputs of the ionization chambers are sent to the beam steering coils of the bending magnet through automatic feedback circuits so that the beam flatness and symmetry can be controlled. More details about the operation mechanism of the ionization chambers are introduced in section 2.4.1.

2.3.6 Collimator

Primary Collimator

The primary collimator is located immediately behind the x-ray target and above the flattening filter. It is generally made from tungsten and shaped like a slightly diverging cone that is open at both ends. The function of this collimator is to

prevent the scattered photons leaking from the linac head.

Secondary Collimators (Jaws)

After passing through the ionization chambers, the beam is further collimated by secondary collimators. The secondary collimators, also called jaws, consist of two pairs of metal blocks made from tungsten or lead with about an 8 cm thickness and are able to block 99.6% of the dose [23]. The jaws can rotate around the central beam axis and produce a rectangular opening from 0×0 to the maximum of 40×40 cm^2 field size for each jaw incident at 100 cm from the x-ray source.

If the linac is operated in electron beam mode, the secondary collimators are opened wider than the required field, and an additional electron applicator is attached in the front of the linac head. The applicator is mounted on an accessory mount and provides collimation close to the skin surface of the patient. This is required because the electron scattering in the air produces a wide beam penumbra if the collimators are far away. In the patient treatment, a cutout, a piece of low melting point metal having a window with the shape of the tumor contour, is usually used to shape the electron beam.

For modern linacs, each of the four collimators is driven independently so that they can define asymmetric fields. For example, in Fig 2.10 (a), collimators y_1 and y_2 are located symmetrically at 5 cm from the central axis, whereas, collimator x_1 and x_2 are driven to 2.5 and 7.5 cm from the central axis such that the centre of the 10×10 cm^2 field is off the central axis of the collimators. This setup makes the field have different diverging edges, as shown in Fig 2.10 (b). The use of asymmetric collimators produces changes in the collimator scatter, phantom scatter, and off-axis beam quality [27, 28].

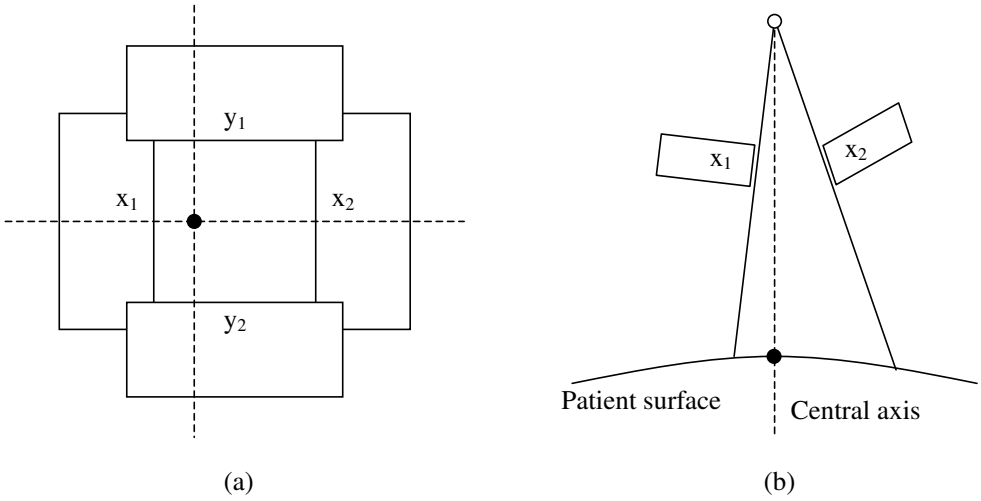

Figure 2.10: Asymmetric field created by secondary collimators (a) beam's eye view and (b) side view

Tertiary Collimation (Multileaf Collimators)

Most modern linacs are equipped with multileaf collimators (MLCs) in addition to basic rectangular jaws. The specifications of MLC differ from one manufacturer to the next. An MLC consists of a large number of collimating leaves (e.g., a Varian type MLC has 60 pairs of leaves with a leaf width of 1 cm at the isocentre plane). Each leaf is driven by an individually computer-controlled motor and control circuit. Commonly, the leaves are made of a high atomic numbered material such as tungsten alloy. Miniaturized MLCs (microMLCs), for example, one with a 3 mm leaf size and 7×7 cm^2 field size at the isocentre plane, are commercially available [29]. The application of MLCs with computer control can easily spare critical organs, such as the heart and the spinal cord, near a target volume. MLCs are particularly useful for conformal

radiotherapy and IMRT.

2.3.7 Gantry

The source of radiation can be rotated about a horizontal axis for most of the linacs. The motion of the gantry is controlled by a control pendant inside the treatment room or the keyboard console in the control room. As the gantry rotates, the central axis of the beam forms a vertically circular plane. The centre of the plane is the isocentre. This isocentric construction enables radiation beams to be directed from various directions but intersect at the isocentre located inside the patient.

As sophisticated megavoltage equipment, linacs produce both x-ray and electron beams at different energy levels and are able to provide adequate dosages of radiation to deep-seated tumors. With careful treatment planning and proper selection of accessories, such as the applicators and cutouts, linacs can provide maximum dose to the target tissues and minimize the exposure of healthy tissues.

2.4 Techniques for Radiation Measurements

2.4.1 Ionization Chambers

Ionization chambers detect radiation by measuring the charge released by different mediums that are exposed to radiation. Typically, they are used for absolute dose measurements. The thimble type chamber and the parallel plate chamber are two commonly used ionization chambers. The thimble type chambers have a

cylindrical structure and are irradiated through the cylinder-shape electrode. The parallel plate ionization chambers contain two parallel electrodes, which could be circular or rectangular, and are irradiated with a primary beam through the upper electrode. The sensing principle of a parallel plate ionization chamber can be explained by taking gas as an active volume medium as an example. Fig 2.11 illustrates the sensing process [22].

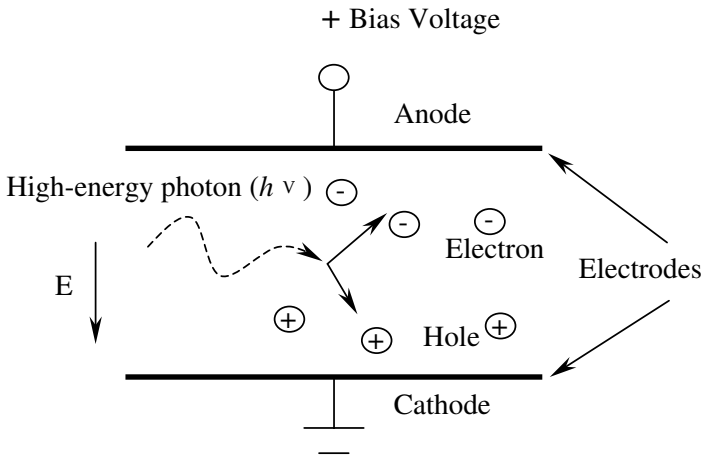

Figure 2.11: Sensing principle of a parallel plate ionization chamber [22]

A bias voltage is applied to maintain a uniform electric field between the two electrodes. The electric field strength is proportional to the applied bias voltage. When ionizing radiation interacts with the gas in the active volume of the detector chamber, the high-energy particles transfer energy to the gas molecules, which split into electron and hole pairs. Under the external electric field, the holes and electrons move to the cathode and anode, respectively. This, in turn, creates a small current, which is detected by the electrometer. From the detected signal, the radiation dosage is quantified. The absorbed dose in the gas of the active

volume is defined as the charge produced per unit mass multiplied by the energy required to produce a unit charge, which is calculated by

$$D_{gas} = \frac{Q}{m_{gas}} W, \tag{2.7}$$

where D_{gas} is the absorbed dose in the gas (Gy), Q represents the charges collected in the active volume of the chamber (C), m_{gas} is the mass of the gas in the active volume (kg), and W is the average energy required to cause one ionization pair in the gas (J/C or eV/ion pair). W is a constant over widely varying conditions of air pressure and electron energies and is equal to 33.97 J/C for air. Equation 2.8 is an extended version of equation 2.7 after taking into account the effects of the temperature and pressure according to the gas density.

$$D_{gas} = \frac{Q}{\rho \cdot V} W (\frac{273.2 + T}{273.2})(\frac{101.3}{P}), \tag{2.8}$$

where ρ is the density of the gas in the chamber at standard temperature and pressure (0 ^{o}C, 101.3 kPa) (kg/m^3), V is the chamber active volume (m^3), T is the temperature of the gas in the chamber (^{o}C), and P is the pressure of the gas in the chamber (kPa).

2.4.2 Thermoluminescence Dosimeters

TLDs are based on the radio-thermoluminescence property of materials. TLDs are available in a wide range of materials, sizes, shapes, and as powder or solid. Because LiF:Mg, Ti (lithium fluoride doped with magnesium and titanium) TLDs are most commonly used in radiotherapy, the general principle is illustrated in the

following paragraph by considering this type of dosimeter as an example.

In general, TLDs consist of crystals that are nonconducting. At room temperature, all the electrons are confined to the valence band, and no electrons exist in the conduction band. Some of the electrons may gain enough energy to jump into the conduction band if the crystal is irradiated with ionizing radiation. There are a number of impurities in the crystal. The impurities can trap electrons from the conduction band at an energy state that is between the conduction band and the valence band. Usually, the energy gap between the conduction band and the traps is of the order of a few eV, and the number of electrons trapped is directly proportional to dose. The depth of the traps and the temperature determine the probability that the electrons can gain enough energy to return to the conduction band. With an increase in temperature, there is a high possibility that the electrons will return to the conduction band and release energy in the form of light. The light emission requires a second type of crystal impurity. In LiF:Mg, Ti magnesium is associated with the electron trapping (impurity level 1), whereas titanium plays a role in the light emission (impurity level 2). The general principle of TLDs is found in Fig 2.12 [1].

When TLDs are employed for dosimetric measurements, great care must be taken because scratches or contamination of the detector surface reduces the light emitted from the detector. Therefore, all thermoluminescence materials should be handled with vacuum tweezers and separated in an array. In addition, strict annealing procedures must be followed. The annealing procedures consist of three steps: (i) high temperature annealing prior to irradiation, (ii) low temperature annealing prior to irradiation, and (iii) prereadout annealing at a low temperature after irradiation. Generally, TLDs are placed into a high temperature furnace preheated to 400 ^{o}C for 1 hour. At the end of the annealing, the TLDs are

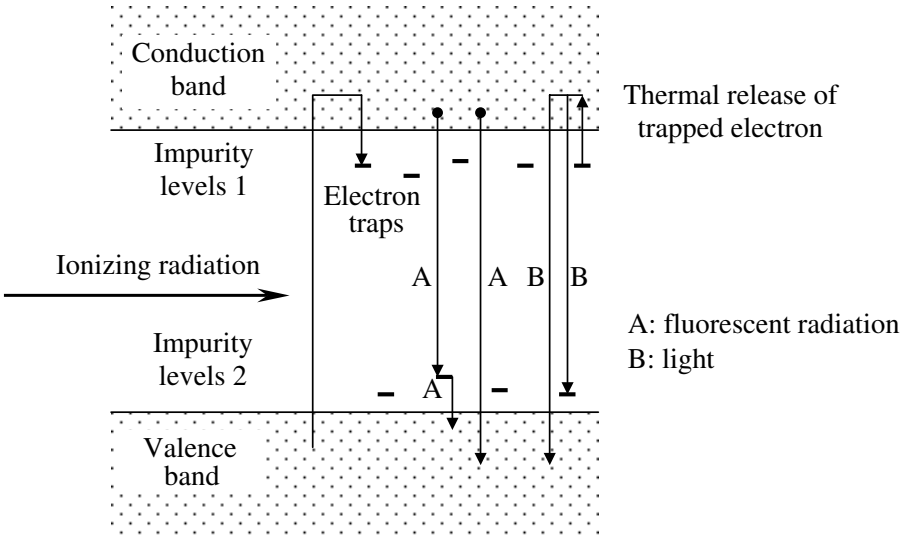

Figure 2.12: General principle of TLDs [1]

immediately removed from the high temperature furnace and transferred into a low temperature furnace preheated to 105 ^{o}C, where they remain for 2 hours. Then the TLDs are removed from the furnace and cooled to room temperature. After being irradiated and before being read out, the TLDs are annealed for 15 minutes inside the low temperature furnace that is preheated to 105 ^{o}C. Then, the TLDs are ready to be read out [6]. An example of a glow curve of a TLD is shown in Fig 2.13.

2.4.3 Film Dosimeters

One of the most important features of film dosimeters, compared with those of other dosimeters, is that a 2D spatial distribution map of the radiation is obtained. Radiographic and radiochromic film are two types of film dosimeters primarily used in radiotherapy. The operation of both film dosimeters is based

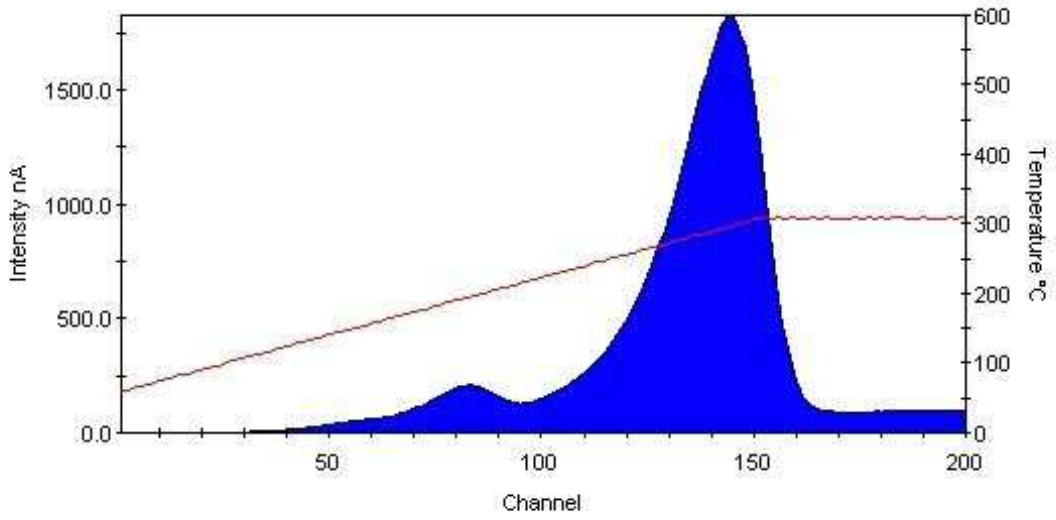

Figure 2.13: Example of a glow curve of a TLD

on the colour change of the radiosensitive emulsions. The silver in silver bromide is reduced to metallic silver in a radiographic film due to ionizing radiation. The radiochromic material turns blue, when it is irradiated, due to a solid-state polymerization process in a radiochromic film. The dose of the radiation is related to the darkening of the film, which is referred to as the OD. This relationship is expressed as follows:

$$OD = \log_{10}(\frac{I_0}{I}), \tag{2.9}$$

where I_0 is the light intensity with no film present, and I is the light intensity after transmission through the film. The advantage of this definition is that the ODs are additive. Two layers of film (or two exposures of the same film) produce a sum of the ODs: $OD = OD_1 + OD_2$. Fig 2.14 displays a typical OD curve of a film dosimeter.

In the following two paragraphs, radiographic and radiochromic film are

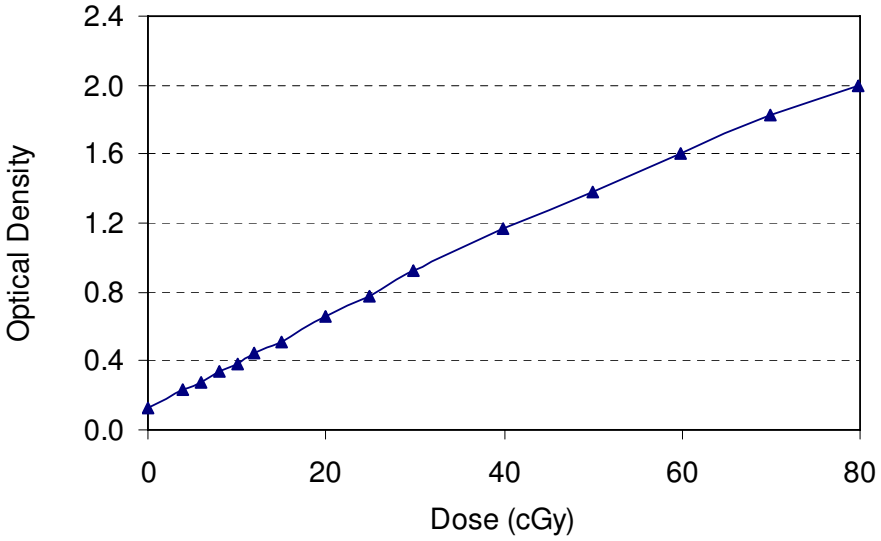

Figure 2.14: OD curve of a film dosimeter

introduced, respectively.

- **Radiographic Film**: Radiographic film consists of a clear polyester base that is coated on one or both sides with a radiosensitive emulsion. Normally, the sensitive layer consists of silver bromide crystals embedded in gelatine. The absorption of ionizing radiation causes the following reaction:

$$\text{Photon} + \text{Br}^- \longrightarrow \text{Br} + \text{e}^-$$

$$\text{e}^- + \text{Ag}^+ \longrightarrow \text{Ag}$$

The elemental silver is black and produces a latent image. During the development of the film, silver ions are reduced in the presence of silver atoms. The silver bromide in undeveloped grains is washed away from the film during fixation, and only the areas of the film that are hit by radiation appear black. The degree of the darkening is related to the dose deposited on the film and is expressed in equation 2.9.

- **Radiochromic Film**: Colourless, transparent radiochromic films become permanently coloured by the absorption of the radiation. This colour change does not require any latent thermal, optical, or chemical development or fixation. When a radiochromic film is exposed to ionizing radiation, colouration occurs due to an attenuation of some of the visible light coming through the developed film.

  Ideally, the relationship between the dose and OD should be linear, however, both radiographic and radiochromic films are relatively linear only over a limited range. Some factors that affect the sensitivity of film dosimeters include photon beam energy, film uniformity, film plane orientation, experimental designs, post-irradiation conditions, and the types of densitometers used.

  Most radiochromic films are sensitive to UV light in varying degrees [21, 30]. For most medical applications, UV light causes an unwanted reaction in the films. Therefore, films must be protected from UV sources such as the sun and fluorescent light exposure, and the films should be stored in an opaque container and taken out only for experiments and readouts.

  If there is a UV component in the readout light sources for densitometry, it can also have an effect on the radiochromic film. Again, care must be taken when fluorescent light sources are used for the readout of radiochromic film products.

  Many radiochromic films are produced with various layers in their construction. These constructions produce effects based on the polarization qualities of the readout light sources used for the OD evaluation. Klassen et al. [31] found that the orientation of the film in

terms of the front and back can produce a variation in the measured OD on the same piece of film.

2.4.4 Semiconducting Dosimeters

Semiconducting dosimeters include silicon diodes and MOSFET dosimeters. The mechanism of semiconducting dosimeters for radiation detection is explained by considering a MOSFET dosimeter as an example. The irradiation of MOSFET dosimeters causes a threshold voltage shift. The shift is proportional to the total quantity of trapped charges, which is proportional to the dose. Ionizing radiation passing through the SiO_2 layer creates electrons and holes. After an initial recombination of the electrons and holes, the non-recombined electrons move quickly to the metal contacts, and the holes have a low effective mobility and are trapped in a narrow region near the SiO_2/Si interface. These trapped charges lead to the threshold voltage shift of the MOSFET dosimeter. The radiation-induced charge trapping process is shown in Fig 2.15 [32]. Fig 2.16 shows a calibration curve of a MOSFET dosimeter.

The efficiency of charge trapping depends on the thickness of the oxide layer, the gate potential applied during irradiation, and the quality of the oxide layer obtained from the fabrication process. One way to increase the sensitivity of MOSFET dosimeters is to increase the thickness of the SiO_2 layer. It is straightforward that a increase in the SiO_2 layer results in more electrons and holes that are generated during radiation. The experimental results indicate that the number of electron-hole pairs generated within the SiO_2 layer obeys a power law dependence on the SiO_2 thickness t_{ox}^n, where t_{ox} is the thickness of the SiO_2 layer and n varies according to the type of oxide grown (wet vs. dry), growth

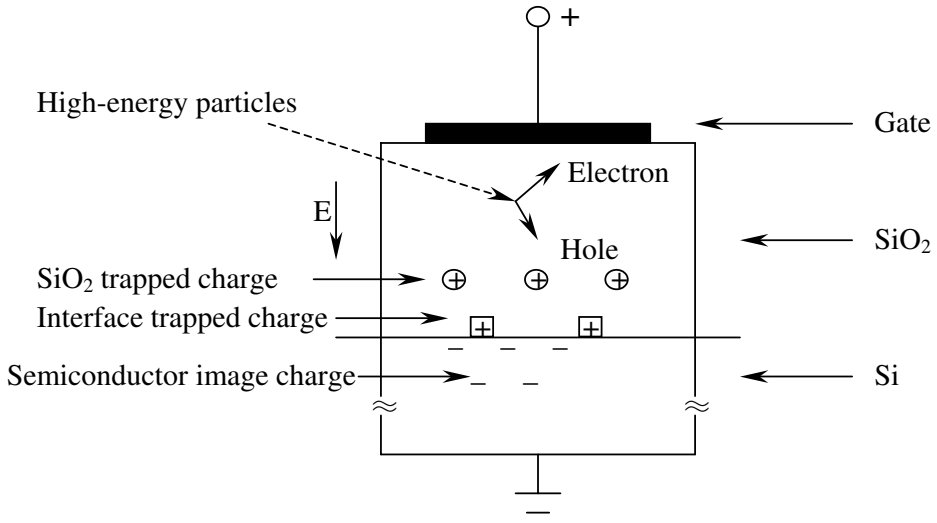

Figure 2.15: Radiation-induced charge trapping process in a MOSFET dosimeter [32]

rate, growth ambient pressure and temperature, and post oxidation anneal ambient pressure and temperature [33]. The typical thickness of the gate oxide layer of a commercial MOSFET is approximately 50 to 80 nm. However, it takes more than 100 hours at temperatures of 1000 ^{o}C to grow an oxide layer thicker than 1 μm. This oxidation time is not feasible. Clearly, these fabrication processes limit the sensitivity of MOSFET dosimeters.

2.5 Conclusion

The fundamentals of radiation physics, including the photon and the electron interactions with matter, are introduced in this chapter. The operation principle and major components of the linac are presented. Four commonly used dosimeters,

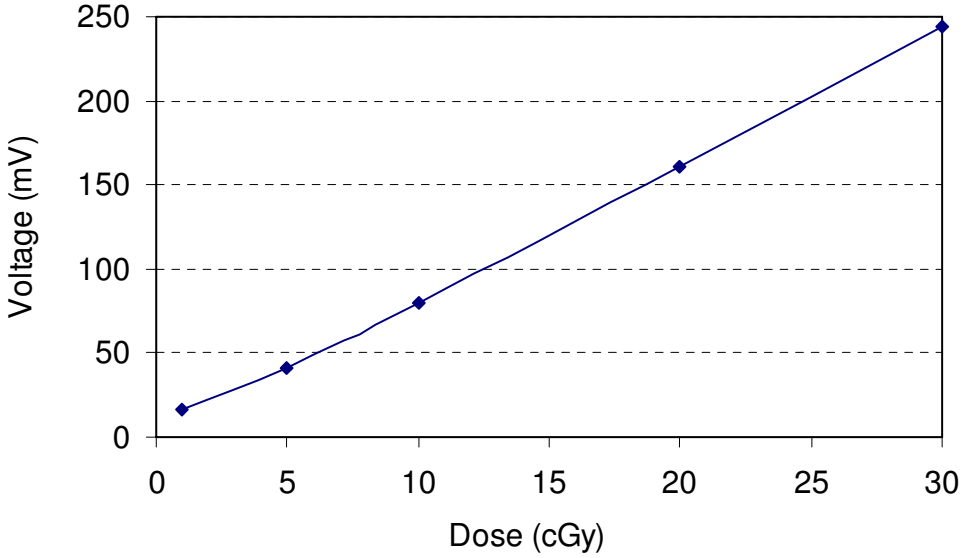

Figure 2.16: Calibration curve of a MOSFET dosimeter

ionization chambers, TLDs, film dosimeters, and semiconducting dosimeters, and their detection mechanisms are summarized. The next chapter describes carbon nanotubes, the sensing material of the proposed dosimeters.

Chapter 3

Carbon Nanotubes

3.1 Introduction

Since the discovery of CNTs in 1991 [34], CNTs have been widely studied for their potential as important new materials for micro- and nanotechnology. CNTs are hollow tubes that are composed of carbon atoms. The typical diameter of a CNT is tens of nanometers, and its length can vary from nanometers to hundreds of microns [35]. One of the most attractive properties of CNTs is their applications on biomedical research because of their superior structural, mechanical, and electrical properties such as small size and mass, high strength, and higher electrical and thermal conductivities [34, 36].

CNTs can be thought of as a layer of graphite rolled up into a cylinder [37]. Depending on the arrangement of their graphene cylinders, there are two types of nanotubes: (i) single-walled nanotubes (SWNTs) and (ii) multi-walled nanotubes (MWNTs). SWNTs have only one single layer of graphene cylinders, whereas MWNTs have many layers with spacing between the consecutive layers of 3.4 angstrom [38]. Furthermore, the films of synthesized CNTs can be random or

aligned in nature as shown in Fig 3.1.

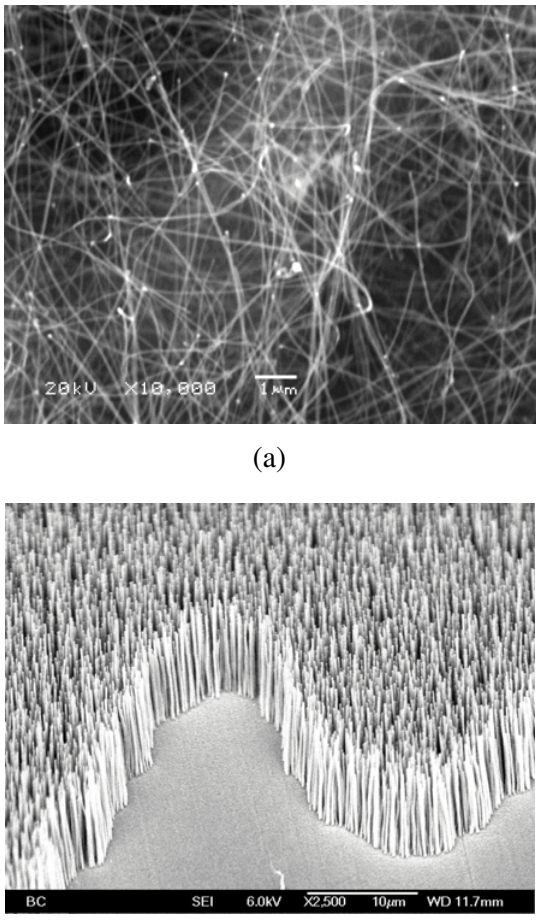

(a)

(b)

Figure 3.1: Orientation of the CNTs can be (a) random or (b) aligned

The following description of carbon nanotubes include: (i) a brief introduction of three synthesis methods of CNTs, (ii) a description of the purification techniques of CNTs, (iii) a summary of the electrical, mechanical, and thermal properties of CNTs, (iv) a highlight of the applications of CNTs with potential in radiation dosimetry, and (v) a proposal of three methods for

using CNTs in radiation dosimetry.

3.2 Synthesis

Generally, three techniques are used for CNTs synthesis: (i) the carbon arc-discharge technique, (ii) the laser-ablation technique, and (iii) the chemical vapour deposition (CVD) technique.

3.2.1 Carbon Arc-Discharge Technique

In 1991, Iijima discovered MWNTs by using an arc-discharge technique [34]. In 1993, SWNTs were synthesized for the first time by Iijima and Ichihashi [39] and Bethune et al. [40] using metal catalyst in the arc-discharge method. In the carbon arc-discharge technique, two carbon electrodes are used to generate an arc by DC current. The electrodes are placed in a vacuum chamber. An inert gas is supplied to the chamber in order to increase the speed of the carbon deposition. Initially, the two electrodes are kept far apart. Once the pressure is stabilized, a 20 V voltage is applied, and the anode is then gradually brought closer to the cathode to strike the electric arc. The electrodes become red hot and a plasma forms during the arcing. Once the arc stabilizes, the electrodes are kept about a millimetre apart while the CNTs are deposited on the cathode. When a specific length of the CNT is reached, the power supply is cut off and the machine is left for cooling.

3.2.2 Laser-Ablation Technique

The laser-ablation technique was used by Thess et al. [41] to produce bundles of aligned SWNTs. In this technique for manufacturing CNTs, intense laser pulses are utilized to ablate a carbon target. The pulsed laser-ablation of graphite in the presence of an inert gas and catalyst forms CNTs [41]. Arepalli et al. [42] found that individual nanotubes with lengths of tens of microns are formed in the vicinity of the target at the beginning. These nanotubes subsequently coalesce into bundles. In general, there are several major parameters that determine the amount of CNT produced by this method: the amount and type of catalysts, laser power and wavelength, temperature, pressure, type of inert gas present, and the fluid dynamics near the carbon target [43, 44].

3.2.3 Chemical Vapour Deposition Technique

For the first time, the catalytic growth of MWNTs by CVD was proposed by Yacaman et al. [45]. In the CVD technique, CNTs are synthesized by imparting energy to hydrocarbons. The imparted energy breaks the molecule into reactive radical species in the temperature range of 550 to 750 ^{o}C. Then, these reactive species diffuse down to the substrate, which is heated and coated with catalysts (usually a first row transition metal such as Ni, Fe, or Co), where it remains bonded. This process results in the formation of CNTs. The commonly used hydrocarbon sources are methane, ethylene, and acetylene, and the commonly used energy sources are electron beams. Varadan and Xie [46] developed a CVD technique using microwave energy for synthesizing MWNTs. The authors used acetylene as the hydrocarbon and cobalt as the catalyst at a temperature of 700 ^{o}C. MWNTs prepared by this process have an average diameter of 20 to 30 nm

and consist of 26 layers. Park et al. [47] used a sequential combination of radio frequency plasma enhanced CVD (RF PECVD) and thermal CVD to synthesize CNTs on stainless steel plates from an acetylene and hydrogen gas mixture. Seidel et al. [48] synthesized dense networks of SWNTs by using a Ni catalyst layer of 0.2 nm thickness by thermal CVD at temperature as low as 600 ^{o}C.

3.3 Purification

In all the aforementioned CNT preparation methods, a number of impurities are produced. In the case of the arc-discharge and laser-ablation techniques, the by-products are fullerenes, graphitic polyhedrons with enclosed metal particles, and amorphous carbon [49]. The most common impurities are carbonaceous materials, whereas the other types of impurities that are generally observed are metals [50]. The impurities limit the utilization of CNTs in certain applications. Therefore, CNTs need to go through purification processes before being used.

In the carbon arc-discharge technique, the impurities can be purified by oxidation as the carbonaceous impurities have high oxidation rates. Gas phase purification [51, 52] and liquid phase purification [53, 54, 55] are two approaches for purification by oxidation. Purified SWNTs of lengths less than 2 μm were observed by scanning electron microscopy (SEM) when nitric acid, sulphuric acid, and their mixture were used as oxidants [55]. Transmission electron microscopy (TEM) confirmed that the SWNTs were purified with little damage on the surface and metal catalysts were efficiently removed.

A purification technique for SWNTs that are synthesized by the pulsed laser-ablation technique uses a cationic surfactant and trapped SWNTs on a membrane filter [56]. 90% purity by weight after purification was observed by using this

method. However, the technique was microscale in nature and was not very useful for purifying large batches. A macroscale technique was developed to overcome this limitation [57]. The purification process can be scaled to industrial levels of throughput, when such volumes of SWNT material become available.

A purification process consisting of sonication, oxidation, and acid washing steps has been developed to purify the SWNTs grown by the CVD technique [58]. MWNTs grown by the CVD method were subjected to wet and dry oxidation to remove the impurities and traces of catalysts [59]. It was observed that the $KMnO_4/H_2SO_4$ aqueous oxidation procedure was effective in reducing the Co catalyst while moderately damaging the outer wall of CNTs.

Some other techniques have also been used to purify CNTs. CNTs were boiled in nitric acid aqueous solutions to remove the amorphous carbon and methal particles [60]. SWNTs with more than 90% purity were generated by Shelimov et al. [61] by using ultrasonically assisted microfiltration from amorphous and crystalline carbon impurities and metal particles. A scalable purification method for SWNTs was developed using microwave heating in air followed by a treatment with hydrochloric acid [62]. Microwave-assisted purification has been used by Ko et al. [63] for the purification of MWNTs.

3.4 Properties

The chirality and diameter of CNTs determine their properties. In electrical terms, chirality and diameter determine whether the CNT will behave as a metal or a semiconductor [64, 65]. As is shown in Fig 3.2, the chiral vector of CNTs, $\boldsymbol{C}$, is represented mathematically by two unit vectors a_1 and a_2.

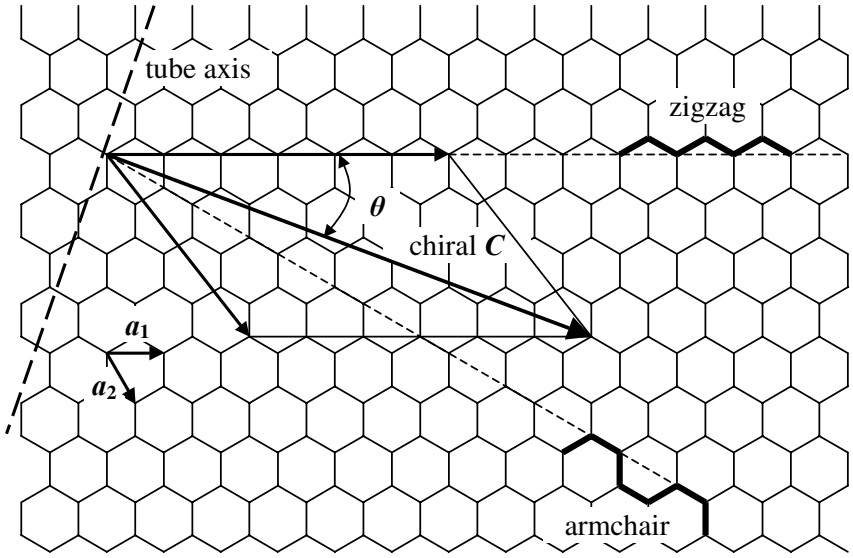

Figure 3.2: Chiral vector for the CNT characterization [66]

$$\boldsymbol{C} = n\mathbf{a_1} + \mathbf{ma_2}, \tag{3.1}$$

n and m are positive integers. The diameter of a CNT, d, and the chiral angle, θ, can be obtained by using equation 3.2 and equation 3.3 [67].

$$d = \frac{a\sqrt{m^2 + mn + n^2}}{\pi} \tag{3.2}$$

$$\theta = \arctan(\frac{\sqrt{3}m}{2n + m}) \tag{3.3}$$

where a is the distance between the consecutive carbon atoms (1.42 angstrom).

The relation between n and m defines three categories of CNTs: (i) armchair ($n = m$ and chiral angle equal to 30^o); (ii) zigzag ($n = 0$ or $m = 0$ and chiral angle

= 0^o); and (iii) chiral (other values of n and m and chiral angles between 0^o and 30^o) [68]. All armchair nanotubes are metals, as well as those with $n - m = 3j$ (j being a nonzero integer). All others are semiconductors, which have a band gap that is inversely related to the diameters of the nanotubes [69]. For the development of molecular electronics, methods have been proposed by Collins et al. [70], Krupke et al. [71], and Banerjee et al. [72] to separate the metallic and semiconducting SWNTs.

3.4.1 Electrical Properties

The dielectric behavior of the CNTs are found to be highly anisotropic. Owing to their nearly one-dimensional electronic structure, electronic transport in metallic SWNTs and MWNTs occurs ballistically (without scattering) over long distances. This enables nanotubes to carry high currents with negligible heating [73, 74]. MWNTs can carry high current densities up to 10^9 - 10^{10} A/cm^2 and can conduct current without any measurable change in their resistance or morphology for extended periods of time at temperature up to 250 ^{o}C [75]. Superconductivity in SWNTs has been observed at low temperatures [76]. The doping of CNTs provides various ways for controlling their physical properties. Doped CNTs have applications in nanoelectronics, field emission, nonlinear optics, and chemical sensors [77]. CNTs can align themselves along field lines under a high electric field. This observation may lead to novel electromechanical applications for CNTs [78].

3.4.2 Mechanical Properties

CNTs are currently the strongest known fibres because the carbon-carbon bond observed in graphite is one of the strongest in nature. Typically, the Young's modulus of a defect-free SWNT is about 1000 GPa. The Young's modulus for a MWNT is higher than that for a SWNT because when different diameters of SWNTs consist in a coaxial MWNT, the Young's modulus will take the highest value of a SWNT plus the contributions from the coaxial intertube coupling or van der Waals force. Thus, the Young's modulus for a MWNT is about 1100 to 1300 GPa. Wong et al. [79] using atomic force microscopy (AFM) determined the average value of Young's modulus of MWNTs is around 1280 GPa. The tensile strength of SWNT bundles is in the range of 13 to 52 GPa. In the case of MWNTs, it is observed that only the outermost layer breaks during the tensile load testing process, and the value is in the range of 11 to 63 GPa [80, 81].

3.4.3 Thermal Properties

The specific heat and thermal conductivity of CNTs are dominated by phonons as the electronic contribution is negligible due to low density of free charge carriers [82]. CNTs have thermal properties that are similar to those of graphite and diamond at room and elevated temperatures, but unusual behaviour at low temperatures. The intertube coupling in SWNT bundles and MWNTs is weak in the temperature region > 100 K [83]. The experiments by Yi et al. [84] revealed a linear dependence of the specific heat of MWNTs on the temperature over the entire temperature interval (10 to 300 K). MWNTs and bundles of SWNTs with an average diameter of 1.3 nm were used by Mizel et al. [85] to measure the specific heat in the temperature range $1<T<200$ K. Theoretical calculations

showed that the thermal conductivity for SWNT ropes and MWNTs at room temperature could vary between 1800 and 6000 W/mK whereas more than 3000 W/mK is obtained from the experimental measurement of a single MWNT [86]. It was observed by Zhang et al. [87] that the value of the heat conductivity of a zigzag nanotube is maximum, while the chiral nanotube has a minimum value. The authors also found that the thermal conductivity of SWNTs depends on their length, radius, temperature, and chirality. Therefore, nanoscale devices with different heat conductivities can be made with nanotubes of different chiralities.

3.5 Potential Applications of CNTs for Radiation Detection

In the last few years, intensive studies have been conducted to explore different applications of CNTs. These applications include energy storage and energy conversion devices [88], high strength composites [89], nanoprobes and sensors [90, 91], actuators [92], electronic devices [93], catalysis [94], and hydrogen storage media [95]. This section highlights existing applications of CNTs with potential for radiation dosimetry. A comprehensive review on the applications of CNTs can be found in the literature [96].

Enhancement of Electric Fields by CNTs

Modi et al. [97] fabricated a miniaturized gas ionization sensor by using vertically aligned MWNT film as the anode. The sharp tips of the CNTs generated a very high electric field at relatively low voltages and as a result, the breakdown voltage

was reduced significantly. For example, the breakdown voltage of the air dropped from 960 V with a current discharge of 69 μA, measured by a traditional gas sensor, to 346 V with a current discharge of 460 μA, measured by the CNT-based gas sensor. The sensor is not sensitive to temperature, humidity, and gas flow.

Particle-Collision-Induced Resistance Change of CNTs

CNTs can be regarded as a graphite sheet rolling up to form a nanotube cylinder with all the carbon atoms residing at the tube surface. Because of this special structure, the environments in contact with the CNTs affect the electron transport along the nanotube. Romero et al. [98] reported that significant changes in the electron transport in metallic SWNTs were observed when the SWNTs were undergoing collision with inert gas atoms or other small molecules. Their experimental results revealed that the radial direction deformation of the SWNTs due to the particle collisions induced resistance changes of the SWNTs. Moreover, the results showed a relationship between the gas pressure and resistance changes, where the pressure was a measure of the collision frequency of the particles with the nanotube walls.

Carbon Nanotube Field Effect Transistor Dosimetry

Tang et al. [99] fabricated carbon nanotube field effect transistor (CNTFET) dosimeters, which were analogous to MOSFET dosimeters in terms of device configuration and substrate fabrication processes. The irradiation of a CNTFET device causes a shift in its threshold voltage, which is proportional to the radiation dose deposited in the oxide insulation layer that is residing between the back gate and the SWNT channel. The performance of the CNTFET dosimeters is comparable or even superior to commercial MOSFET dosimeters.

This is the first time for demonstrating that CNT-based dosimeters are capable of detecting ionizing radiation. The device did not display any sign of radiation damage on the nanotubes after being exposed to radiation.

Transparent CNT Network FET

CNTs are shown to behave as semiconductors, allowing the use of CNTs in transistors. In a single CNT transistor, a single nanotube serves as a channel allowing the carriers to move from the source to the drain. It has been shown that a random network of nanotubes with an appropriate density can also act as a conducting channel in a FET configuration. Artukovic et al. [100] built a transparent and flexible transistor with CNT network films. The substrate of the transistor was a sheet of polyester (PE). To form the gate layer of the FET, a suspension of SWNTs was sprayed onto the PE substrate forming a dense nanotube network. Thin strips of gold were evaporated at the opposite edges of the substrate on top of the CNT network as electrical contacts. The insulating layer in this transistor was a 1.5 μm thick layer of Parylene N. Another CNT network film with a lower density was formed on top of the insulating layer as a source-to-drain channel. The gate, insulating layer, and conducting channel exhibit a combined 80% transparency in the visible range. Repetitive bending had only minor influence on the characteristics of the transistor. The source-to-drain current was reduced slightly when the device was bent, but the device recovered completely afterwards.

3.6 Discussion

The applications of CNTs highlighted above indicate the potential of CNTs for radiation dosimetry.

The same idea behind the CNT gas ionization sensor [97] can be transferred to conventional ionization chambers to improve their ionization collection efficiency. When aligned CNT films are grown on top of the two electrodes of an ionization chamber, the electric field between the two electrodes can be reinforced due to the sharp tips of the CNTs. Therefore, the operation voltage of the ionization chamber can be lowered, but an acceptable ionization collection efficiency can still be achieved. The lower voltage potentially offers a safer and more convenient environment for radiation detection.

As it was reported that particle collisions with CNTs induced a resistance change in [98], it can also occur when the CNTs are irradiated with ionizing radiation. X-ray beams and electron beams consist of photons and electrons, respectively. Both are small particles. The dose rate of the beams controls the intensity of photons and electrons, which in turn, determines the collision frequency of the photons and electrons with the CNTs. Therefore, it is feasible to try and establish a relationship between the radiation dose rate and the corresponding resistance changes of CNTs.

The CNTFET detector built by Tang et al. [99] demonstrates the usage of CNTs for radiation measurement. However, the dosimeter has a similar design and sensing principle as MOSFET dosimeters. The physical limitations in silicon fabrication processes remain a problem. For example, the thickness of a silicon dioxide layer still limits the sensitivity of the CNTFET detectors. In addition, the lack of control over a single CNT diameter and chirality during synthesis is also a

big challenge. The simple CNT network FET reported in [100] demonstrates an entirely new transistor structure, which can be used in the design of CNT-based film dosimeters. The most attractive feature of such dosimeters is transparency and flexibility, which make wearable dosimeters possible.

3.7 Conclusion

Research activity related to CNTs has grown phenomenally in the last one and half decades. The synthesis, purification, and properties of CNTs are introduced in a short form prospectus. The potential applications of CNTs related to radiation detection are highlighted in this chapter. It is expected that many applications of CNTs will be explored in future as the interest of the nanotechnology research community in this field increases.

Chapter 4

Parallel Plate Ionization Chamber with CNT Electrodes

4.1 Introduction

This chapter describes a CNT-based parallel plate ionization chamber. The chamber has two stainless steel electrodes, which are customized to accommodate the CNT samples. The substrate materials for growth CNTs and the size of the CNT layers are restricted by the product offered by the company. The reason to choose stainless steel plates as electrodes is because they meet the requirements for CNT layer growth and as conductive electrodes in the proposed chamber. Experiments, including signal saturation characteristics, linearity, and electrode separation, were carried out to characterize the chamber. The experimental results confirmed that the prototype chamber is suitable for studying the ionization collection efficiency of CNTs. In the second stage, square- and irregular-shaped CNT electrodes were designed. The saturation characteristics of the chamber with the CNT electrodes were measured. The

experimental results are provided and discussed.

4.2 Dosimeter Design and Fabrication

The structure of the CNT-based parallel plate ionization chamber is shown in Fig 4.1. The chamber consists of three main parts: (i) two parallel metal electrodes, (ii) an electrode separation vernier, and (iii) a polymethyl methacrylate (PMMA) container. Each is indicated in Fig 4.1 by 1, 3, and 6, respectively.

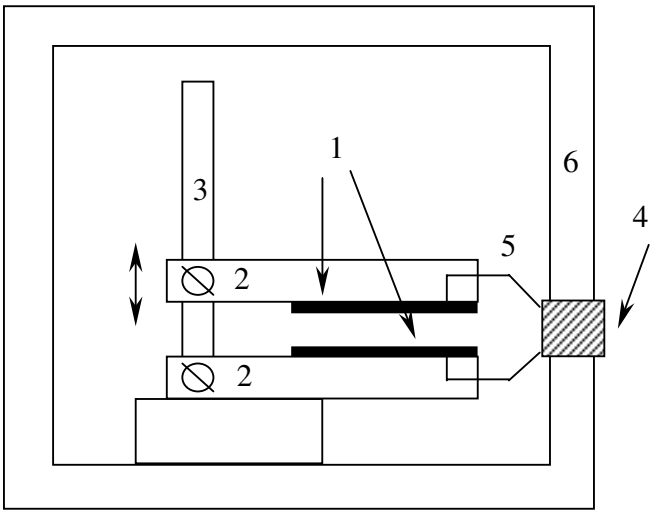

Figure 4.1: Proposed parallel plate ionization chamber: 1. metal electrodes, 2. PMMA electrode holders, 3. electrode separation vernier, 4. output port, 5. low-noise cable, and 6. PMMA container

Two parallel electrodes of stainless steel plates with a 1.5 mm thickness and a 40 $\times$ 40 mm^2 dimension were constructed. This design differs from other conventional parallel plate ionization chambers for surface dose measurements [101, 102, 103]. In a conventional parallel plate ionization chamber, the upper

electrode usually contains thin plastic coated with conductive materials, such as aluminum or graphite coated Mylar®. There are three reasons for choosing the parallel plate structure and relatively thick metal plates as electrodes in the proposed design. First, the parallel plate structure allows the insertion of the CNTs inside the active volume of the chamber to study the ionization collection efficiency, and it allows for easy and precise control of the electrode separation distance. Secondly, the shape and thickness of the electrodes were made compatible with the CNT samples and easy to make electrical connection. Thirdly, the relatively thick upper metal electrode produces more secondary electrons, which enhance the signal to noise ratio. This is essential in this investigation especially since a small electrode separation distance and low bias voltage are used for the measurements.

The two metal electrodes were held by 1 cm thick PMMA levers. The upper electrode was controlled by an electrode separation vernier with a resolution of 0.1 mm, and could be moved closer or farther away from the bottom electrode, thus changing the plate separation and the corresponding active volume. Low noise cables were used to connect the electrodes to the output port, which was fixed on the container wall. The entire setup was mounted within a PMMA container. A photo of the proposed parallel plate ionization chamber is shown in Fig 4.2.

4.3 Experimental Environment

After the design and fabrication of the chamber, extensive measurements were carried out at the Grand River Regional Cancer Centre, Kitchener, Ontario, Canada. 6 MV and 15 MV photon beams produced by the Varian Clinac 21 EX medical linear accelerator were used for ionization measurements. The chamber

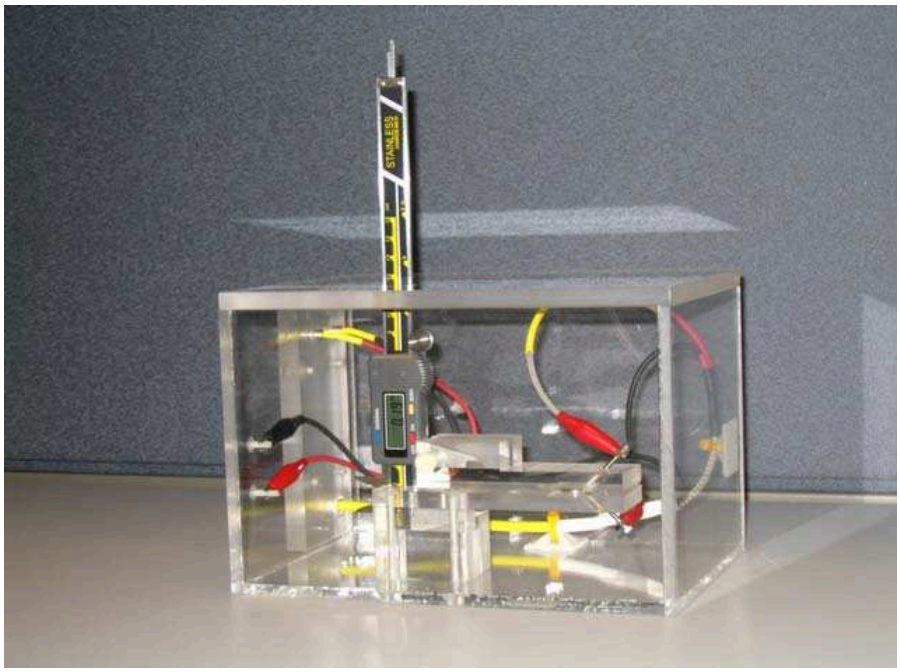

Figure 4.2: Photo shows the structure of the proposed parallel plate ionization chamber

was placed under the linac head with a source-to-surface distance (SSD) of 100 cm. The linear accelerator was calibrated such that 1 monitor unit (MU) produces 1 cGy in water for a calibration geometry of 100 cm from the source to the point of measurement, 10×10 cm^2 field size at the point of measurement, a depth of 5 cm in water. This calibration corresponds to the doses in the air of 1.272 cGy and 1.267 cGy, respectively, for 6 MV and 15 MV photon beams. Signals were measured by a Dose 1 therapy digital electrometer (Scanditronix-Wellhofer®), which can provide current and charge readings. A low noise cable was used to connect the dosimeter to the electrometer in order to eliminate background noise interference. A bias voltage was provided by the Dose 1 electrometer. The experimental setup is shown in Fig 4.3.

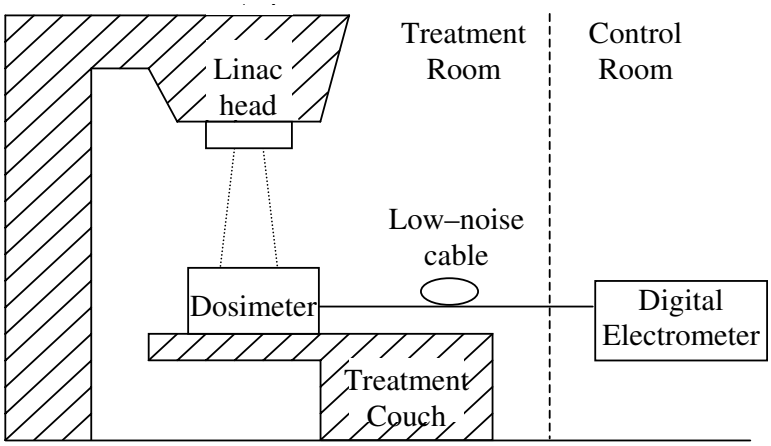

(a)

(b)

(c)

(d)

Figure 4.3: Experimental setup at the Grand River Regional Cancer Centre (a) a schematic diagram, (b) treatment room where the chamber was placed on the treatment couch under the linac head, (c) control console in the control room, and (d) electrometer

4.4 Dosimeter Characterization

Experiments on the signal saturation characteristic, linearity, and electrode separation were performed to test the proposed chamber. The experimental parameters used in the measurements are summarized in Table 4.1.

4.4.1 Signal Saturation Characteristic

Signal saturation curve measurements were performed by varying the bias voltages from 0 to 500 V at different electrode separations and doses. In Fig 4.4 (a) and (b), the collected charges initially had a sharp increase with an increase in the bias voltage. When the bias voltage was at 100 V and above, the increase in the collected charge reached a plateau and became nearly saturated. When the bias voltage was set at 300 V, the chamber could be operated in the near saturation regime up to a 5 mm electrode separation with 100 MU. It is expected that a small bias voltage induces only a weak electric field between the electrodes. Such a weak field cannot reduce the recombination effect of the electrons and holes significantly, and therefore, it results in a loss of signal. However, by increasing the bias voltage, the electric field becomes stronger and the chamber is able to collect more electrons and holes before the onset of the electron and hole recombination. This causes the saturation effect as observed in Fig 4.4 (a) and (b).

Moreover, the dosimeter was operated in the near saturation regime at a bias voltage of 300 V in all scenarios. The measurements presented in section 4.4.2 and 4.4.3 were performed with a bias voltage of 300 V.

Table 4.1: Experimental parameters in the measurements of the proposed parallel plate ionization chamber

	Signal saturation characteristic	Linearity	Electrode separation	Square-shaped CNT electrode	Irregular-shaped CNT electrode
Beam energies (MV)	6	6, 15	15	6	6, 15
(SSD) (cm)	100	100	100	100	100
Monitor Units (MU)	5, 50, 100, 200	2 to 600	100	100	100
Field sizes (cm^2)	5×5	5×5	5×5	5×5	1×1, 5×5
Bias voltages (V)	0 to 500	300	300	0 to 600	0 to 600
Electrode separations (mm)	0.5, 2, 5,10	2	0.5 to 5	2	2

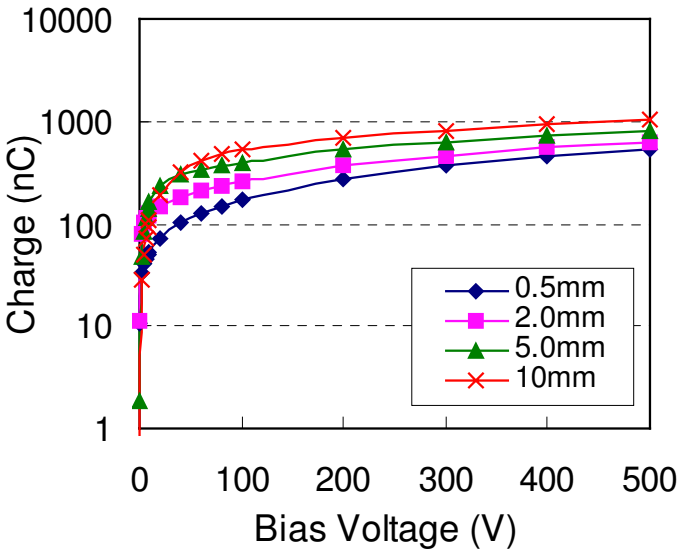

(a)

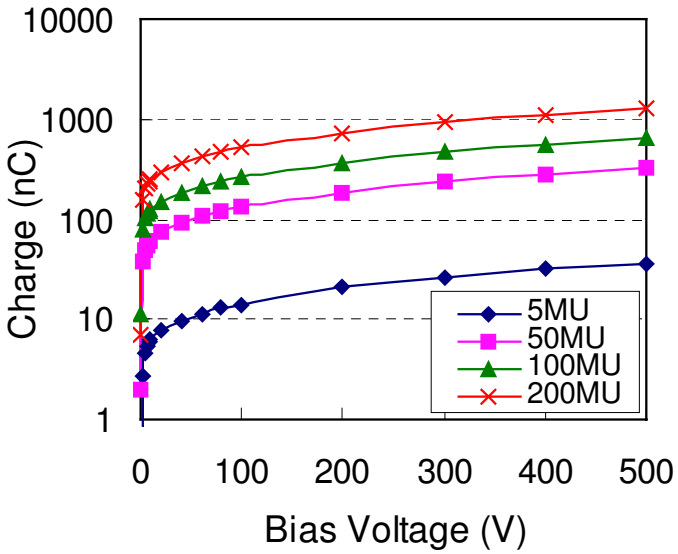

(b)

Figure 4.4: Signal saturation curves of the chamber (a) in different electrode separations at 100 MU and (b) in different doses with a 2 mm electrode separation

4.4.2 Linearity

For signal response linearity measurements, the dosimeter was setup with a 2 mm electrode separation and irradiated with a dose range from 2 to 600 MU for both the 6 and 15 MV photon beams. The readings of the chamber are plotted in Fig 4.5. The chamber displayed excellent linear responses.

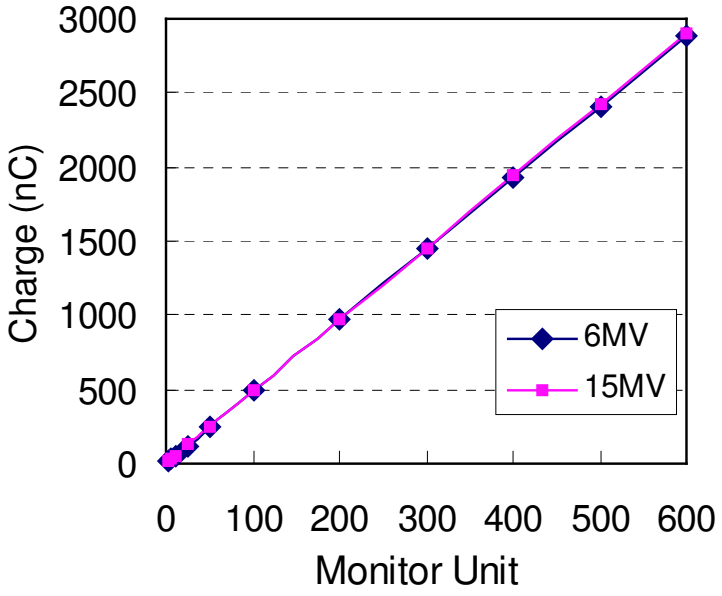

Figure 4.5: Linearity measurement of the proposed chamber

4.4.3 Electrode Separation

One advantage of the proposed chamber is that the separation of the two electrodes can be precisely controlled from 0.2 mm to 50 mm, which offers a good opportunity to examine the relationship between the active volume (the active volume has a linear relationship with the electrode separation distance) and the collected charges. Fig 4.6 shows the relationship between the electrode separation distance

and the collected charge.

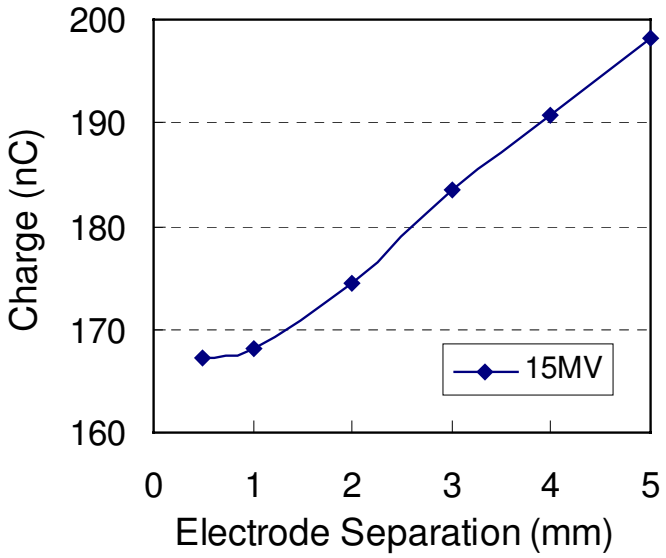

Figure 4.6: Relationship between the electrode separation distance and collected charge

The increase in electrode separation leads to an increase in the chamber active volume. As a result, more gas molecules are enclosed within the chamber. When high-energy photons enter the chamber, more electrons and holes are produced within the larger active volume, which in turn results in a larger signal. Therefore, the active volume has a significant effect on the amplitude of the detected signals. Similar results were reported by Rawlinson et al. [102].

4.5 Dosimeter with CNT Electrodes

According to the results reported in [97], we expected that the bias voltage of the parallel plate ionization chamber could be lowered if vertically aligned CNT films

were used as electrodes. The sharp tips of the CNTs can generate a very high electric field inside the chamber at relatively low voltage. Therefore, the chamber can be operated with low bias voltage while the ionization collection efficiency is not reduced. In this section, two different CNT electrode designs are presented, and the experimental results are discussed.

4.5.1 Dosimeter with Square-Shaped CNT Electrodes

A schematic diagram of a square-shaped electrode with CNTs grown on top is shown in Fig 4.7.

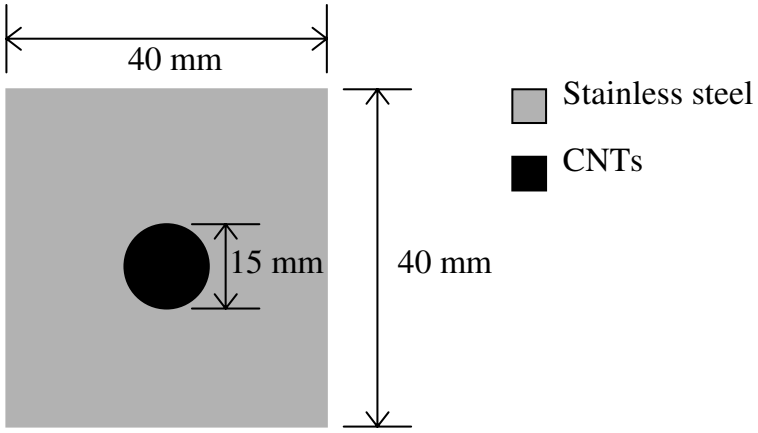

Figure 4.7: Square-shaped CNT electrode design

A circular shape CNT layer with a 15 mm diameter was grown in the centre of the stainless steel substrate. The CNT layer was grown by Xintek, Inc.. Fig 4.8 exhibits a SEM image of the microstructure of the CNTs, which was taken by using a JEOL JSM - 6460 SEM. As shown in Fig 4.8, the CNTs were randomly oriented instead of vertically aligned, and catalysts and impurities can be found

in the CNT layer. This type of CNT film was the only available sample at the time of the parallel plate ionization chamber experiments. The substrate and the size of the CNT layer were also restricted by the availability of the product offered by the company.

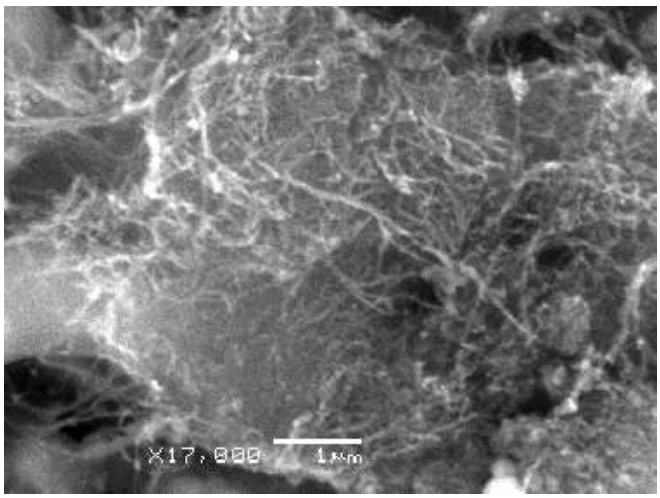

Figure 4.8: SEM image of the CNT sample grown by Xintek, Inc.

The saturation characteristics of the chamber with the CNT electrodes were measured by using 6 MV photon beams with a 5×5 cm^2 field size. The chamber was placed at a 100 cm SSD and 5 cm away from the central axis of the beams. A 100 MUs dose was delivered. As control experiments, stainless steel electrodes without CNTs were used for comparison.

Fig 4.9 shows the saturation curves of the chamber with and without the CNT layer. In Fig 4.9, the two saturation curves are very close to each other. The collected charges of the CNT-based ionization chamber are slightly smaller than those of the control chamber. The saturation voltage of the CNT-based chamber was not lowered due to the existence of the CNTs on the electrodes. There are two possible reasons for this result. First, as observed in the SEM image of the

CNT sample (Fig 4.8), there were many catalysts and impurities in the CNT layer. These catalysts and impurities may reduced the collection efficiency of the chamber. Second, since the CNT layer covered only a part of the stainless steel electrode, the electric field inside the chamber became non-uniformed due to the junction of the CNT layer and the electrode. In order to eliminate the effect of the non-uniform electric field on the ionization collection efficiency, an irregular-shaped electrode design was proposed. It should be noted that no visible damage to the CNTs was observed by the SEM after the experiments.

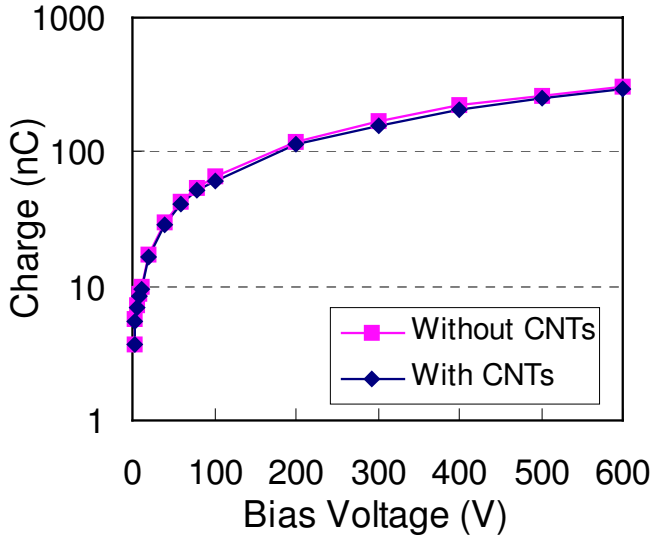

Figure 4.9: Saturation curves of the chamber with the square-shaped CNT electrodes

4.5.2 Dosimeter with Irregular-Shaped CNT Electrodes

Fig 4.10 is a schematic diagram of the irregular-shaped CNT electrode. In this design, a CNT layer covers the most parts of the electrode. The rectangular edges

of the substrate are designed so that the CNT electrodes can be embedded into the PMMA electrode holders.

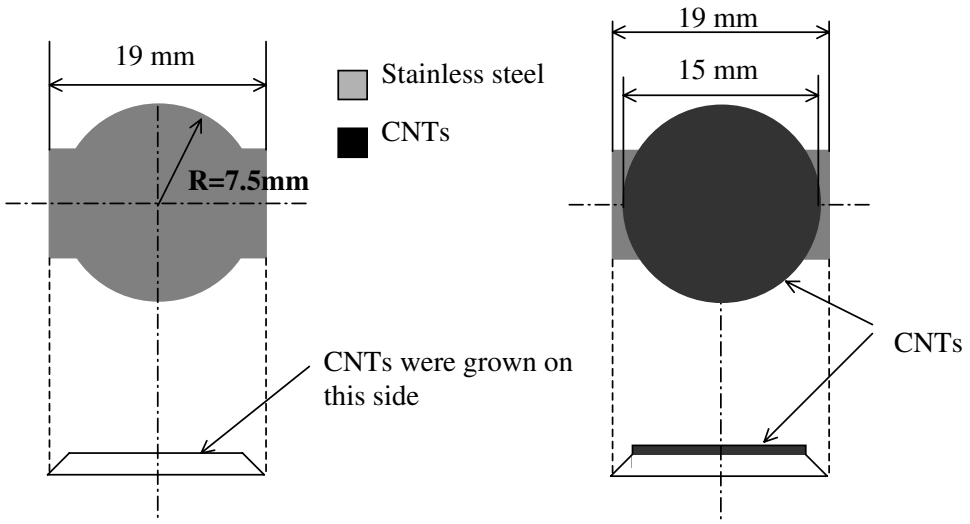

Figure 4.10: Irregular-shaped CNT electrode design (a) before growing the CNTs and (b) after growing the CNTs

The saturation characteristic measurements were performed by varying the bias voltages from 5 to 600 V. A 100 MUs dose was delivered for both the 6 and 15 MV photon beams. An 1×1 cm^2 field size was chosen for the 6 MV beams, and a 5×5 cm^2 field size was selected for the 15 MV beams. The results are shown in Fig 4.11.

For both the CNT-based ionization chamber and the control chamber, the collected charges increase as the bias voltage increases. However, for a given bias voltage, the CNT-based chamber has smaller collected charges. This result shows that the catalysts and impurities in the CNT layer may reduce the collection efficiency of the chamber.

The bias voltage of the CNT-based parallel plate ionization chamber was not

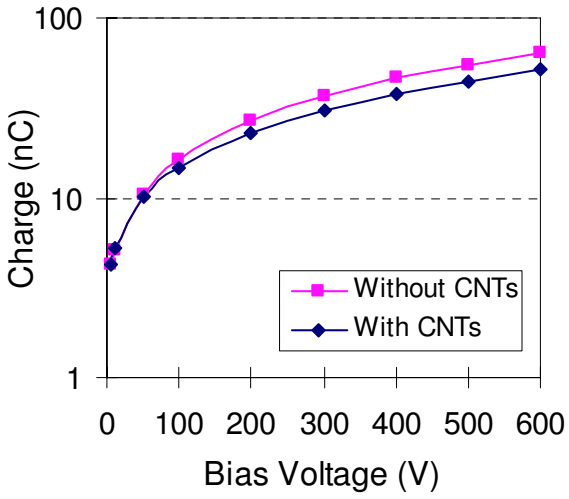

(a)

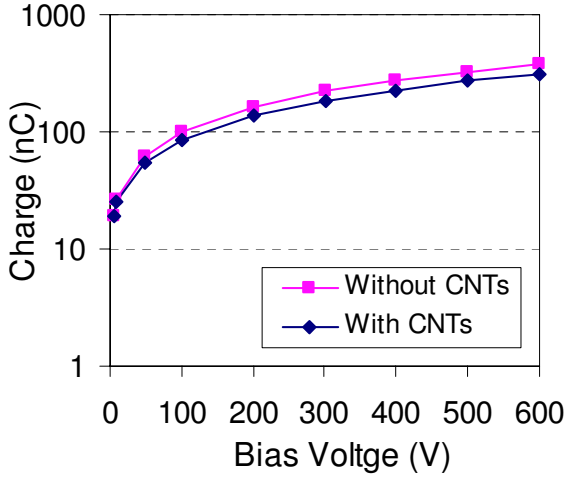

(b)

Figure 4.11: Saturation characteristic of the chamber with the irregular-shaped CNT electrodes (a) 6 MV photon beams with a 1 × 1 cm^2 field size and (b) 15 MV photon beams with a 5 × 5 cm^2 field size

lowered as expected with the square- and irregular-shaped CNT electrodes. Vertically aligned CNTs in place of the randomly aligned CNTs may be appropriate for electrodes in the future. In addition, proper purification steps need to be taken to purify the CNT layer. It is anticipated that the use of the purified and vertically aligned CNTs will improve the collection efficiency of the ionization chamber. The miniaturized ionization chamber with CNT electrodes can be used for high spatial resolution measurements in IMRT. The CNT-based ionization chamber with high ionization collection efficiency is expected to provide good signals when small dose is delivered. This will be one of the future research directions.

4.6 Conclusions

A customized parallel plate ionization chamber was designed and fabricated to study the ionization collection efficiency of CNTs. A set of measurements, such as the signal saturation characteristic, signal response linearity, and electrode separation distance, were performed to characterize the proposed chamber. Two designs of CNT electrodes, square- and irregular-shaped, were proposed. The saturation characteristics of the chamber with the CNT electrodes were measured. It is found that the catalysts and impurities within the CNT layers can reduce the collection efficiency of the ionization chamber. Vertically aligned CNTs are expected to improve the performance of the chamber.

Chapter 5

Dosimeters and Dosimeter Arrays Based on Resistance Change

5.1 Introduction

This chapter presents dosimeters and dosimeter arrays based on resistance change. Carbon fibre sheets and CNT films are used as the sensing materials. In section 5.2, a carbon fibre sheet-based dosimeter is presented, including the structure of the dosimeter and the dosimeter's responses regarding the dose rate, dose, and field size measurements. Section 5.3 describes dosimeters based on CNT films. The fabrication process of the CNT films is illustrated. Percolation theory is used to explain the percolative conductivity of the dosimeter followed by discussions of the dosimeter's performance. A transparent and flexible dosimeter is also demonstrated in this section. A CNT-based film dosimeter array system is presented in section 5.4. The design and fabrication of the dosimeter arrays, readout circuit, and user interface are explained in sequence. After the performance of the dosimeter arrays is discussed, the CNT-based film

dosimeters are compared with commonly used dosimeters. Conclusions are given in section 5.5.

5.2 Carbon Fibre Sheet-Based Dosimeter

Carbon fibres are an important class of graphite-related materials, which are closely connected to CNTs with regard to structures and properties. Carbon fibres have been well known for their structural applications (which are related to aerospace structures [104], aircraft brakes [105], and concrete structures [106]) and thermal applications (which are related to heat conduction [107] and thermal insulation [108]) due to the high strength to weight ratio and low coefficient of thermal expansion.

Nowadays, synthesis techniques for carbon fibres are very mature. Carbon fibres with different diameters, morphologies, and properties are commercially available. Therefore, in this study, besides exploring the use of CNTs as sensing materials in radiation dosimetry, carbon fibres are also investigated for applications in dosimetric measurements.

5.2.1 Dosimeter Design and Fabrication

Fig 5.1 is a schematic diagram of the carbon fibre sheet-based dosimeter design. Because the carbon fibre sheet is very brittle, two plastic holders, each having a 1.8×1.8 cm^2 hole, were used to form a sandwich structure in order to support the carbon fibre sheet. The size of the hole on the PMMA holders defines the opening area that directly exposed to the radiation. Copper electrodes were used as electrical contacts with the carbon fibre sheet.

The resistance of the carbon fibre sheet is determined to be 1.5 Ω at room

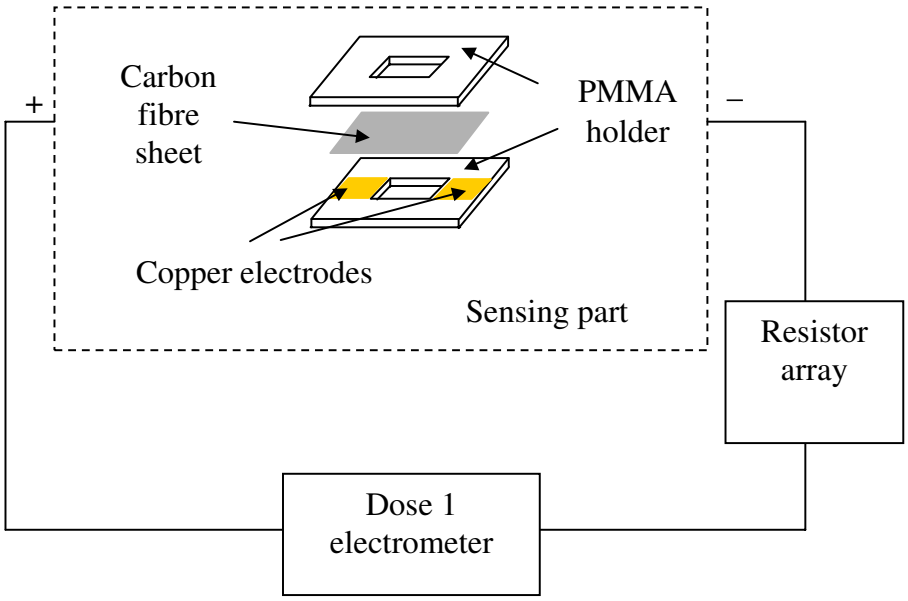

Figure 5.1: Carbon fibre sheet-based dosimeter design

temperature. In order to lower the initial current, a resistor array with an equivalent resistance of 592 MΩ was connected in series with one electrode of the sandwich structure. Another electrode was connected to the Dose 1 therapy digital electrometer, which provided 10 V to the circuit and measured the signals. The initial current within the circuit was around 16.47 ± 0.01 nA. The current had a small fluctuation in the level of 10 pA, which was the background noise. The ionizing radiation produces a current change on the carbon fiber sheet. This change in the current is the signal measured by the dosimeter. The typical current change measured by the carbon fiber sheet-based dosimeter is of the order of one hundred picoampere. Therefore the signal to noise ratio of the carbon fiber sheet-based dosimeter is greater or equal to 10:1.

The carbon fibre sheet is supplied by E-TEK, Division of DeNora. Fig 5.2

displays the microstructure of the carbon fibre sheet. The scale bar shown in the picture is 50 μm.

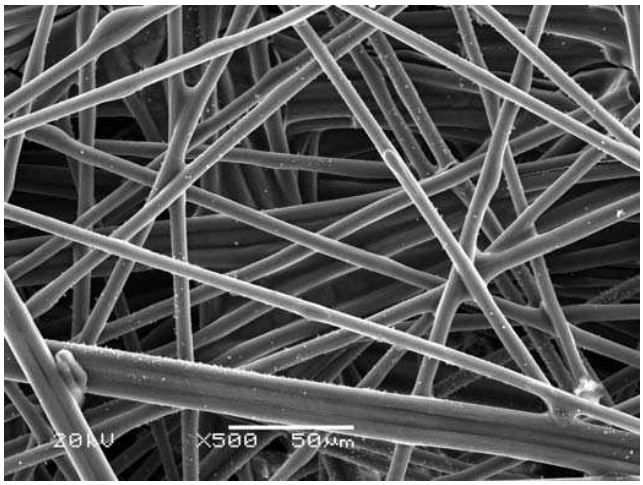

Figure 5.2: SEM image of the carbon fibre sheet

The carbon fibre sheet consists of carbon atoms with the atomic number (Z) equal to 6. Therefore, the carbon fibre sheet is a low Z material, which means that the carbon fibre sheet-based dosimeter can be used as a tissue equivalent detector. Moreover, carbon is non-toxic inside the body; thus, a carbon fibre radiation dosimeter is compatible with body tissue and has the potential to be implanted inside the human body. These properties will allow the carbon fibre radiation dosimeter to be used in intracavitary brachytherapy.

5.2.2 Experimental results

The dose rate, dose, and field size measurements were conducted to test the carbon fibre sheet-based dosimeter. The experimental parameters used in the measurements are summarized in Table 5.1.

Table 5.1: Experimental parameters in the measurements of the carbon fibre sheet-based dosimeter

	Dose rate measurements	Dose measurements	Field size measurements
Photon beam energies (MV)	6, 15	6	6, 15
Source-to-surface distance (SSD) (cm)	100	100	100
Monitor Units (MU)	100	Vary from 100 to 600	100
Dose rates (MU/min)	Vary from 100 to 600	600	600
Field sizes (cm^2)	1×1, 1.8×1.8	1.8×1.8	Vary from 0.5×0.5 to 1.8×1.8

Dose Rate Measurement

The linac can be operated at several different dose rates. The results of dose rate measurement are shown in Fig 5.3, where the dose rates varied from 100 to 600 MU/min for the field sizes of 1 × 1 cm^2 and 1.8 × 1.8 cm^2.

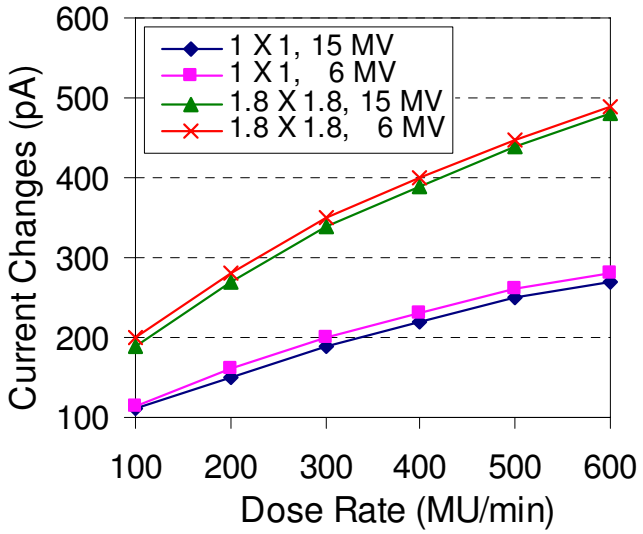

Figure 5.3: Current change associated with the dose rate for the 6 and 15 MV photon beams with the field sizes of 1 × 1 cm^2 and 1.8 × 1.8 cm^2

For a given field size, the changes in the amount of current passing through the carbon fibre sheet increase with an increase of the dose rate for both the 6 and 15 MV photon beams. Similar to the phenomena that were observed in diamond dosimeters [109, 110, 111], the results are explained as follows. When the carbon fibre sheet is irradiated by the MV photon beams, the absorption of the ionizing radiation induces a temporary change in the electrical conductivity of the carbon fibre through the production of electrons and holes. Under the influence of the

current passing though the carbon fibre sheet, the electrons and holes move in the opposite directions. Their movements reinforce the initial current inside the circuit. As a result, the current passing through the carbon fibre sheet increases when the photon beams are ON and returns to the initial value when the beams are OFF. The current changes depend on the intensity of the photon beams, which is determined by the dose rate of the linac.

Dose Measurement

For the dose measurement, the dosimeter was irradiated with a dose range from 100 to 600 MU for the 6 MV photon beams. The results are given in Fig 5.4.

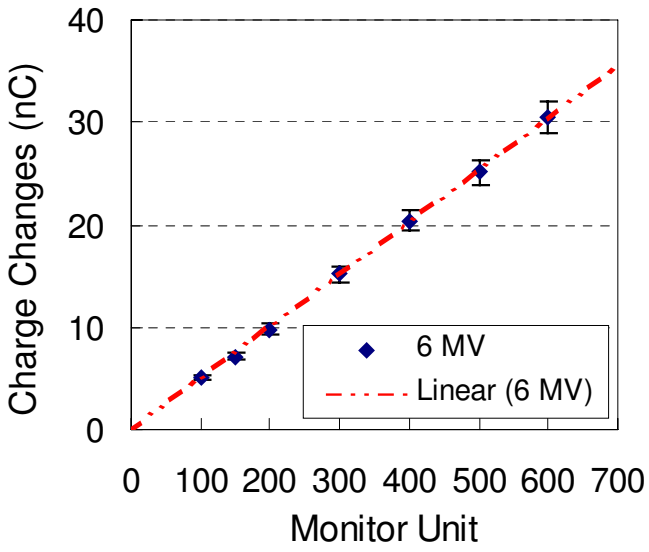

Figure 5.4: Response of the carbon fibre sheet-based dosimeter (nC) in relation to monitor unit

The variation of charge is directly proportional to the given dose. The dash dot line in Fig 5.4 is a linear fit to the measurement by

$$\Delta Q = \alpha D, \tag{5.1}$$

where $\alpha = 5.06 \times 10^{-2}$ nC/MU, ΔQ is the change of the charge, and D is the dose. The deviation bars in Fig 5.4 are 5%. For the given dose range from 100 to 600 MU, the dosimeter displayed an excellent linear response. To verify the experimental results, the changes of charge can also be calculated. The current integrated by the time (which is equal to the time duration when the beam was ON) is the charge passing through the carbon fibre sheet. Since the time duration that the beam was ON is determined by the dose (the larger the dose chosen, the longer the delivery time), the changes of the charge are calculated by

$$Q = \int i(t)dt \Longrightarrow \Delta Q = \int \Delta i(t)dt. \tag{5.2}$$

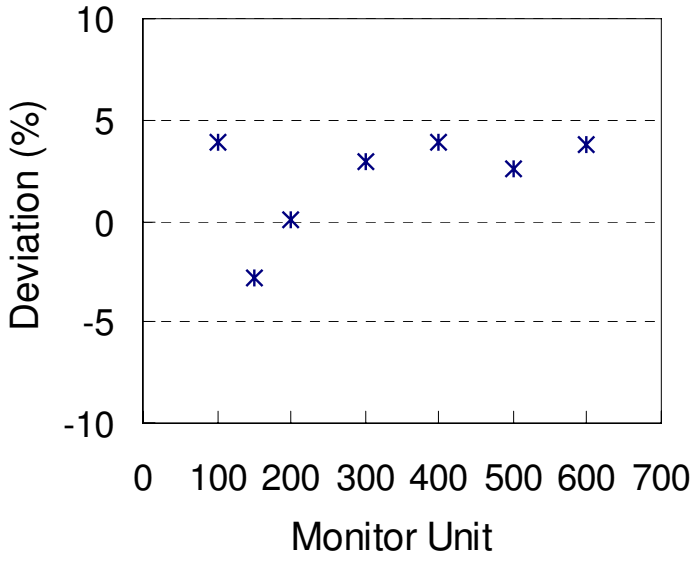

Figure 5.5: Deviation between the measurements and calculations

In Fig 5.3, it is seen that, when the field size is 1.8×1.8 cm^2, the average current change is 0.49 nA for the 6 MV photon beams with a dose rate equal to

600 MU/min. Then ΔQ can be simply calculated by

$$\Delta Q = 0.49 * t, \tag{5.3}$$

where t is the beam ON time. Fig 5.5 reveals the deviation between the measurements and calculations. The corresponding data are listed in Table 5.2.

Table 5.2: Changes of charge (ΔQ) to different monitor units

Monitor Units	Measurements	Calculations	Deviation (%)
100	5.100	4.90	3.92
150	7.150	7.35	-2.80
200	9.805	9.80	0.51
300	15.150	14.7	2.97
400	20.400	19.6	3.92
500	25.150	24.5	2.58
600	30.550	29.4	3.76

Field Size Measurement

The field size measurements were conducted by varying the size of a square field from 0.5×0.5 cm^2 to 1.8×1.8 cm^2. A dose of 100 MUs was delivered at a dose rate of 600 MU/min for both 6 and 15 MV photon beams.

In Fig 5.6, it can be seen that the changes of the current passing through the carbon fibre sheet increase with an increase of the field size. This result occurs because increasing the field size means more carbon fibres are exposed to

the radiation. Since the sensing area of the dosimeter increases, the dosimeter measures larger change in the current.

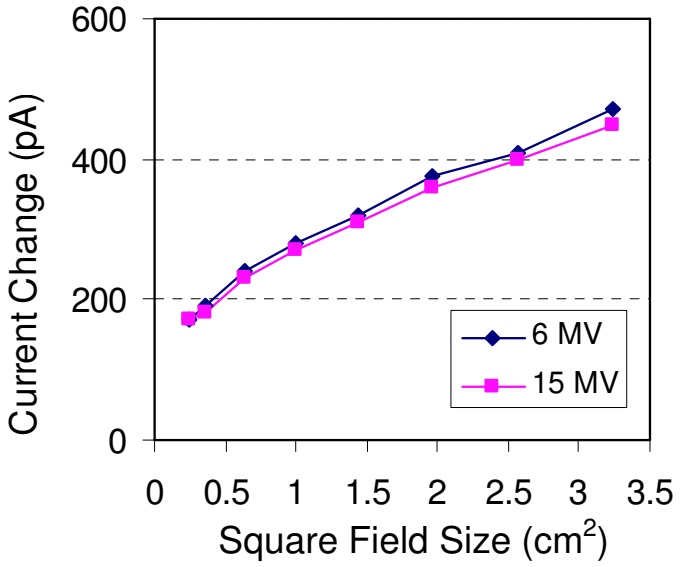

Figure 5.6: Current change in relation to the field sizes of the 6 and 15 MV photon beams at 600 MU/min dose rate

5.2.3 Summary

A dosimeter with a carbon fibre sheet as the sensing material was designed and fabricated to study the properties of the carbon fibre under MV photon beam irradiation. The sensing area of the dosimeter is 1.8×1.8 cm^2. This dosimeter can be used for the dosimetric measurements and real-time dose rate monitoring. Changes in the current passing through the carbon fibre sheet indicate the dose rate changes, while the charge changes reflect the dose differences. The experimental results showed that the carbon fibre sheets can be used for MV photon beam measurements. In addition, the sensing area of the proposed

dosimeter can be reduced to 5×5 mm^2. The miniaturization of the current design provides the possibility of a carbon fibre sheet-based dosimeter with a higher spatial resolution.

5.3 Carbon Nanotube-Based Film Dosimeter

Devices based on a single CNT exhibit a superior performance due to the unique electrical and mechanical properties of the nanotubes as introduced in chapter 3. However, the reproducibility of the single tube devices remains a challenge because the properties of a CNT are determined by its chirality and diameter. Unfortunately, the chirality and geometry of the CNTs still cannot be controlled in current CNT synthesis processes. In addition, for the devices based on single nanotube, the CNT must be positioned precisely in a certain location in order to connect with other electrical or mechanical parts. With current assembly and patterning technologies, precise positioning cannot be conducted efficiently.

In contrast, the research on CNT films opens up new avenues for CNT-based device manufacturing. Recent studies show that CNT films can be used in diodes and field effect transistors (FETs) [100, 112], gas sensors [113], field emission devices [114], and transparent conductive coatings [115]. CNT films can be formed on substrates by using different methods, including drop casting from solvents [116], spin coating [117], spray coating [114], and vacuum filtration [115]. In this section, dosimeters based on CNT films are presented to explore the usage of CNT films as a sensing material for radiation measurements.

5.3.1 Dosimeter Design and CNT Film Formation

A schematic drawing of a CNT-based film dosimeter design is shown in Fig 5.7. The dosimeter mainly consists of a CNT film as the sensing material and two copper electrodes for the electrical contacts. Purified HiPco SWNTs were selected for the film preparation. The average diameter of the CNTs is 2 nm, and the average length is 2 μm. The CNT films were made on transparent glass substrates.

A suspension of CNTs was prepared with a concentration of 0.1 mg/mL of CNTs in deionized (DI) water. The suspension was ultrasonicated for 30 minutes using a probe ultrasonicator (Hielscher® UP200S) and then used immediately.

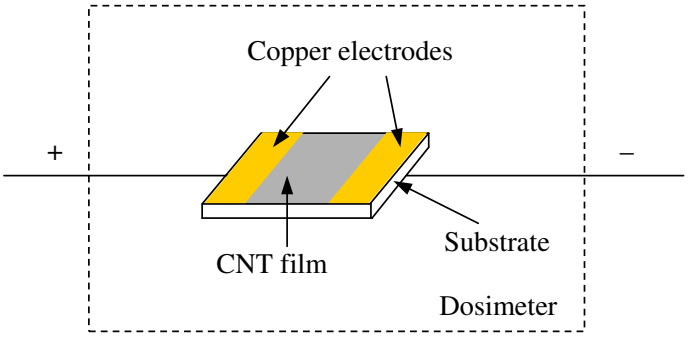

Figure 5.7: CNT-based film dosimeter design

Before the ultrasonication, the CNTs tended to stick together and floated on the surface of the DI water. The color of the water body is very clear. After 5 minutes of ultrasonication, the CNTs started to spread in the water. With longer duration of ultrasonication, the CNTs spread evenly in the water. After 30 minutes, the colour of the suspension became evenly dark, and a uniform CNT suspension was obtained.

After the ultrasonication step, a spin processor (Laurell® WS-400 LITE Series) was used to spin the suspension on the glass substrates. The spin processor was operated at 6000 rpm for 60 seconds for one CNT layer. Then, the substrates with the CNT layer were heated at 100 ^{o}C for 10 minutes. After the water evaporated, the CNTs were left behind on the surface of the substrates to form a thin layer of film. The CNT films resided on the substrate well because of the hydrophobic properties of the CNTs. The density of the CNTs in the film can be controlled

by spinning different numbers of CNT layers on the substrate. Fig 5.8 shows the SEM images of the CNT films with different densities. Fig 5.8 (a), (b), and (c) show the density of the CNTs in the films when 3, 5, and 10 layers of CNTs were deposited, respectively.

The spin and heating processes were repeated until the desired film density was achieved. It is noteworthy that the suspension was kept ultrasonicating during the CNT film formation and heating processes so that the CNTs in the suspension could not congregate.

After the formation of the CNT film on the substrates, two parallel copper electrodes were made on the top of the film at a distance of 20 mm. The fabrication process of the CNT-based film dosimeters is summarized in Fig 5.9.

5.3.2 Percolative Conductivity of CNT Films

The electrical performance of CNT-based film devices is highly dependent on the properties of the CNT film. Therefore, it is essential to understand the effect of various factors, such as the length and density of the CNTs, on the properties of the film.

In this study, the average length and the density of CNTs in the film is considered to determine the effect of percolation on electrical conductivity in the CNT-based film dosimeters. A model based on the percolation theory is used to study how the average length and density of CNTs in the film can influence the electrical conductivity of the film.

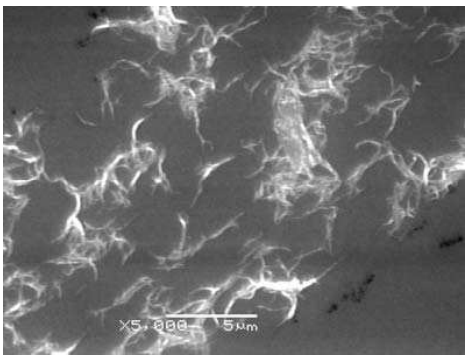

(a)

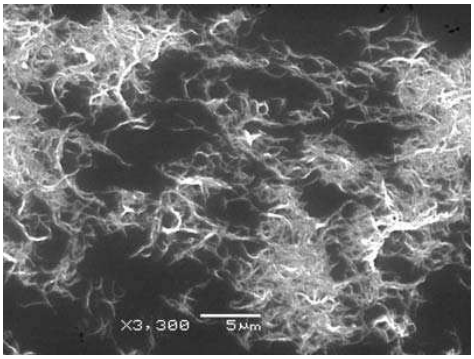

(b)

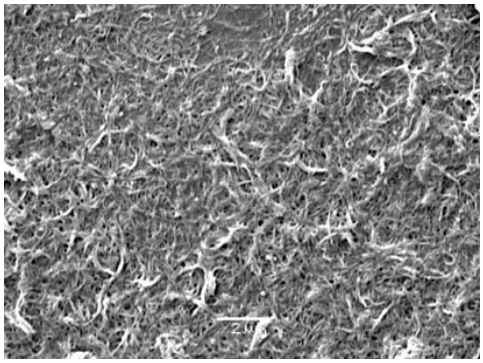

(c)

Figure 5.8: SEM images of CNT films with different numbers of CNT layers (a) 3 layers, (b) 5 layers, and (c) 10 layers

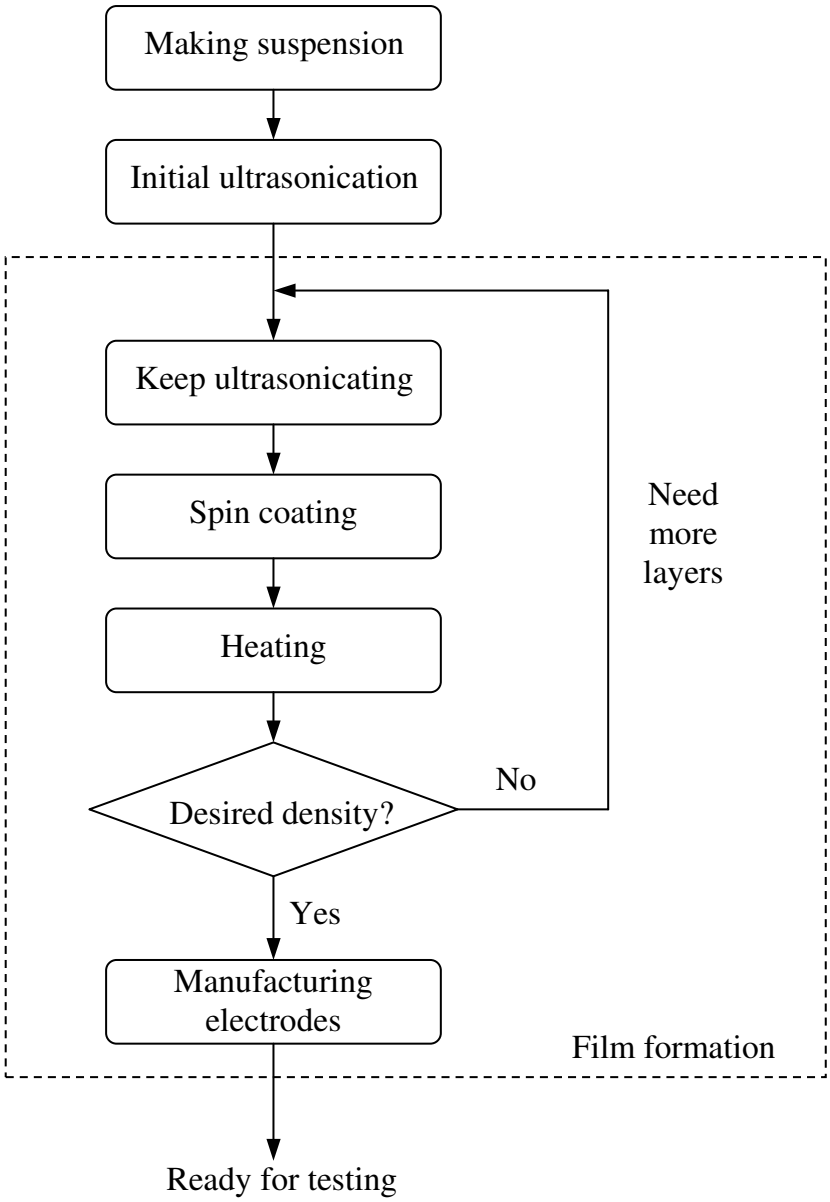

Figure 5.9: Flowchart of the CNT-based film dosimeter fabrication process

Percolation Theory

Using percolation theory to study the conductivity and related properties has been going on for decades [118, 119]. Recent research shows that the percolation theory can also be applied to study the conductivity of CNT network films [120, 121, 122, 123].

The CNTs shown in Fig 5.8 suggest randomly oriented with no preferential directions and the length of the CNTs is much greater than their diameter. Therefore, the percolation theory of random distribution of the conducting network can be applied in this case. In the CNT films, because the nanotubes tend to be attracted to each other through van der Waals interactions, a small bundle of CNTs is considered as one conducting identity.

According to the percolation theory, the conductivity of the CNT network film is dependent on the density of the CNTs in the film, and is expressed as

$$\sigma \propto (N - N_c)^{\alpha}, \tag{5.4}$$

where σ refers to the conductivity of the CNT network film, N is the density of the CNTs in the film, N_c is the critical density corresponding to the percolation threshold, and α is the conductivity exponent, which is equal to 1.94 [118]. For the random distribution of the CNTs in the film, the critical density, N_c, gives the position of the phase transition, where the CNT network transits from a disconnected to a connected status. As a result, the electrical property of the CNT film changes gradually from nonconductive to conductive. The range where N_c falls into is called the percolation region.

Equation 5.4 holds close to the percolation region. When the CNT density is well beyond the critical density N_c, the conductivity of the CNT film is expected to be linearly dependent on the density.

The critical density is determined by the average length of the CNTs in the film and is given by

$$N_c = \frac{1}{\pi} \cdot (\frac{4.236}{l})^2, \tag{5.5}$$

where l is the average length of the CNTs in the film [123].

Critical Density vs. Average Length of CNTs

According to equation 5.5, the critical density of the CNTs in the film declines with the increase in the CNTs' average length in Fig 5.10. It is easy to understand that when the CNTs are long, the tubes have a higher possibility to connect to each other. Therefore, very few tubes are required to form conductive paths within certain area. By referring to equation 5.4, the conductivity of the film is related to the critical density, as a result, when the density of the CNTs in the film is a constant, the conductivity of the film is dependent on the average length of the CNTs in the film.

Conductivity vs. Average Length of CNTs

Fig 5.11 provides the results on the relationship between the average length of the CNTs and the conductivity of the film according to equation 5.4 and 5.5. The conductivity is converted to a sheet conductivity, which is defined as $1/\mathrm{R}_\square$. $\mathrm{R}_\square$ is the sheet resistance and is defined as

$$R_\square = R\frac{W}{L}, \tag{5.6}$$

where R is the resistance of the CNT film, W and L are the width and the length of the film, respectively.

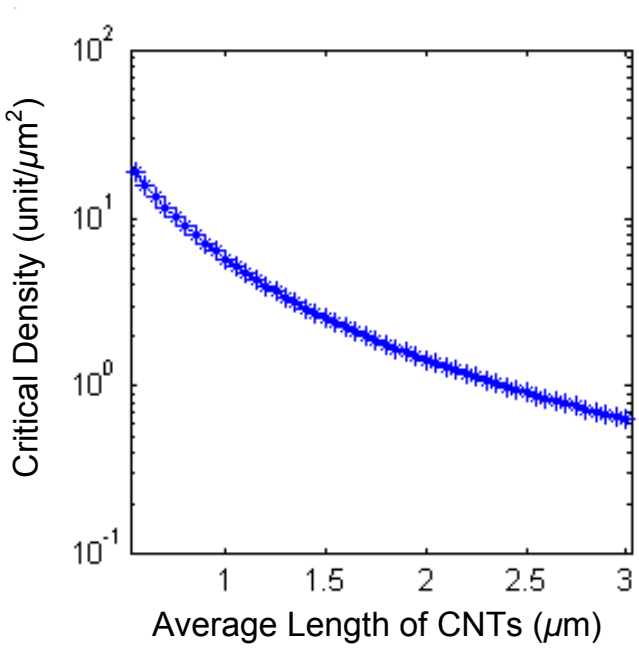

Figure 5.10: Critical density of the film decreases as the average length of CNTs in the film increases (from equation 5.5)

As seen in Fig 5.11, for a given CNT density (for example, 10 unit/μm^2), when the CNTs are shorter than the threshold length (around 0.5 μm), no continuous conductive path is formed; the film is, therefore, nonconductive. When the length of the CNTs reaches and exceeds the threshold length, the conductivity of the film shows a sharp increase. With further increasing in the CNTs' average length, the conductivity of the film reaches a plateau and the film becomes conductive. Given the CNTs' average length is a constant, the higher density of the CNTs in the film leads to a larger film conductivity.

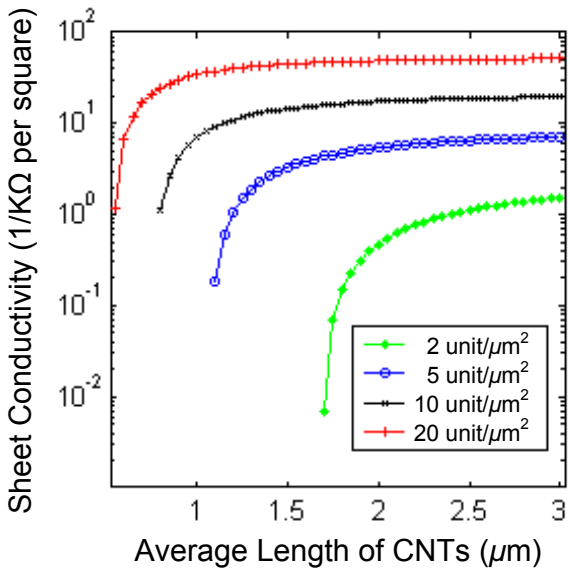

Figure 5.11: Relationship between the average length of CNTs in the film and the film conductivity (from equation 5.4 and 5.5)

Percolative Conductivity in the CNT-Based Film Dosimeter

In the CNT-based film dosimeter, a CNT film is employed as the sensing material. CNT films with different densities were made to study the percolative conductivity of the film. Table 5.3 lists four CNT-based film dosimeters and their corresponding CNT layers.

The CNT-based film dosimeters were placed on the treatment couch (carbon fiber table top) and under the accelerator head with a SSD of 100 cm. A bias voltage of 15 V was applied to the dosimeters. Ionizing radiation induced a change in the current passing through the CNT film when the dosimeter was irradiated. The current was measured by the Dose 1 therapy digital electrometer. Fig 5.12 shows the current changes of the film with 3 CNT layers when the 6 MV photon beams with different dose rates irradiated the CNT film.

Table 5.3: Dosimeters with different CNT densities

Dosimeter No.	Number of CNT layers
1	1
2	3
3	5
4	10

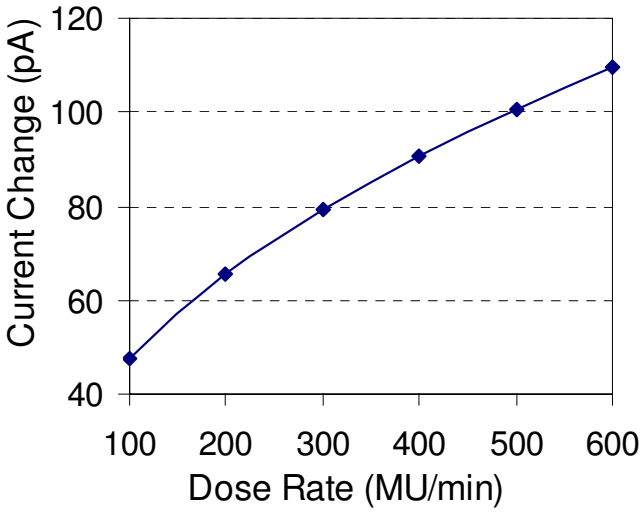

Figure 5.12: Current passing through the film with 3 layers of CNTs changes when the dosimeter was irradiated by the 6 MV photon beam with a field size of 1 × 1 cm^2

According to the Ohm's law, the current passing through a conductor is directly proportional to the voltage applied on the two ends of the conductor, and inversely proportional to the resistance of the conductor such that

$$I = \frac{V}{R}. \tag{5.7}$$

Since the bias voltage applied on the CNT film remains the same throughout the irradiation, the change of current is related to the change in conductivity of the CNT film. If ΔI represents the change of current, and ΔR represents the change of resistance, then ΔI is inversely proportional to ΔR. Thus,

$$\Delta I = \frac{V}{\Delta R}. \tag{5.8}$$

The variation of ΔI reflects the change of ΔR, which in turn reflects the change in the conductivity.

Fig 5.13 shows the responses of the four newly developed dosimeters with different CNT films (see Table 5.3). In this experiment, 6 MV photon beams with dose rates at 300, 400, 500, and 600 MU/min were used.

As observed in Fig 5.13, the current changes ΔI show the peak values on the film that is prepared with three layers of CNTs. This nonlinear scaling suggests that the 3-layer CNT film may be within the percolation region. According to equation 5.4, the film conductivity is exponentially dependent on the CNT density at the percolation region, which means that small changes in the CNT density can lead to significant variation of film conductivity. Because the film conductivity determines the amount of current passing through the CNT film, as a result, the current can vary significantly with the change of the CNT density. It should be noted that the low energy electrons from the linac head and the treatment couch might also affect the film conductivity. Further study is needed to investigate this issue.

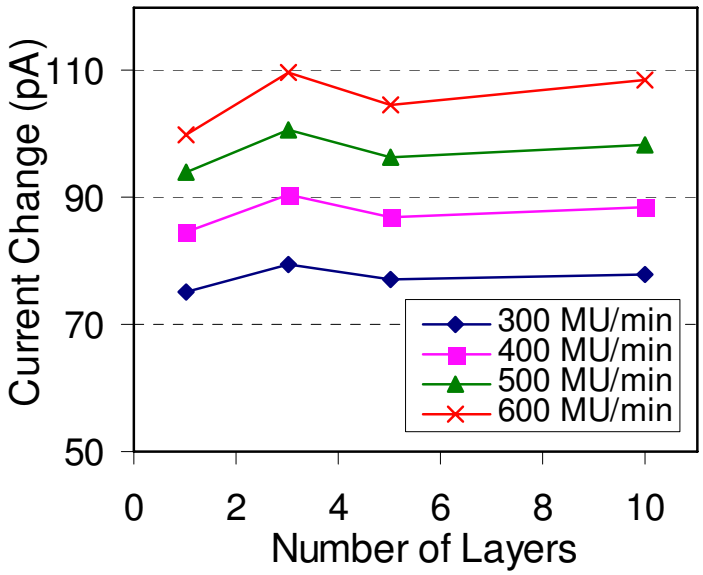

Figure 5.13: Current change passing through the films versus the number of layers of CNTs on the top of the substrate (6 MV photon beams with the field size of 1 $\times$ 1 cm^2)

The results of this experiment suggest that CNT-based film devices with the CNT film fabricated within the percolation region are expected to perform well. For the CNT-based film dosimeter, larger responses are achieved when the film consists of three layers of CNTs.

5.3.3 Experimental results

The responses of the dosimeters to ionizing radiation with different energies, dose rates, and field sizes were examined to assess the performance of the proposed dosimeter.

Responses to Electron Beams with Different Energies

In beam energy experiments, electron beams with 4, 6, 9, 12, and 16 MeV were used to irradiate the dosimeters with 100 MUs at a dose rate of 400 MU/min and field size of 2 × 2 cm^2. The experimental results are plotted in Fig 5.14.

Fig 5.14 (a) shows the responses of the dosimeters to the electron beams with different nominal energies. The changes of current passing through the CNT films increase with the increase of the electron beam energy. Refer to the percentage depth dose (PDD) curves of the electron beams with different energies provided by the Varian Clinac 21 EX medical linear accelerator (see Fig A.6 in Appendix 6), at depth of 0 cm, the relative surface dose increases as the beam energy increases. From the ratio of relative surface dose to the dose at calibration geometry of different beam energies in Appendix 7, one can calculate the relative surface dose, $D_{surface}$, when 100 MUs were delivered by the electron beams with different energies.

$$D_{surface}(cGy) = \frac{M_{surface}}{M_{calibration}} \times \frac{1cGy}{MU} \times 100MU. \tag{5.9}$$

Fig 5.15 plots the current change of the dosimeters versus the relative surface dose in water. The four CNT-based film dosimeters exhibit good linearity to surface dose. The results are in agreement with the fact in Fig A.6.

In addition, it can be seen from Fig 5.14 (b) that for a given electron beam energy, the CNT film with three layers of CNTs shows the largest responses compared with the other three films. This result is in accordance with the results discussed in section 5.3.2 and further confirms that the CNT film fabricated within the percolation region shows a better performance responding to the input signals.

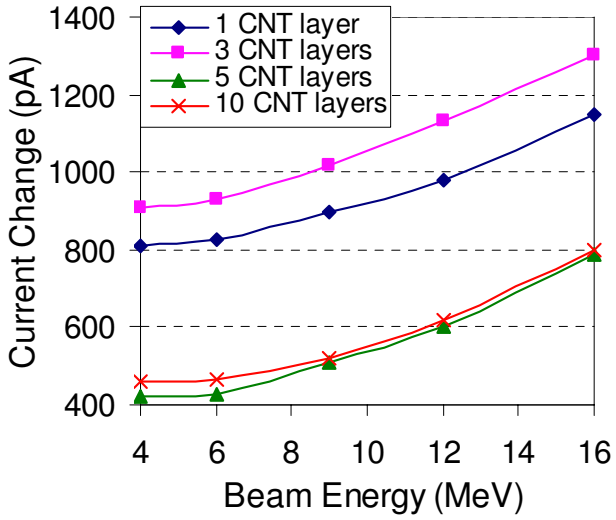

(a)

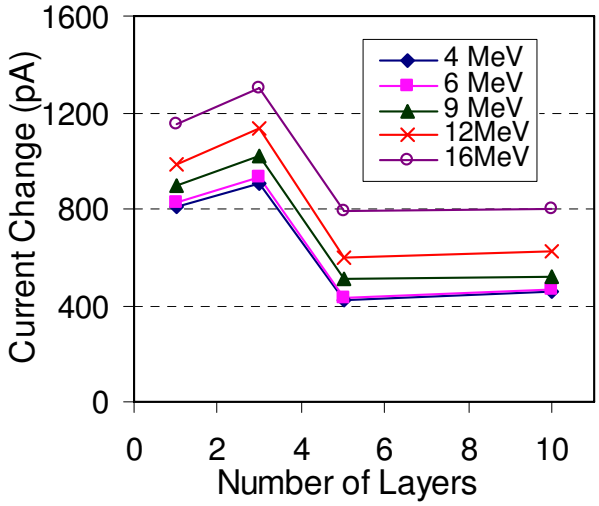

(b)

Figure 5.14: (a) Dosimeter responses to electron beams with different nominal energies at 400 MU/min dose rate and 2 × 2 cm^2 field size (The apparent energy dependence is resolved in Fig 5.15 with surface dose) and (b) Current change of the films versus the number of layers of CNTs at different electron beam energies at 400 MU/min dose rate and 2 × 2 cm^2 field size

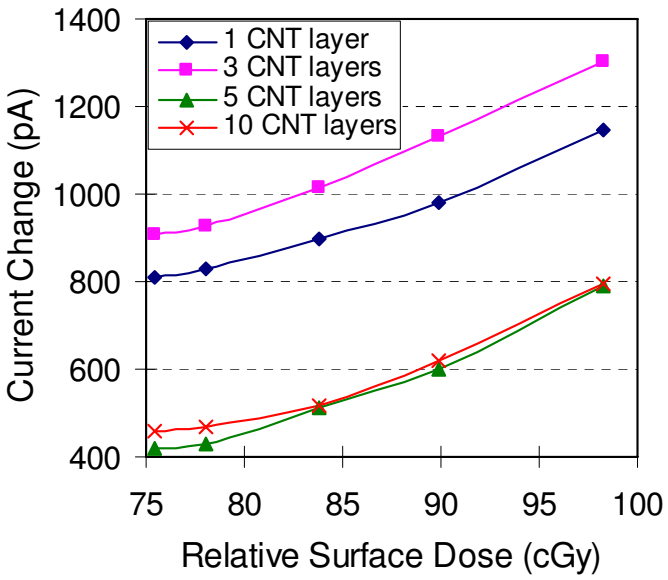

Figure 5.15: Current change of the dosimeters versus relative surface dose in water. Each curve has been constructed with the data from 4, 6, 9, 12, and 16 MeV electron beams demonstrating beam energy independence and approximate linear dependence of current change with dose.

Dose Rate Measurement

In the dose rate measurement, both photon beams and electron beams were used. Fig 5.16 (a) shows the responses of the four CNT-based film dosimeters to the 6 MV photon beams with the dose rate varying from 100 MU/min to 600 MU/min in the step of 100 MU/min. Fig 5.16 (b) shows the responses of dosimeter 2 and dosimeter 4 to the 4 MeV electron beams with the dose rates at 100, 200, 300, 400, 500, 600, and 100 MU/min.

In both Fig 5.16 (a) and (b), the ionization current increased with the increase of the dose rate. In addition, the current changes induced by the electron beams were much larger than those induced by the photon beams. This phenomenon is

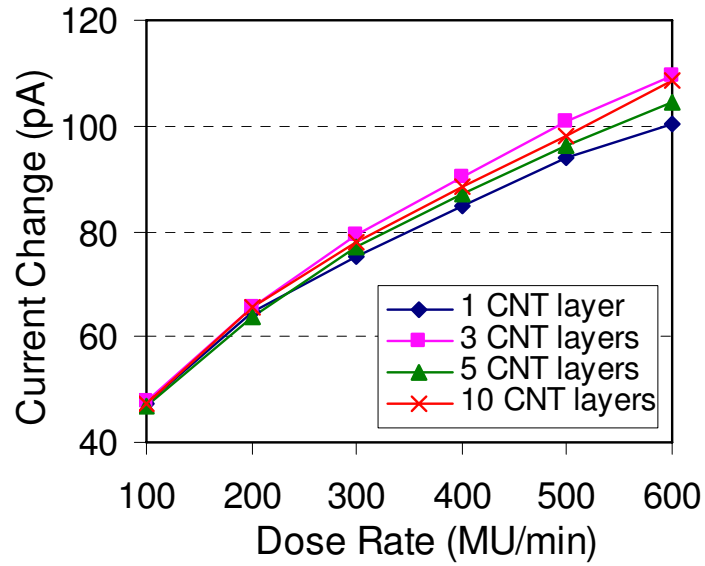

(a)

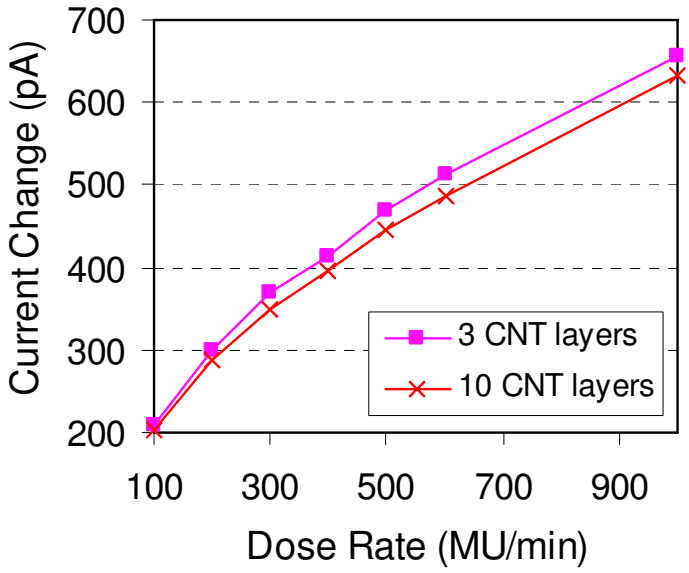

(b)

Figure 5.16: Current change passing through the CNT films increases with the increase of the dose rate for (a) 6 MV photon beams with 1×1 cm^2 field size and (b) 4 MeV electron beams with 2×2 cm^2 field size

explained as follows.

Megavoltage photon beams are more penetrating than electron beams and, in general, travel much further before interacting in a medium (mean free path = 1/(linear attenuation coefficient)). Photon interactions result in the production of high-energy electrons via photoelectric, Compton, or pair production processes. The electrons then go on to deposit their energy in the medium via collisions and excitation.

The dosimeters described in this thesis were used to measure surface dose with no buildup, which is the most stringent conditions of operation (the lowest signal to noise ratio). Under these conditions the surface dose for photons is several times lower than for electrons. This is shown in Appendix 7. Hence the dose measured from electron beams is approximately 4 times greater than for the dose measured from photon beams.

Field Size

Field sizes were varied from 0.4 × 0.4 cm^2 to 2.0 × 2.0 cm^2 in the field size measurement. Both 6 and 15 MV photon beams were used in this experiment. The dose rate was 400 MU/min. As shown in Fig 5.17, the responses of the CNT-based film dosimeters increased when the beam size became larger. This result is very similar to that of the carbon fibre sheet-based dosimeter. The reason is that with the increase of the field size, more CNTs are exposed to the radiation. As a result, the dosimeter measures larger change in the current due to the increase of the dosimeter's sensing area.

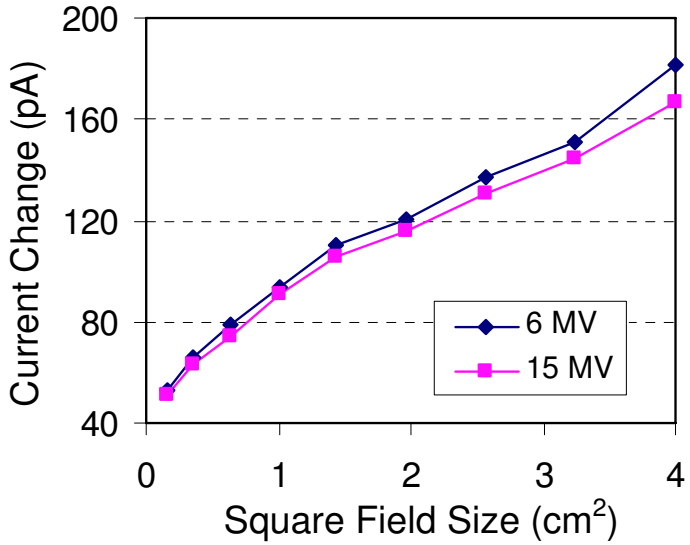

Figure 5.17: Current change increases when the field size of photon beams increases (6 and 15 MV photon beams delivered at 400 MU/min dose rate)

5.3.4 Absorbed Dose Calibration of the CNT-based Film Dosimeter

The CNT-based film dosimeter was dose calibrated using a parallel plate ionization chamber. Because the CNT-based film dosimeter was placed on the carbon fiber table top without buildup, the dose calibration with the parallel plate ionization chamber was also done without buildup. The relative surface dose rate in water, $DR_{surface}$, can be calculated by

$$DR_{surface}(cGy/min) = \frac{M_{surface}}{M_{calibration}} \times \frac{1cGy}{MU} \times DoseRate\frac{MU}{min}. \quad (5.10)$$

As shown in equation 5.10, the measured dose rate with the CNT-based film dosimeter is converted to the dose rate in water using the ratio of the parallel plate ionization chamber reading for a 2×2 cm^2 field to the parallel plate ionization

chamber reading in the calibration geometry corresponding to 1 cGy/MU. The ratios of the parallel plate ionization chamber reading for different beam energies are given in Appendix 7. Fig 5.18 shows the current change per unit area of the dosimeter versus different dose rate in water.

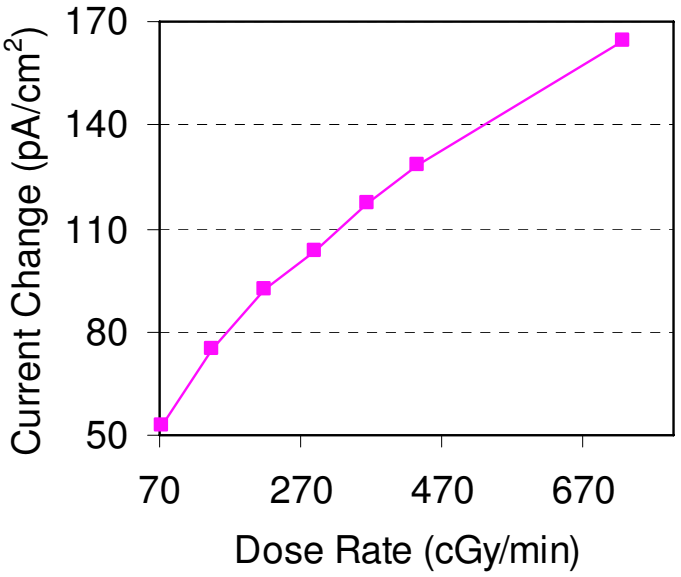

Figure 5.18: Current change per unit area of the dosimeter with 3 layers of CNTs versus 4 MeV electron beam delivered at different dose rate in water

Since both the X and Y axes of Fig 5.18 are measured rates, the collected charge can be determined per unit dose by appropriate scaling of time. The charge, Q, measured by the dosimeter per minute per unit area can be calculated by

$$Q(pC/min \cdot cm^2) = \Delta I \times \frac{60sec}{min} \times \frac{1}{area}. \tag{5.11}$$

Fig 5.19 shows the relationship between the charge measured by the dosimeter per minute per unit area and the relative surface dose in water. This is the

charge generated per unit area of detector irradiated and represents the unit area sensitivity of the CNT-based film dosimeter. This quantity is approximately linear with dose and irradiated field size, and independent of beam energy.

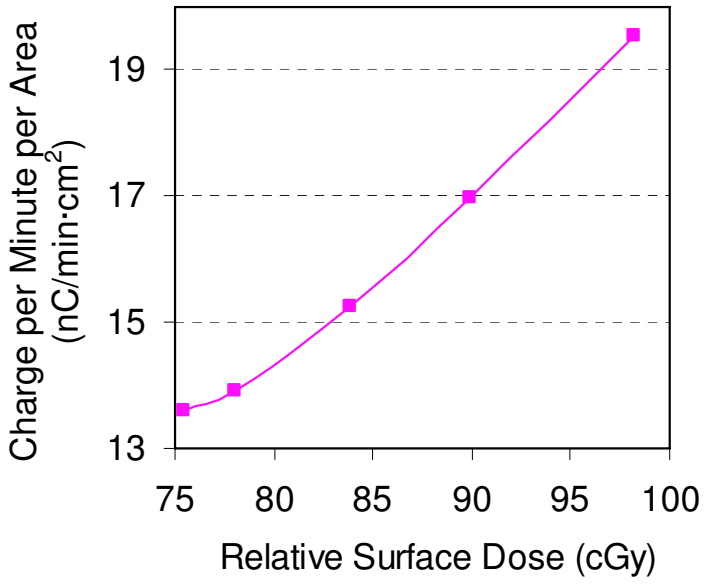

Figure 5.19: Charge measured by the dosimeter with 3 layers of CNTs per minute per unit area versus relative surface dose in water (data from 4, 6, 9, 12, and 16 MeV electron beams delivered at 400 MU/min dose rate)

5.3.5 The Concept of Flexible Dosimeter

In sections 5.3.1 and 5.3.3, the fabrication process and performances of the CNT-based film dosimeters are described. If the glass substrate in the dosimeters is replaced by a flexible substrate, the dosimeters will have the features of transparency and flexibility that allow the dosimeter to fit the contour of a surface with a curvature. In order to test this concept, a sheet of polyester was chosen as the substrate. CNT films were fabricated on the top of

the polyester sheet by following the fabrication procedure described in section 5.3.1, and then the copper electrodes were made. A photo of a flexible CNT film dosimeter being bent is shown in Fig 5.20.

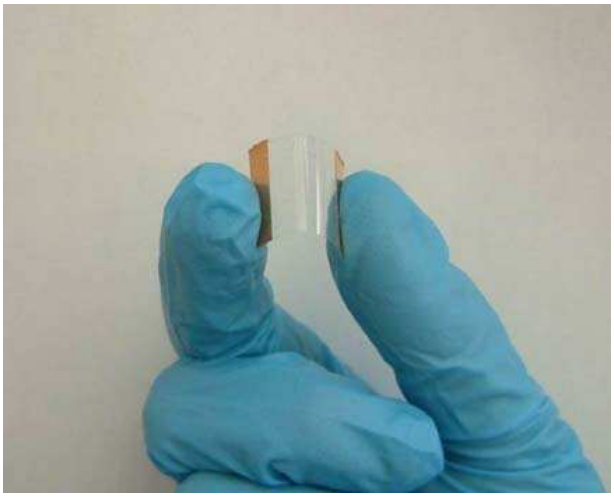

Figure 5.20: Photo of a flexible CNT-based film dosimeter being bent

To test the flexibility of the dosimeter, measurements were taken when the dosimeter was flat and bent. 4 MeV electron beams with a dose rate of 400 MU/min were used in the experiments. After the dosimeter was irradiated at the flat status, it was bent and irradiated under the same experimental conditions. The experiments were repeated three times. Fig 5.21 shows the responses of the dosimeter.

As shown in Fig 5.21, when the dosimeter is bent, the current changes are reduced slightly. But the dosimeter recovers completely to the flat status and exhibits excellent repeatability. This result indicates that the flexible dosimeter can be bent to fit the curvature of objects.

The further investigation on the response of the flexible dosimeter with different bending angles will be very useful. For example, measurements on the

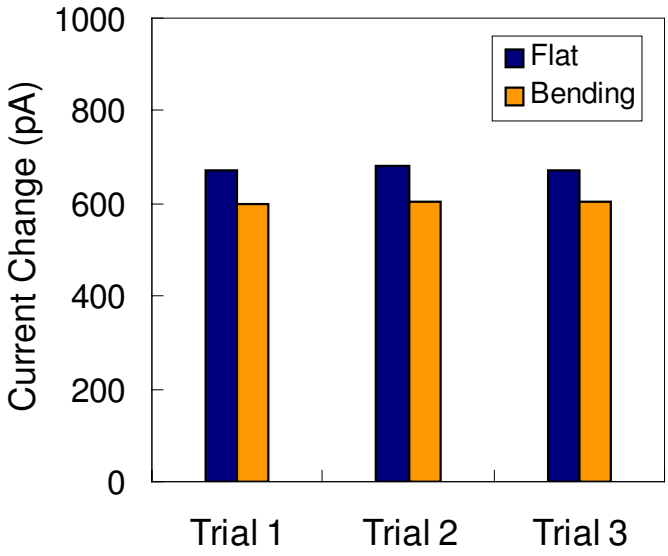

Figure 5.21: Dosimeter responses on a flat surface and curved surface

dosimeter to be bent with typical curvatures of the human body, such as the curvature of arm, neck, head, and chest, can be carried out to find the relationship between the dosimeter response and the bending angle. With further calibration, the flexible dosimeter can be worn by patients when they are undertaking radiation treatment. Real-time dosimetric information can be measured during treatment. This work will have a significant impact on the verification of prescribed dose in radiotherapy and can be conducted in the future.

5.3.6 Summary

Dosimeters based on the CNT films were designed and fabricated. The CNT films were prepared by a spin coating method. The percolative conductivity of the CNT films was studied to investigate the optimal design of the dosimeter.

The dosimeter with the 3-layer CNT film displayed the largest responses to the ionizing radiation. A CNT-based film dosimeter with a polyester substrate was built to demonstrate the possibility of a flexible and transparent dosimeter. The flexible dosimeter was able to perform dosimetric measurements when it was bent and could recover completely. The fabrication process of the CNT-based film dosimeters were completed at room temperature, and no clean room environment is required. This easy and fast fabrication process is inexpensive and allows high efficiency in the mass production of the CNT-based film dosimeter.

5.4 Carbon Nanotube-Based Film Dosimeter Array System

A CNT-based film dosimeter can provide dosimetric information at single points. In order to obtain a 2D radiation beam profile and intensity map, a dosimeter array is required. In this section, detailed information about a CNT-based film dosimeter array system, including the array design and fabrication process, readout circuit implementation, user interface, and array performance analysis, is presented.

5.4.1 Array Design and Fabrication

This section provides a necessary overview of the array structure and materials used in fabricating the proposed CNT-based film dosimeter array. A number of fabrication steps are performed to seek the preferred array structure and material for the electrode array design.

Electrode Design

Fig 5.22 represents an array electrode template designed to make the consequent electrode design standard. The template consists of 16 bonding pads and is able to provide connections for a 2 $\times$ 2 array. The size of each bonding pad is 4 $\times$ 4 mm^2 and the width of each wire is 50 μm. The size of the entire template is 35.5 $\times$ 35.5 mm^2. Up to four templates can be fabricated on one 4 inch (101.6 mm) diameter pyrex glass substrate. The blank block in the middle of the template can accommodate different electrode array designs.

Four array electrodes with different shapes and/or sizes were designed based

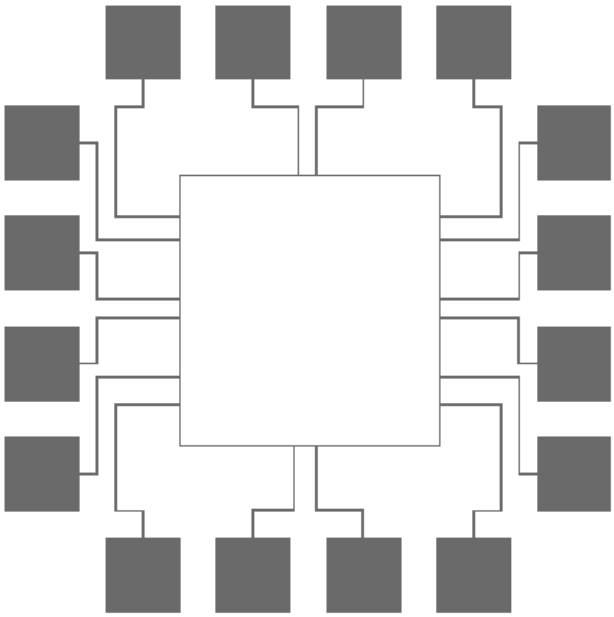

Figure 5.22: Standard electrode template for a 2 × 2 array

on the template in Fig 5.22. In the first design (design 1), the electrodes of one pixel are parallel to each other. Each electrode is 5 mm in length and 25 μm in width. The spacing between the two electrodes is 4.5 mm, which defines the sensing area of one pixel to be 5 × 5 mm^2. The spacing between two adjacent pixels is 3 mm. Design 1 is illustrated in Fig 5.23.

The second design is to study whether the width of the electrode affects the signal collection. In the second design, as shown in Fig 5.24, the electrodes are still parallel to each other with a length of 5 mm, but the width of each electrode is 1 mm. The spacing between the two electrodes is reduced to 3 mm in order to remain the sensing area of each pixel to be 5 × 5 mm^2. And the spacing between two adjacent pixels is maintained at 3 mm.

A very common comb electrode structure was used in the third design. As observed in Fig 5.25, pixel (1, 1) and (1, 2) have a sensing area of 5 × 5 mm^2 and

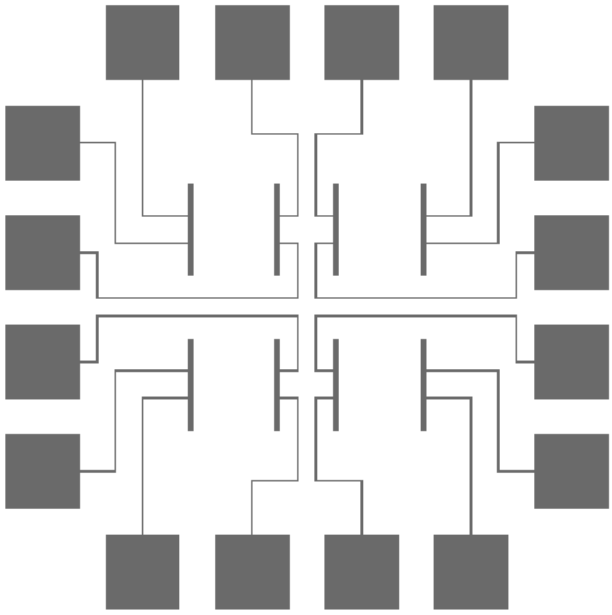

Figure 5.23: Design 1 - parallel electrodes with 25 μm in width forming a sensing area of 5 $\times$ 5 mm^2 for each pixel

a spacing of 500 μm between the two adjacent fingers. For pixel (2, 1) and (2, 2), the spacing between the adjacent fingers is still 500 μm, but the sensing area is reduced to 3 $\times$ 3 mm^2.

The fourth array electrode was designed to test whether the size of the sensing area affects the signal collection. As shown in Fig 5.26, the design of the fourth array electrode is very similar to that of design 1 except that the sensing area of each pixel is reduced to 3 $\times$ 3 mm^2.

A summary of the parameters in each design is provided in Table 5.4. The final layout of the four designs on one substrate is shown in Fig 5.27, where the eight cross marks are used to align two masks during the photolithography processes.

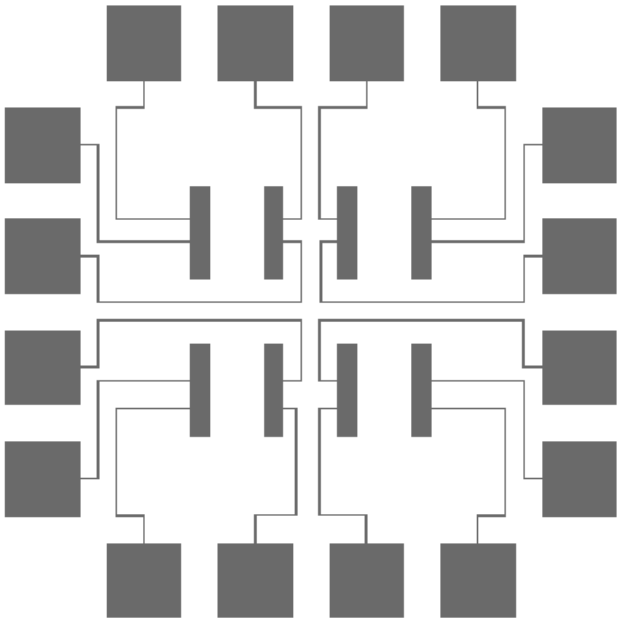

Figure 5.24: Design 2 - parallel electrodes with 1 mm in width forming a sensing area of 5 $\times$ 5 mm^2 for each pixel

Electrode Fabrication

The electrode arrays were fabricated at the Cornell NanoScale Science & Technology Facility (CNF), Cornell University, Ithaca, New York. A total of two masks is required: one for the electrode array patterning and the other for leaving windows to spin coating CNT films. Pyrex glass are used as substrates. The electrode array fabrication process is illustrated in Fig 5.28, and each step is explained as follows.

- **Substrate Cleaning**: The purpose of this step is to remove dust and native oxide from the substrate surface. The native oxide tends to form hydrogen bonds with the water molecules that are adsorbed from the air. When the photoresist is spun on such surface, the photoresist layer adheres to

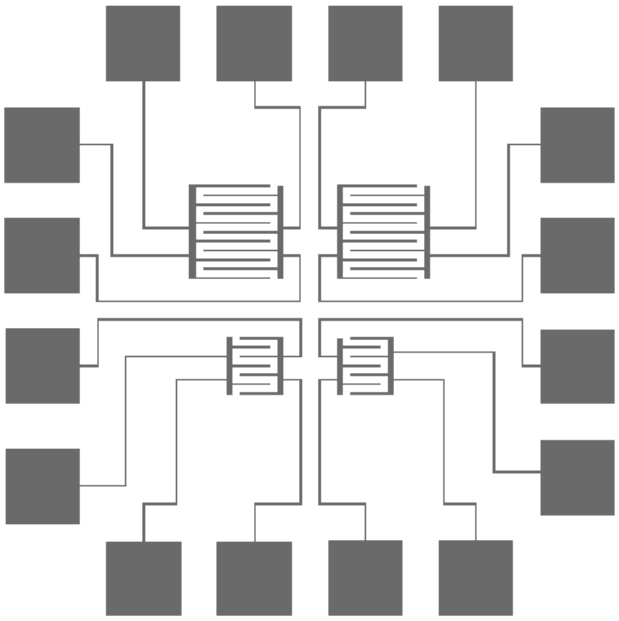

Figure 5.25: Design 3 - comb electrodes with different sensing areas

the water vapour rather than to the substrate surface. In order to avoid this situation, isopropyl or methanol rinse is used to remove the dust and native oxide from a brand new substrate. If there is grease on the substrate, methylene chloride is required to remove the grease.

- **Photolithography**: Photolithography is a process of transferring patterns of geometric shapes on a mask to a thin layer of photoresist that is spin-coated onto the surface of a wafer [124]. A layer of LOR 5A with a thickness of 500 nm was spun onto the pre-cleaned pyrex glass substrate as an adhesion promoter, followed by a soft bake at 180 ^{o}C for 4 minutes on a hot plate to drive the solvent from the resist. Consequently, a 1.4 μm positive photoresist S1813 layer was spun on the top of the LOR 5A layer, followed by a soft bake at 90 ^{o}C for 60 seconds on the hot plate. Fig 5.28 (a) shows the substrate

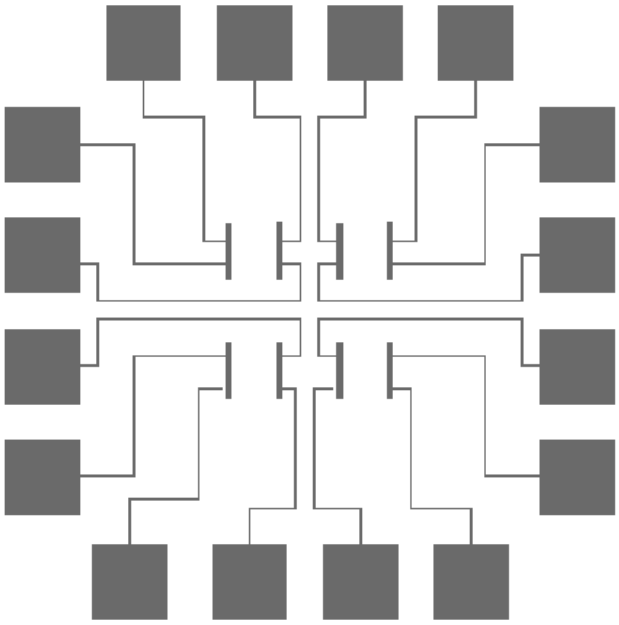

Figure 5.26: Design 4 - parallel electrodes with a 25 μm in width forming a sensing area of 3 $\times$ 3 mm^2 for each pixel

with photoresist coated on the surface.

The substrate was then exposed for 3.6 seconds by using the first mask and developed for 60 seconds. The exposed regions became soluble and could be easily removed in the development process. The exposure and development processes were achieved by an EV 620 Contact Aligner and a MIF300 developer, respectively.

Oxygen plasma in a descum process further removed the residual photoresist from the substrate before depositing the metal layer. This process was carried out by a Branson/IPC P200 Barrel Etcher. Fig 5.28 (b) is the result after the first photolithography.

- **Metal deposition**: 16 nm of chromium was deposited as an adhesion layer

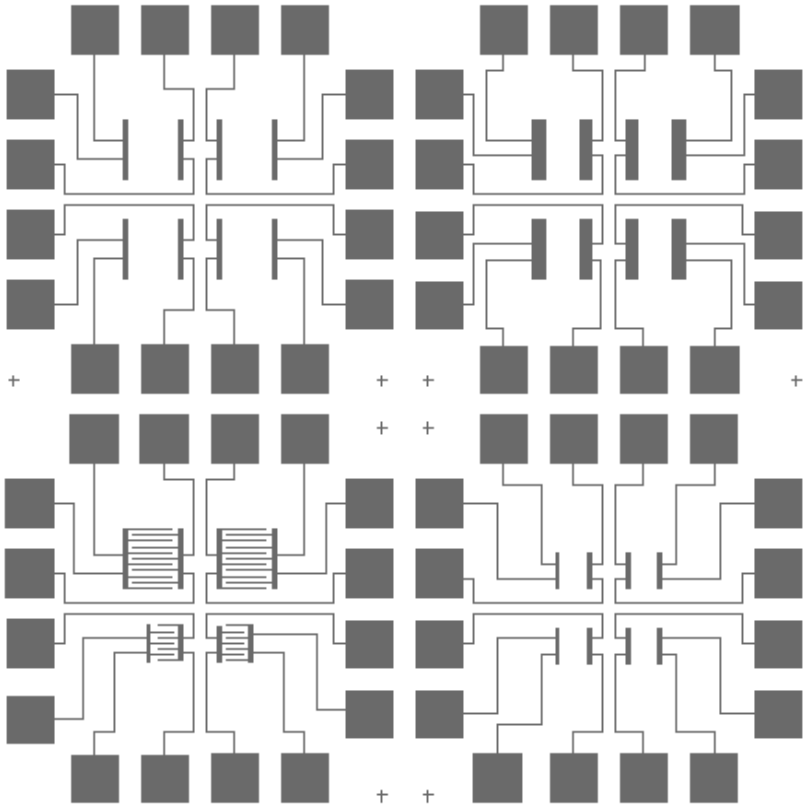

Figure 5.27: Final layout of the four designs in one substrate

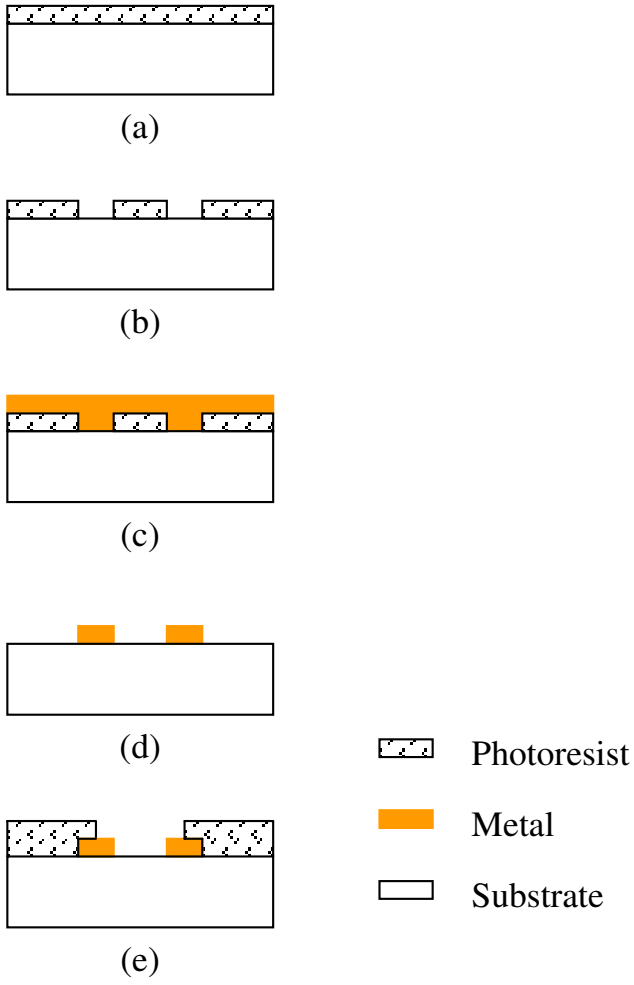

Figure 5.28: Electrode array fabrication process (a) photoresist coated on the substrate, (b) after the first photolithography, (c) metal deposition, (d) lift-off, and (e) after the second photolithography

Table 5.4: Summary of parameters in four electrode array designs

Design No.	Electrode length (mm)	Electrode width (mm)	Fingers	Sensing area (mm^2)
Design 1	5	0.25	No	5×5
Design 2	5	1	No	5×5
Design 3	5 and 3	0.25	Yes	5×5 and 3×3
Design 4	3	0.25	No	3×3

followed by 300 nm of gold by using an E-gun evaporation system for the deposition of the metal thin films (CVC 4500 Evaporator). The metal layer covered the remaining photoresist as well as parts of the substrate where the photoresist was removed in the previous developing step (Fig 5.28 (c)).

- **Lift-Off**: The substrate was then placed in 1164 soak for 24 hours or longer. The photoresist underneath the metal layer was dissolved in the solution, in the meanwhile, the metal layer that was deposited on the photoresist was removed. The metal that was deposited directly on the substrate remained after the lift-off process, as shown in Fig 5.28 (d). After the lift-off process, the substrate was rinsed in Isopropyl Alcohol (IPA) and DI water consequently, and dried by N_2 gas.

- **Substrate Cutting and Cleaning**: Before cutting the substrate into individual chips, a layer of photoresist S1818 was spun on the top of the metal layer to prevent the cutting dust from being deposited on the

electrode patterns. This was followed by a soft bake at 115 ^{o}C for 90 seconds and a hard bake at 90 ^{o}C for 2 hours. Then a K & S7100 Dicing Saw with an all-purpose standard 300 μm-width blade was used to cut the substrate. After stripping the photoresist S1818, the substrate was cleaned with IPA and DI water, and dried.

- **Windows for CNT Film Coating**: A thin layer of adhesion promoter P20 and 2.1 μm photoresist S1818 were spun on the chips, followed by a soft bake at 115 ^{o}C for 90 seconds on the hot plate. The chips were exposed for 8 seconds by an HTG System III-HR Contact Aligner using the second mask and developed in a MIF300 Developer for 60 seconds. A following descum process removed the residual photoresist from the glass substrate so that the CNT film can adhere well to the substrate. Fig 5.28 (e) illustrates the substrate with a window for CNT film coating.

Fig 5.29 shows optical photos of the electrode arrays. CNT films were then prepared on the substrate with the patterned electrodes by following the procedures described in section 5.3.1.

5.4.2 Readout Circuit

The experimental results of a single-pixel CNT-based film dosimeter were measured by using the commercial electrometer, Dose 1 Digital Electrometer. However, a readout circuit is required to measure the multiple output signals from the dosimeter array.

The amplitude of the output signals from the dosimeter array is at the picoampere level (1 pA = 10^{-12} A). In this situation, filtering of the noise to improve the signal-to-noise ratio is a big challenge to overcome. The

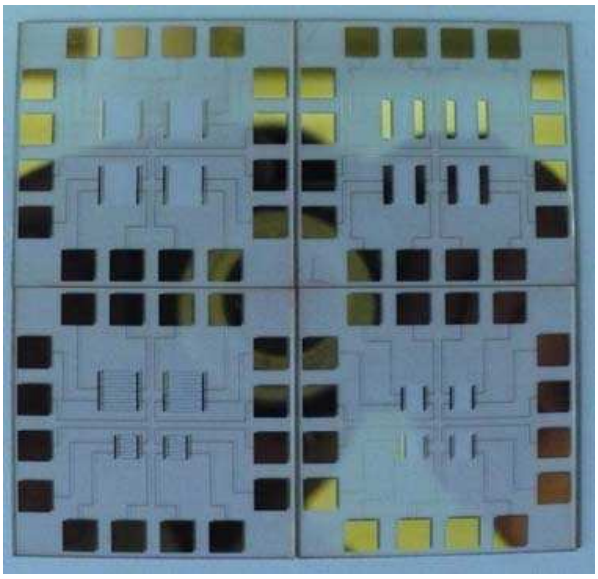

(a)

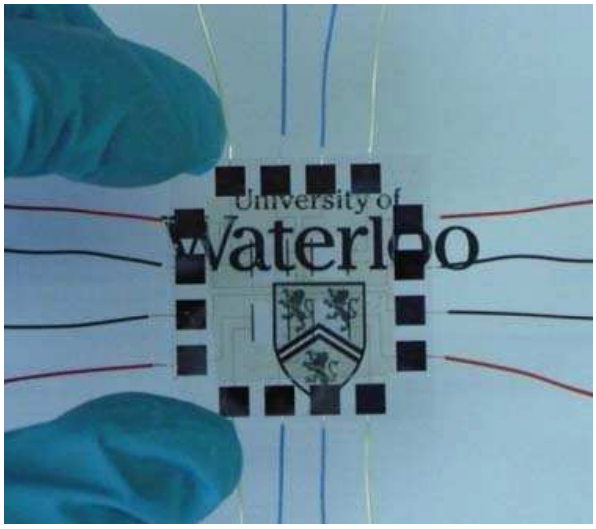

(b)

Figure 5.29: (a) Photo of four electrode arrays on pyrex glass substrates and (b) Photo shows the transparency of the array after being coated with the CNT film and wire bonding

organization of the following two sections is that the theory of operation is introduced first followed by the implementation of the design.

Theory of Operation

In order to measure the picoampere current, a negative feedback loop based on transimpedance amplifiers was chosen to convert the input current into a voltage [125, 126]. A schematic diagram of the current readout circuit for a single readout channel is illustrated in Fig 5.30.

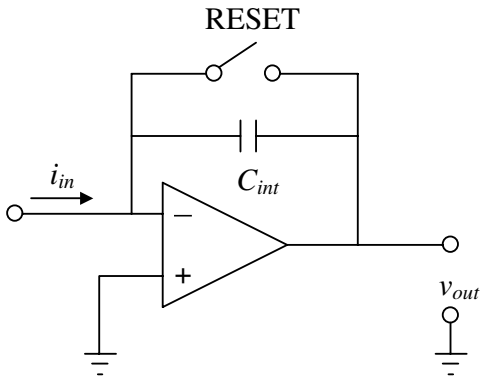

Figure 5.30: Current readout circuit for a single readout channel

In the negative feedback setup, the negative input of the amplifier is connected to one electrode of the CNT-based film dosimeter array pixel, and the positive input is connected to the ground. The amplifier's output is fed back to its negative input. When the feedback RESET switch of the amplifier is closed, the integrating capacitor C_{int} is discharged, thus resetting the amplifier. When the RESET switch is open, the current input from the dosimeter array pixel is converted into voltage. The voltage measured at the output of the amplifier v_{out} is proportional to the

charge collected and equal to the voltage across the capacitor, which is given by

$$v_{out}(t) = -\frac{1}{C_{int}} \int_0^{\tau_{int}} i_{in}(t)dt = \frac{1}{C_{int}} \int_{\tau_{int}}^0 dq_{in}(t), \tag{5.12}$$

where τ_{int} is the duration of the charge integration, i_{in} and q_{in} are the ionizing current and charge, respectively. If $i_{in}(t)$ remains constant throughout a small time interval of integration τ_{int}, the output voltage is simplified to

$$V_{out} = -\frac{I_{in}}{C_{int}} \tau_{int}. \tag{5.13}$$

If rearranging equation 5.13, the ionizing current can be determined by reading the output voltage of the amplifier and is given by

$$I_{in} = -\frac{V_{out}}{\tau_{int}} C_{int}. \tag{5.14}$$

For clarity, this negative feedback loop based transimpedance amplifier is referred as an integrator in the following sections.

Design Implementation

The implementation of the circuit is made with two assumptions in minds: (i) the pre- and post-irradiation leakage currents are negligible $< 10^{-12}$ A; (ii) the sensitivity of the circuit is independent of the ambient conditions and time. A block diagram of the CNT-based film dosimeter system elements is shown in Fig 5.31. The arrows indicate the direction of the signal path.

As observed in Fig 5.31, the output voltages from the integrators are sent to a buffer and then collected and converted into binary numbers via an analog-to-digital (A/D) converter. These binary numbers are sent to a microcontroller for processing and subsequently transmitted to a host computer via a recommended standard 232 (RS232) cable. Besides processing the digital

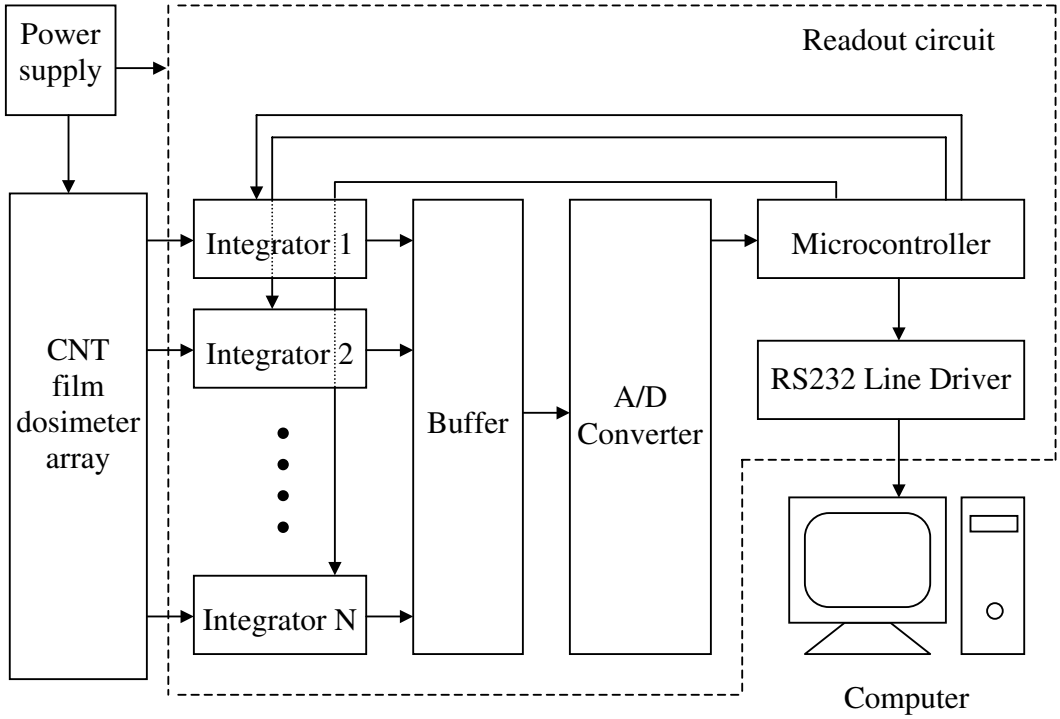

Figure 5.31: Block diagram of the CNT-based film dosimeter system elements

signals, the microcontroller also controls the RESET switches of the integrators. A RS232 line drive is needed to convert the output voltage levels of the microcontroller to the proper RS232 voltage levels. Details of the selected components are listed as follows.

- **Integrator**: Specialized integrator chips with built-in capacitors, ACF2101, from Burr-Brown [127] are used in the circuit. The leakage currents of the ACF2101 integrator are low (at femtoamper range 1 fA = 10^{-15} A). The integrator chip also has built-in HOLD and RESET switches.

- **Buffer**: An operational amplifier, OPA241, from Burr-Brown [128] is

employed as a buffer. The OPA241 chip has an input impedance of 10 MΩ, which can isolate the integrator circuitry from the interference from the voltage measuring circuitry. The output current of the amplifier is in the range of -24 mA to +4 mA, which allows enough current for the A/D converter.

- **Analog to Digital Converter**: An A/D converter integrated circuit chip, ADS8509, from Burr-Brown [129] offers a 16-bit resolution analog-to-digital signal convert.

- **Microcontroller**: A microcontroller, ATmega8, from Atmel [130] is used to control all the components in the circuit. The microcontroller has a universal asynchronous receiver/transmitter (UART) for RS232 communications with the host computer, a serial peripheral interface (SPI) for communications with the A/D converter, an internal clock for timing, and enough pins to control the multiplexing of the integrator outputs and the integrator HOLD and RESET switches.

- **RS232 Line Driver**: A RS232 Driver/Receiver, MAX232A, from Maxim [131] is used to convert the transistor transistor Logic (TTL) voltage levels required by the microcontroller to the different voltage levels needed by the RS232 interfaces.

- **Other Components**: Besides the previous principal components, a voltage regulator, μA7805, from Texas Instruments [132] and a charge pump voltage converter, TC7662A, from Microchip [133] are used to provide the required power to all the components. A MC14028B from ON Semiconductor [134] and a CD4069UB from Texas Instruments [135] work together to control the

channel selection.

The circuit is powered by a +15 V voltage, which is provided by an external power supply. The inputs of the circuit are connected to the corresponding electrodes of each pixel in the CNT-based film dosimeter array. The background noise of the circuit is about 20 pA. The typical signal measured by the dosimeter array is of the order of several hundred picoampere. Therefore the signal to noise ratio of the dosimeter array system is greater or equal to 10:1. With the dosimeter array, readout circuit, external power supply, and computer, the dosimeter system is capable of providing real-time dosimetric measurements.

5.4.3 User Interface

Software was developed using LabVIEW to provide a graphical user interface. The function of the software includes reading the data from the serial communication port, displaying the data on the screen in real-time, and saving the data into individual excel files for each trial of measurements so that the data can be analyzed after the experiments. Fig 5.32 is a screenshot of the software display screen during an experiment.

The readings from two channels can be seen simultaneously in one screenshot. The information from the other channels is available by rolling the navigation bar on the right-hand side of the screen. For example, in Fig 5.32, the windows on the left-hand side display the voltage values read from the circuit. The windows on the right-hand side display the corresponding current values that were calculated according to equation 5.14. The two pairs of windows in the bottom convey the data read from channel 0 (Ch0) and channel 1 (Ch1), respectively. The upper two windows provide the data read from all the channels.

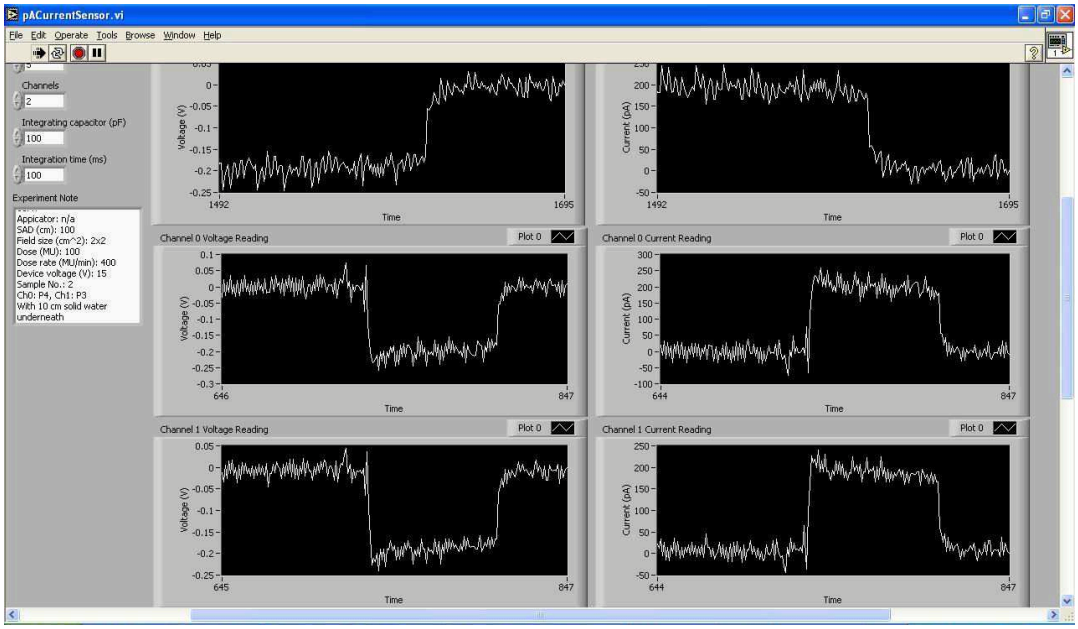

Figure 5.32: Screenshot of the software display

This user interface acquires data from the readout circuit and presents the data in the format of graphs. The graphs provide an instant data display, which allows technical or treatment staff to easily interpret the data and make decisions timely. Moreover, the graphs provide useful information on how long the beam is ON. Fig 5.33 (a) to (f) show the screenshots of the 6 MeV electron beams delivering 100 MU dose at dose rates of 100, 200, 300, 400, 500, and 600 UM/min, respectively, given that the other experimental conditions remain the same. It is clearly shown in Fig 5.33 that the beam ON duration decreases when the higher dose rates are chosen to deliver the same amount of dose.

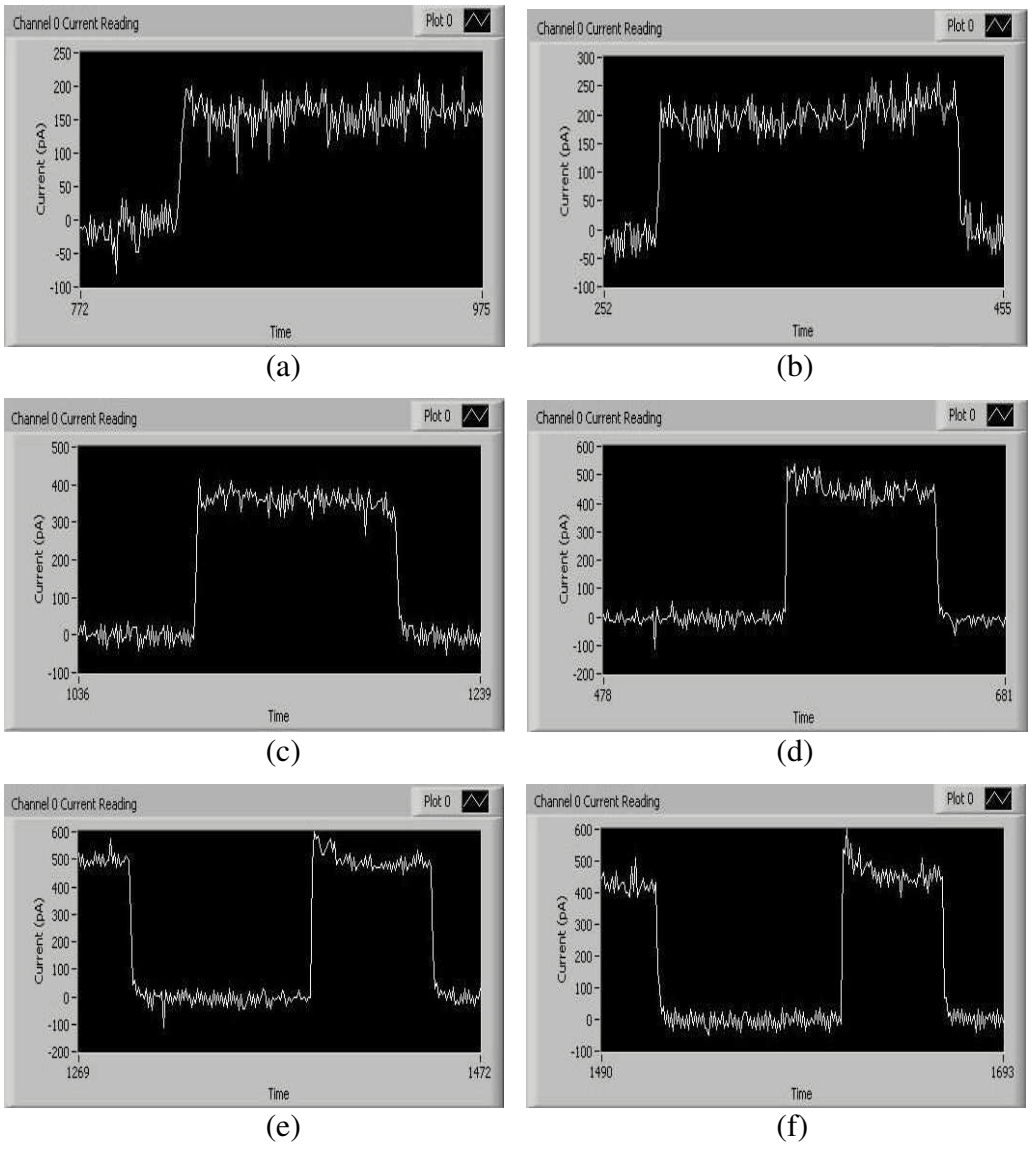

Figure 5.33: Beam ON duration when the dose rates are (a) 100 MU/min, (b) 200 MU/min, (c) 300 MU/min, (d) 400 MU/min, (e) 500 MU/min, and (f) 600 MU/min. (Note: The beam OFF time is not shown in (a) because the delivery time of the beams with a 100 MU/min dose rate is longer than the range that can be shown in the display window)

5.4.4 Experimental Results

Performance of Arrays with Different Electrode Designs

First, the performance of the dosimeter arrays with various electrode designs is compared. The specific parameters of each design can be found in section 5.4.1. All the measurements were performed with 9 MeV electron beams with dose of 100 MUs at a dose rate of 200 MU/min and field size of 2×2 cm^2. The readings from Ch0 of the electrode array design 1, 2, and 4 are taken to make comparison since the pixels in one array are identical. Because the electrode array design 3 contains two different comb electrode structures, the readings from Ch0 and Ch2 are used in the comparison. The readings are shown in Fig 5.34, where the average current changes were marked with the dash lines.

The size of each sensing area is the same in design 1, 2, and for pixel (1, 1) and (1, 2) in design 3. The difference is the contact area of the CNT films with the electrodes. Both design 2 (the parallel electrode structure with an increased electrode width) and design 3 (the comb electrode structure) have increased contact areas between the CNT films and the electrodes compared with design 1. The average readings shown in Fig 5.34 (a), (b), and (c) are very close to each other. The effect of the increased contact areas on the array performance is negligible. This result indicates that the responses of the dosimeter arrays are independent of the contact area between the CNT films and the electrodes. The performance of the comb electrode structure with a 3×3 cm^2 sensing area in design 3, Fig 5.34 (d), and the parallel electrode structure in design 4, Fig 5.34 (e), also verify this conclusion.

Fig 5.34 (a) and (e) show the readings from design 1 and 4. The difference between design 1 and 4 is the size of the sensing area. Design 4 has a sensing area

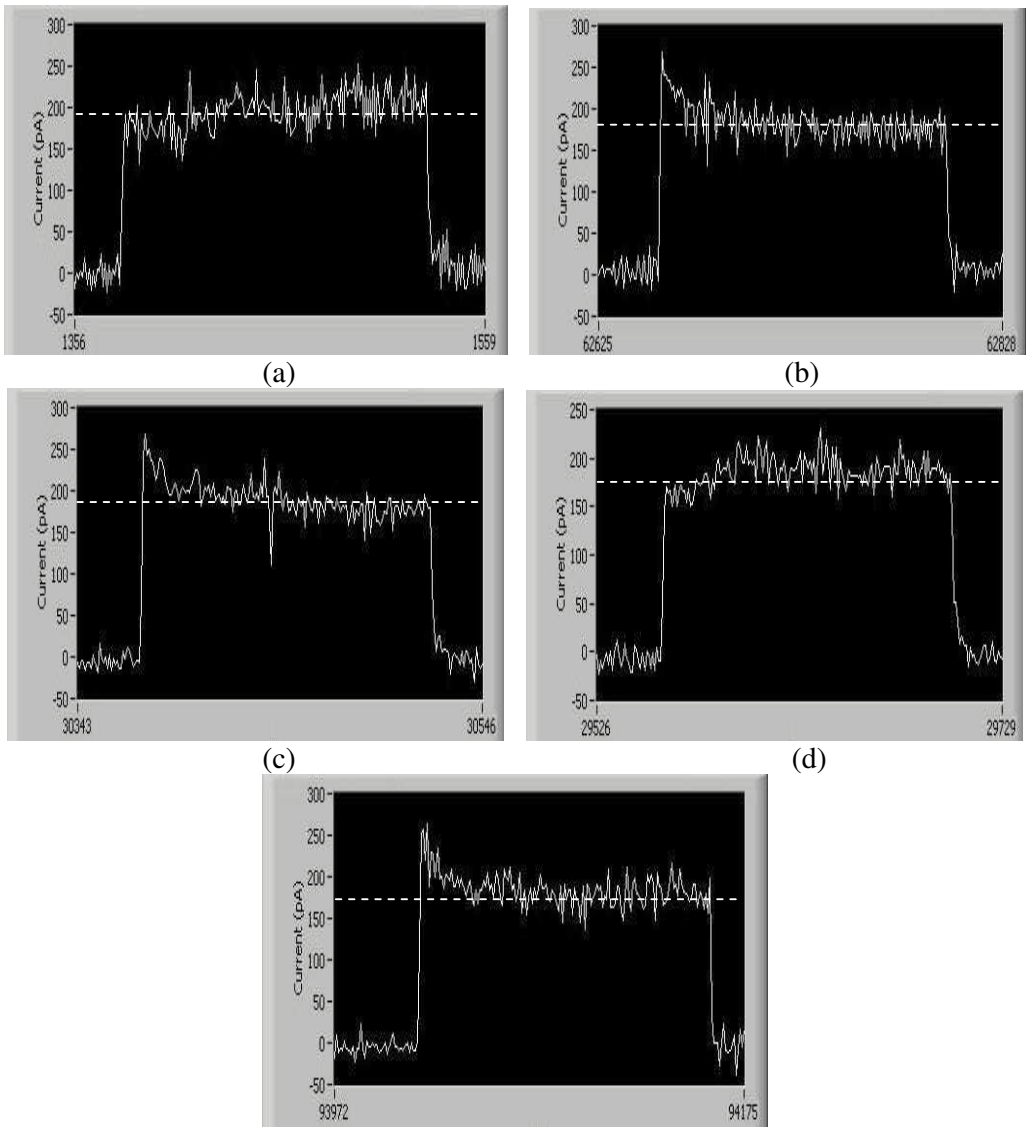

Figure 5.34: Readings from (a) Ch0 in design 1, (b) Ch0 in design 2, (c) Ch0 in design 3, (d) Ch2 in design 3, and (e) Ch0 in design 4

of 3 × 3 cm^2 for each pixel, which is 64% smaller than that of the pixels in design 1 (5 × 5 cm^2). However, as shown in Fig 5.34 (a) and (e), the response of design 4 is only a little less than that of design 1, which does not decrease proportionally to the reduced sensing area. This results provide valuable information for designing high-resolution arrays. An array with a smaller sensing area of the individual pixels can provide higher resolution 2D beam profile maps. The high-resolution arrays are especially useful when dose information is required at points, where the high dose gradient occurs, for example, at the edges of a beam.

After an overall evaluation of the performances of the four designs, it is concluded that design 4 (the parallel electrode structure with a 3 × 3 cm^2 sensing area for each pixel) provides good signal responses with a reduced sensing area. More details on four electrode array designs are shown in Table 5.4. It is noteworthy that the gold electrodes of the array may give an enhanced signal due to the high atomic number of gold ($Z_{gold} = 79$). Further study on the energy dependence of the gold electrodes is needed in the future.

Repeatability Measurements

The repeatability measurements were carried out for both photon and electron beams. Taking design 1 as an example, Fig 5.35 shows the repeatability measurements between the beam ON and OFF for (a) the 15 MV photon beams and (b) the 6 MeV electron beams.

As illustrated in Fig 5.35 (a) and (b), the dosimeter array responded instantly to the radiation beam ON and OFF. The response time of the array was less than 300 milliseconds for both the photon and electron beams. In addition, the array demonstrated good repeatability. Similar repeatability for the photon and electron beams at the other energy levels were observed.

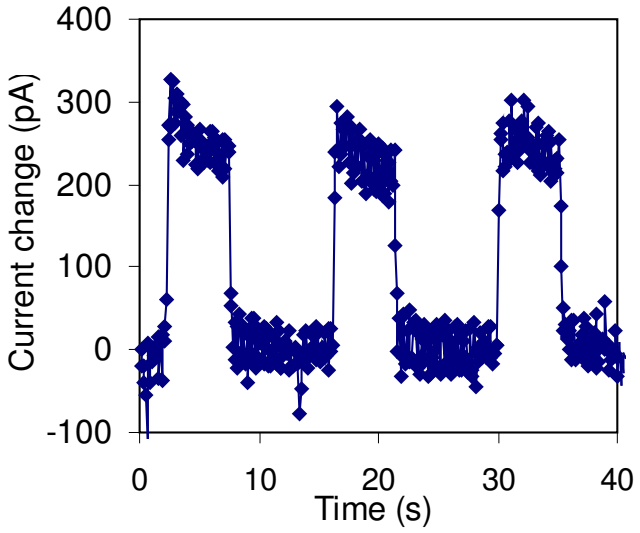

(a)

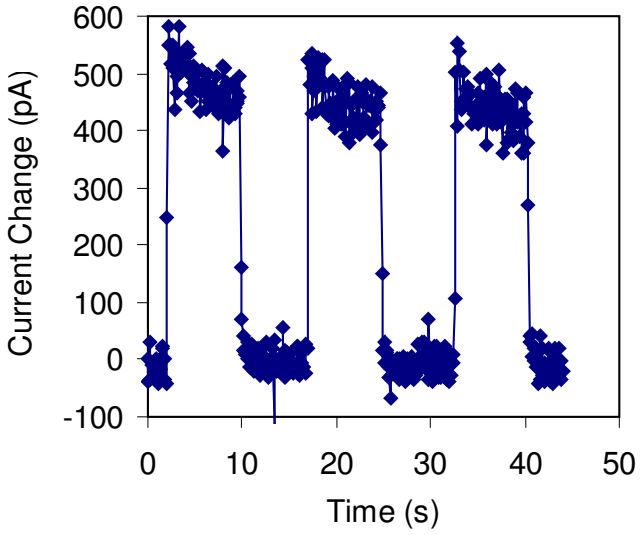

(b)

Figure 5.35: Repeatability measurements between beam ON and OFF for (a) 15 MV photon beams and (b) 6 MeV electron beams

5.4.5 Summary

In this section, a CNT-based film dosimeter array system is described. The system consists of a CNT-based film dosimeter array (to measure the ionizing radiation), a readout circuit (to detect the signals from the dosimeter array and send them to the host computer), and user interface software (to acquire the data from the readout circuit and provide a user interface). The information on the array design and fabrication process, circuit implementation, and software function are provided in detail. The CNT-based film dosimeter arrays performed well with excellent repeatability. A comparison of the CNT-based film dosimeters with current dosimetric measurement techniques is given in Table 5.5.

5.5 Conclusion

For the first time, dosimeters using carbon fibres and CNT films as sensing materials were built to measure ionizing radiation in radiotherapy. First, a carbon fibre sheet-based dosimeter with a sensing area of 1.8×1.8 cm^2 was designed. The dosimeter can provide real-time information on dose rate and dose measurements. Changes in the current passing through the carbon fibre sheet indicate the dose rate changes. The charge changes reflect the dose differences.

Secondly, dosimeters based on CNT-films were fabricated. A spin coating method was developed to form CNT films on glass and polyester substrates. Films with different densities of CNTs were prepared to investigate the optimal design of the dosimeter. The dosimeter with a 3-layer CNT film displayed the largest responses to the ionizing radiation. A transparent and flexible dosimeter based on CNT films was also demonstrated. This flexible dosimeter was able to provide dosimetric measurements when it was bent to fit the curvature of a surface.

Table 5.5: Comparison of the CNT-based film dosimeters with current dosimetric measurement techniques

	Ionization chambers	TLDs	Radiochromic films	MOSFET dosimeters	CNT film dosimeters
In vivo measurement	No	Yes	Yes	Yes	Yes
Usability for volume dosimetry	1D	1D/2D	2D	1D	1D/2D
Real-time readout	Yes	No	No	Yes	Yes
Accumulated dose dependent	No	No	No	Yes	No
Provide dose rate information	No	No	No	Yes	Yes

Thirdly, a CNT-based film dosimeter array system was developed including a CNT-based film dosimeter array, a readout circuit, and user interface software. Four designs of electrode array were compared. The implementation of the readout circuit and software was presented. The array with the parallel electrode structure and a 3×3 mm^2 sensing area for each pixel provided good signal responses. The array system showed excellent repeatability in the measurements.

Chapter 6

Contributions and Future Work

This thesis explores a new generation of dosimeters using CNTs and carbon fibres to provide real-time monitoring of radiation delivery in radiotherapy. The main contributions of the thesis and suggestions for future research are summarized in the next two sections.

6.1 Summary of Contributions

Novel dosimeters and dosimeter arrays are proposed to investigate the use of CNTs and carbon fibres as sensing materials for dosimetric measurements. The main contributions of this thesis are listed as follows.

- In this thesis, CNTs and carbon fibres are explored for the applications on dosimetric measurements. Several novel dosimeter designs, including a parallel plate ionization chamber with CNT electrodes, a carbon fibre sheet-based dosimeter, and a CNT-based film dosimeter are proposed in order to use the different properties of carbon materials to explore their potential in radiation dosimetry.

- For the first time, dosimeters based on carbon fibres and CNT films were built for ionizing radiation measurements in radiotherapy.

- For the first time, a transparent and flexible dosimeter was designed and fabricated. The flexible dosimeter can provide dosimetric information when it was used in the measurements of a surface with curvature.

- A functioning dosimetry system, including a dosimeter array, readout circuitry, and user interface software was designed and implemented. The miniaturized CNT-based film dosimeter can be used as a point detector to measure the dose at a certain point. The CNT-based film dosimeter array is demonstrated to be able to measure the dose distribution on a plane so that the 2D beam profile monitoring can be achieved in real-time.

- The proposed dosimeters have a high sensitivity for dose rate measurements. The repeatability and reproducibility of the dosimeters are good.

- A novel fabrication process was developed for the CNT-based film dosimeters. The process can be conducted at room temperature, and no cleanroom is required. This method provides a low cost, high efficiency, and mass production technology for the CNT-based film dosimeter manufacturing.

- The work in this thesis confirms that the dosimeters based on carbon fibres and CNT films have the potential to provide new opportunities for developing miniaturized and highly sensitive radiation dosimeters.

6.2 Future Work

Avenues for future work include the following.

- Using purified and vertically aligned CNTs as electrodes in the parallel plate ionization chamber to improve the collection efficiency of the dosimeter.
- Although preliminary experiments of the flexible CNT-based film dosimeter were performed in this study, further investigation on the characterization of the flexible dosimeters is required.
- Research on designing dosimeter arrays with more pixels can be continued so that higher resolution 2D radiation dose profile can be obtained.
- Comprehensive quality assurance testing need to be conducted to test the dosimeters and dosimeter arrays.
- Further investigation on toxicity and long-term aging of the dosimeters need to be carried out.

Appendix A

Calibration Data

The calibration data of the Varian Clinac 21 EX medical linear accelerator installed at the Grand River Regional Cancer Centre are provided as follows.

1. **6 MV Photon Beam - Percentage Depth Dose**

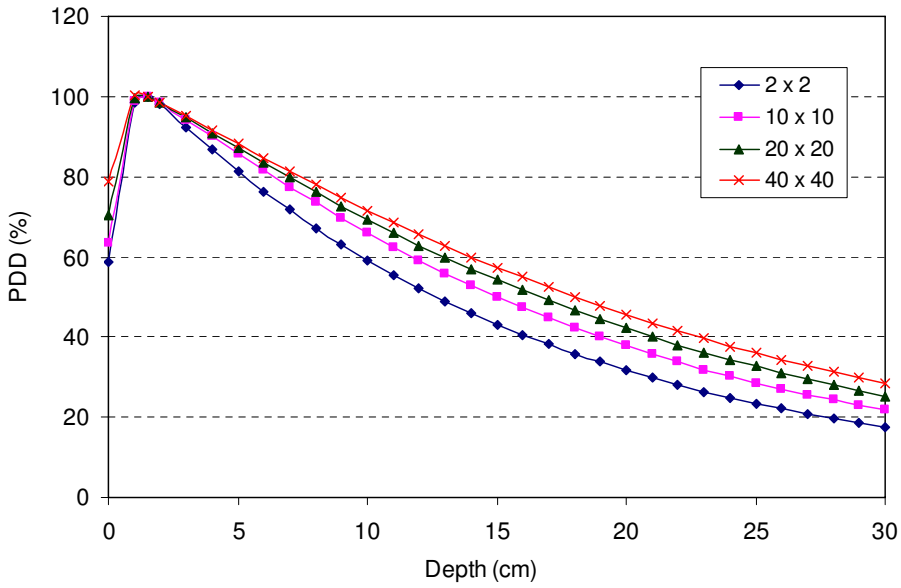

Figure A.1: 6 MV photon beam percentage depth dose for various field sizes

2. **15 MV Photon Beam - Percentage Depth Dose**

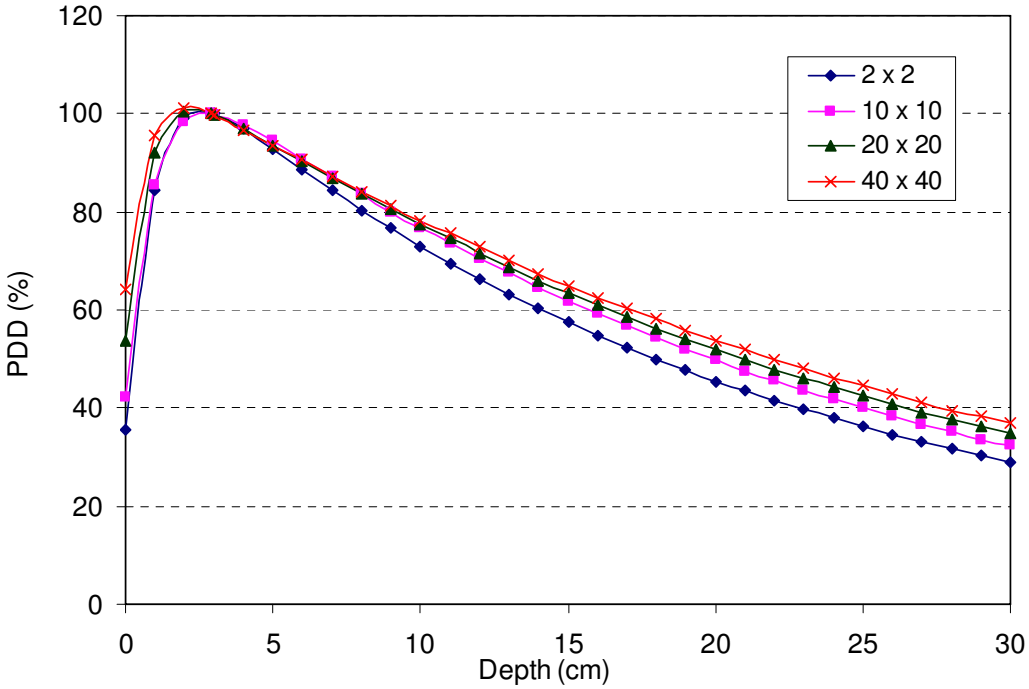

Figure A.2: 15 MV photon beam percentage depth dose for various field sizes

3. **6 and 15 MV Photon Beam - Collimator Scatter Factor**

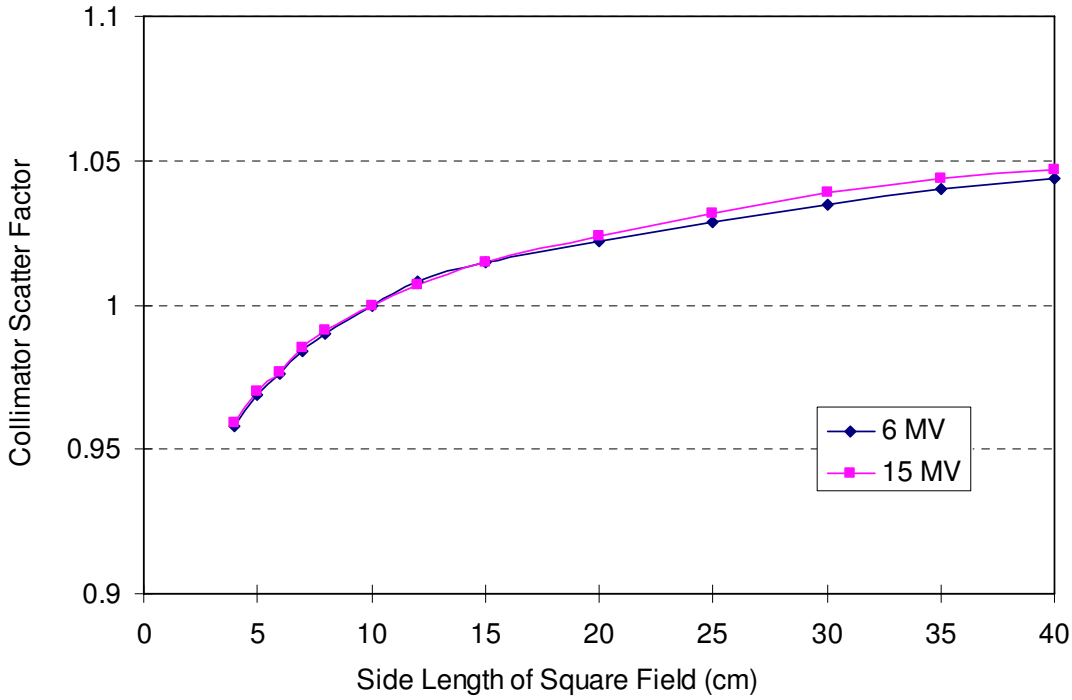

Figure A.3: Collimator scatter factor of 6 and 15 MV photon beams

4. **6 and 15 MV Photon Beam - Relative Surface Dose**

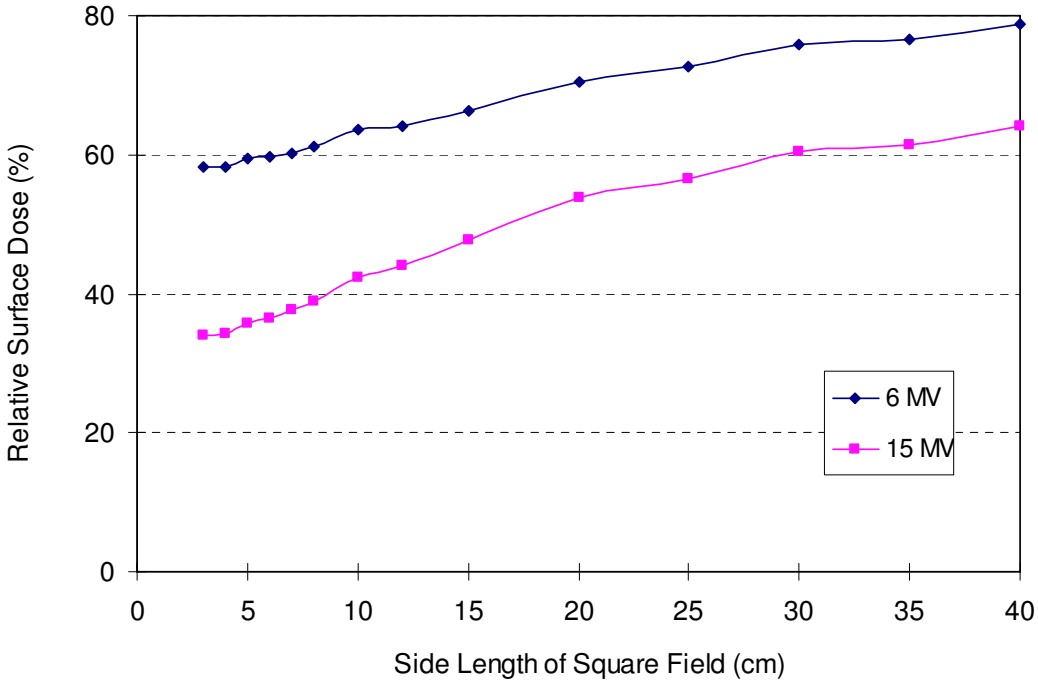

Figure A.4: Relative surface dose of 6 and 15 MV photon beams

5. **Electron Beam - Percentage Depth Dose with 10 × 10 cm^2 Field Size**

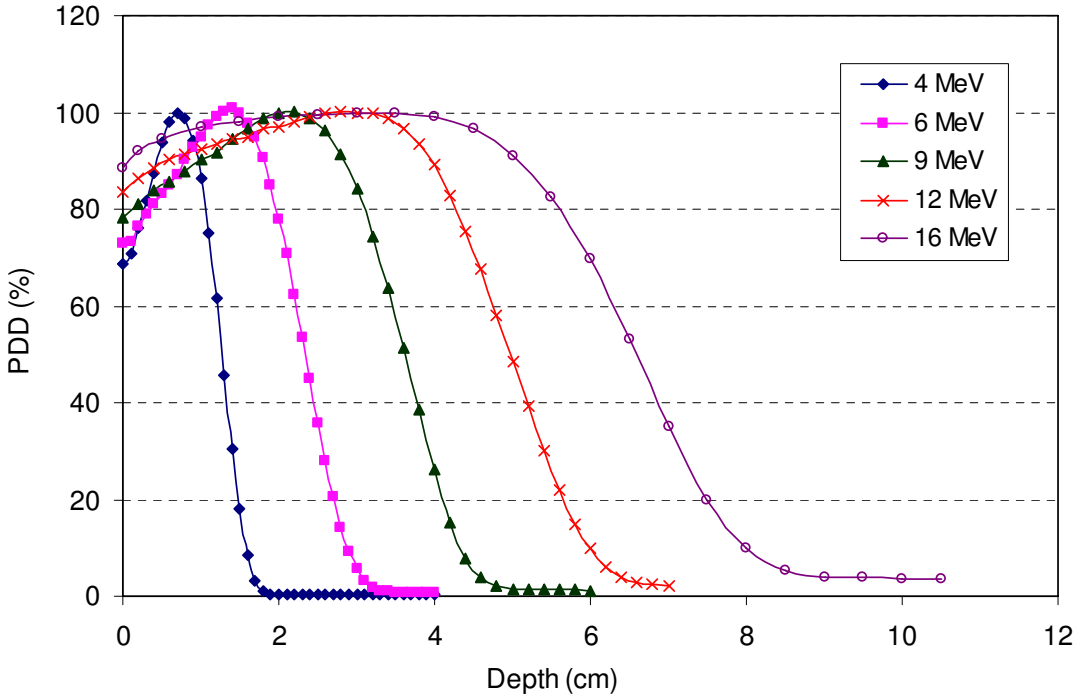

Figure A.5: Percentage depth dose of 4, 6, 9, 12, and 16 MeV electron beams with 10 × 10 cm^2 field size

6. **Electron Beam - Percentage Depth Dose with 2 × 2 cm^2 Field Size**

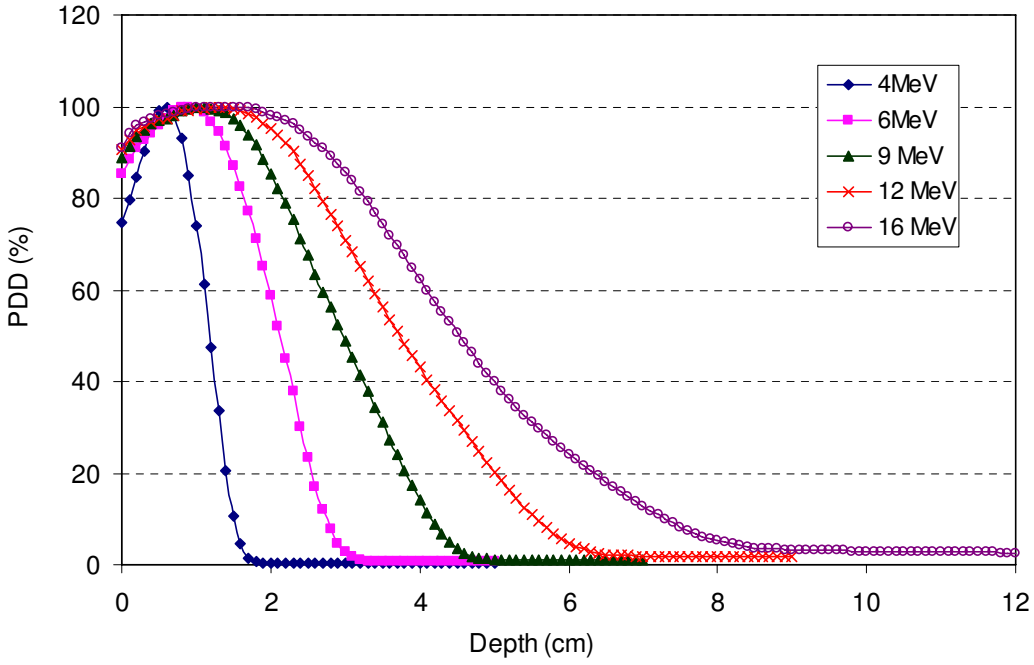

Figure A.6: Percentage depth dose of 4, 6, 9, 12, and 16 MeV electron beams with 2 × 2 cm^2 field size

7. **Ratio of Relative Surface Dose to the Dose at Calibration Geometry of Different Beam Energies**

Beam Energy	$M_{calibration}$	$M_{surface}$	Ratio
4 MeV	7.25	5.47	0.75448
6 MeV	8.53	6.66	0.78077
9 MeV	8.64	7.245	0.83854
12 MeV	8.85	7.955	0.89887
16 MeV	8.95	8.79	0.98212
15 MV	8.28	1.60	0.19323

Note:

(a) The measurements were performed by using a PTW Markus parallel plate ionization chamber.

(b) $M_{calibration}$ were measured in the calibration geometry corresponding to 1 cGy/MU.

(c) $M_{surface}$ were measured on the carbon table top without buildup at field size = 2×2 cm^2.

(d) Ratio = $M_{surface}/M_{calibration}$

Bibliography

[1] J. Van Dyk, *The Modern Technology of Radiation Oncology*, 1999.

[2] E. Podgorsak, *Review of Radiation Oncology Physics: A Handbook for Teachers and Students*. Vienna, Austria: 2005, International Atomic Energy Agency.

[3] J. F. Williamson, "Review: Brachytherapy technology and physics practice since 1950: a half-century of progress," *Physics in Medicine and Biology*, vol. 51, no. 13, pp. R303–R325, 2006.

[4] W. A. Volkert and T. J. Hoffman, "Therapeutic radiopharmaceuticals," *Chemical Reviews*, vol. 99, no. 9, pp. 2269–2292, 1999.

[5] M. S. Huq and P. Andreo, "Advances in the determination of absorbed dose to water in clinical high-energy photon and electron beams using ionization chambers," *Physics in Medicine and Biology*, vol. 49, no. 4, pp. R49–R104, 2004.

[6] C. Yu and G. Luxton, "TLD dose measurement: A simplified accurate technique for the dose range from 0.5 cGy to 1000 cGy," *Medical Physics*, vol. 26, no. 6, pp. 1010–1016, 1999.

[7] M. J. Butson, T. Cheung, P. K. N. Yu, and M. Currie, "Surface dose extrapolation measurements with radiographic film," *Physics in Medicine and Biology*, vol. 49, no. 13, pp. N197–N201, 2004.

[8] M. J. Butson, P. K. N. Yu, T. Cheung, and P. Metcalfe, "Radiochromic film for medical radiation dosimetry," *Materials Science and Engineering*, vol. R41, pp. 61–120, 2003.

[9] P. H. Halvorsen, "Dosimetric evaluation of a new design MOSFET *in vivo* dosimeter," *Medical Physics*, vol. 32, no. 1, pp. 110–117, 2005.

[10] N. Jornet, P. Carrasco, D. Jurado, A. Ruiz, T. Eudaldo, and M. Ribas, "Comparison study of MOSFET detectors and diodes for entrance *in vivo* dosimetry in 18 MV x-ray beams," *Medical Physics*, vol. 31, no. 9, pp. 2534–2542, 2004.

[11] T. Kron, A. Rosenfeld, M. Lerch, and S. Bazley, "Measurements in radiotherapy beams using on-line MOSFET detectors," *Radiation Protection Dosimetry*, vol. 101, no. 1-4, pp. 445–448, 2002.

[12] N. Wen, H. Guan, R. Hammound, D. Pradhan, T. Nurushev, S. Li, and B. Movsas, "Dose delivered from Varian's CBCT to patients receiving IMRT for prostate cancer," *Physics in Medicine and Biology*, vol. 52, no. 8, pp. 2267–2276, 2007.

[13] T. Cheung, M. J. Butson, and P. K. N. Yu, "Multilayer Gafchromic film detectors for breast skin dose determination *in vivo*," *Physics in Medicine and Biology*, vol. 47, no. 2, pp. N31–N37, 2002.

[14] C. F. Chuang, L. J. Verhey, and P. Xia, "Investigation of the use of MOSFET for clinical IMRT dosimetric verification," *Medical Physics*, vol. 29, no. 6, pp. 1109–1115, 2002.

[15] C. Ehringfeld, S. Schmid, K. Poljanc, C. Kirisits, H. Aiginger, and D. Georg, "Application of commercial MOSFET detectors for *in vivo* dosimetry in the therapeutic x-ray range from 80 kV to 250 kV," *Physics in Medicine and Biology*, vol. 50, no. 2, pp. 289–303, 2005.

[16] A. Ahnesjo and M. M. Aspradakis, "Dose calculations for external photon beams in radiotherapy," *Physics in Medicine and Biology*, vol. 44, no. 11, pp. R99 – R155, 1999.

[17] D. Djajaputra and S. Li, "Real-time 3-D surface-image-guided beam setup in radiotherapy of breast cancer," *Medical Physics*, vol. 32, pp. 65–75, 2005.

[18] S. L. Meeks, W. A. Tome, T. R. Willoughby, P. A.Kupelian, T. H. Wagner, J. M. Buatti, and F. J. Bova, "Optically guided patient positioning techniques," *Seminars in Radiation Oncology*, vol. 15, no. 3, pp. 192–201, 2005.

[19] Y. Yan, Y. song, and A. L. Boyer, "An investigation of a video-based patient repositioning technique," *International Journal of Radiation Oncology, Biology, Physics*, vol. 54, no. 2, pp. 606–614, 2002.

[20] L. Johnson, B. Milliken, S. Hadley, C. Pelizzari, D. Haraf, and G. Chen, "Initial clinical experience with a video-based patient positioning system," *International Journal of Radiation Oncology, Biology, Physics*, vol. 45, no. 1, pp. 205–213, 1999.

[21] M. J. Butson, T. Cheung, P. K. N. Yu, D. Abbati, and G. Greenoak, "Ultraviolet radiation dosimetry with radiochromic film," *Physics in Medicine and Biology*, vol. 45, no. 7, pp. 1863–1868, 2000.

[22] H. E. Johns and J. R. Cunningham, *The Physics of Radiology, 4th ed.* Springfield, Illinois: Charles C Thomas publisher, 1983.

[23] P. Metcalfe, T. Kron, and P. Hoban, *The Physics of Radiotherapy X-Rays form Linear Accelerators.* Madison, Wisconsin: Medical Physics Publishing, 1997.

[24] C. M. Washington and D. Leaver, *Principles and Practice of Radiation Therapy, 2nd ed.* St. Louis, Missouri: Mosby, 2004.

[25] F. M. Khan, *The Physics of Radiation Therapy, 2nd ed.* Baltimore, Maryland: Williams & Wilkins, 1994.

[26] D. Greene and P. C. Williams, *Linear Accelerators for Radiation Therapy, 2nd ed.* New York, New York: Taylor & Francis Group, 1997.

[27] W. Kwa, V. Tsang, R. N. Fairey, S. M. Jackson, E. El-Khatib, R. W. Harrison, and S. Kristensen, "Clinical use of asymmetric collimators," *International Journal of Radiation Oncology, Biology, Physics*, vol. 37, no. 3, pp. 705–710, 1997.

[28] F. Araki, R. Ikeda, N. Moribe, Y. Shirakawa, M. Hatemura, T. Shimonobou, Y. Hirata, T. Takada, M. Takahashi, and M. Matoba, "Dose calculation for asymmetric photon fields with independent jaws and multileaf collimators," *Medical Physics*, vol. 27, no. 2, pp. 340–345, 2000.

[29] Elekta, 2008, http://www.products.elekta.com/.

[30] D. O. Odero, G. R. Gluckman, K. Welsh, R. A. Wlodarczyk, and L. E. Reinstein, "The use of an inexpensive red acetate filter to improve the sensitivity of GAFChromic dosimetry," *Medical Physics*, vol. 28, no. 7, pp. 1446–1448, 2001.

[31] N. V. Klassen, L. van der Zwan, and J. Cygler, "GafChromic MD-55: Investigated as a precision dosimeter," *Medical Physics*, vol. 24, no. 12, pp. 1924–1934, 1997.

[32] A. Holmes-Siedle and L. Adams, "RADFET - a review of the use of metal-oxide-silicon devices as integrating dosimeters," *Radiation Physics and Chemistry*, vol. 28, no. 2, pp. 235–244, 1986.

[33] M. Soubra, J. Cygler, and G. Mackay, "Evaluation of dual bias dual metal oxide-silicon semiconductor field effect transistor detector as radiation dosimeter," *Medical Physics*, vol. 21, no. 4, pp. 457–572, 1994.

[34] S. Iijima, "Helical microtubules of graphitic carbon," *Nature*, vol. 354, pp. 56–58, 1991.

[35] N. R. Franklin and H. Dai, "An enhanced CVD approach to extensive nanotube networks with directionality," *Advanced Materials*, vol. 12, no. 12, pp. 890–894, 2000.

[36] M. S. Dresselhaus, "Fullerenes: Down the straight and narrow," *Nature*, vol. 358, pp. 195–196, 1992.

[37] M. S. Dresselhaus, G. Dresselhaus, and P. C. Eklund, *Science of Fullerenes and Carbon Nanotubes*. New York, New York: Academic Press, 1996.

[38] H. Dai, "Carbon nanotubes: opportunities and challenges," *Surface Science*, vol. 500, no. 1-3, pp. 218–241, 2002.

[39] S. Iijima and T. Ichihashi, "Single-shell carbon nanotubes of 1-nm diameter," *Nature*, vol. 363, pp. 603–605, 1993.

[40] D. S. Bethune, C. H. Klang, M. S. de Vries, G. Gorman, R. Savoy, J. Vazquez, and R. Beyers, "Cobalt-catalysed growth of carbon nanotubes with single-atomic-layer walls," *Nature*, vol. 363, pp. 605–607, 1993.

[41] A. Thess, R. Lee, P. Nikolaev, H. Dai, P. Petit, J. Robert, C. Xu, Y. H. Lee, S. G. Kim, A. G. Rinzler, D. T. Colbert, G. E. Scuseria, D. Tomenek, J. E. Fischer, and R. E. Smalley, "Crystalline ropes of metallic carbon nanotubes," *Science*, vol. 273, no. 5274, pp. 483–487, 1996.

[42] S. Arepalli, P. Nikolaev, W. Holmes, and B. S. Files, "Production and measurements of individual single-wall nanotubes and small ropes of carbon," *Applied Physics Letters*, vol. 78, pp. 1610–1612, 2001.

[43] S. Farhat, I. Hinkov, and C. D. Scott, "Arc process parameters for single-walled carbon nanotube growth and production: Experiments and modeling," *Journal of Nanoscience and Nanotechnology*, vol. 4, no. 4, pp. 377–389, 2004.

[44] S. Arepalli, W. A. Holmes, P. Nikolaev, V. G. Hadjiev, and C. D. Scott, "A parametric study of single-wall carbon nanotube growth by laser ablation," *Journal of Nanoscience and Nanotechnology*, vol. 4, no. 7, pp. 762–773, 2004.

[45] M. Jose-Yacaman, M. Miki-Yoshida, L. Rendon, and J. G. Santiesteban, "Catalytic growth of carbon microtubules with fullerene structure," *Applied Physics Letters*, vol. 62, no. 2, pp. 202–204, 1993.

[46] V. K. Varadan and J. Xie, "Large-scale synthesis of multi-walled carbon nanotube by microwave CVD," *Journal of Smart Materials and Structures*, vol. 11, no. 4, pp. 610–616, 2002.

[47] D. Park, Y. H. Kim, and J. K. Lee, "Synthesis of carbon nanotube on metallic substrates by a sequential combination of PECVD and thermal CVD," *Carbon*, vol. 41, pp. 1025–1029, 2003.

[48] R. Seidel, G. S. Duesberg, E. Unger, A. P. Graham, M. Liebau, and F. Kreupl, "Chemical vapor deposition growth of single-walled carbon nanotubes at 600 ^{0}C and a simple growth model," *Journal of Physical Chemistry B*, vol. 108, no. 6, pp. 1888–1893, 2004.

[49] H. Dai, "Nanotube growth and characterization," *Topics in Applied Physics*, vol. 80, pp. 29–53, 2001.

[50] T. W. Ebbesen (ed.), *Carbon Nanotube: Preparation and Properties*. Boca Raton, Florida: CRC Press, 1997.

[51] T. W. Ebbesen, P. M. Ajayan, H. Hiura, and K. Tanigaki, "Purification of nanotubes," *Nature*, vol. 367, p. 519, 1994.

[52] S. Gajewski, H. E. Maneck, U. Knoll, D. Neubert, I. Dorfel, R. Mach, B. Strauss, and J. F. Friedrich, "Purification of single walled carbon nanotubes by thermal gas phase oxidation," *Diamond Related Material*, vol. 12, no. 3-7, pp. 816–820, 2003.

[53] H. Hiura, T. W. Ebbesen, and K. Tanigaki, "Opening and purification of carbon nanotubes in high yields," *Advanced Material*, vol. 7, no. 3, pp. 275–276, 1995.

[54] L. Vaccarini, C. Goze, R. Aznar, V. Micholet, C. Journet, and P. Bernier, "Purification procedure of carbon nanotubes," *Synthetic Metals*, vol. 103, no. 1-3, pp. 2492–2493, 1999.

[55] H. Y. Kim, W. B. Choi, N. S. Lee, D. S. Chung, J. H. Kang, I. T. Han, J. M. Kim, M. H. Moon, and J. S. Kim, "Purification and characterization of single-walled carbon nanotubes," *Proceedings of Materials Research Society Symposium*, vol. 593, pp. 123–127, 2000.

[56] S. Bandow, A. Rao, K. A. Williams, A. Thess, R. E. Smalley, and P. C. Eklund, "Purification of single-wall carbon nanotubes by microfiltration," *Journal of Physical Chemistry B*, vol. 101, no. 44, pp. 8839–8842, 1997.

[57] A. G. Rinzler, J. Liu, P. Nikolaev, C. B. Huffman, F. J. Rodriguez-Macias, P. J. Boul, A. H. Lu, D. Heymann, D. T. Colbert, R. S.Lee, J. E. Fischer, A. M. Rao, P. C. Eklund, and R. E. Smalley, "Large scale purification of single wall carbon nanotubes: process, product and characterization," *Applied Physics A*, vol. 67, no. 1, pp. 29–37, 1998.

[58] C. Xu, E. Flahaut, S. R. Bailey, G. Brown, J. Sloan, K. S. Coleman, V. C. Williams, and M. L. H. Green, "Purification of single-walled carbon nanotubes grown by a chemical vapor deposition (CVD) method," *Chem. Res. Chinese Univ.*, vol. 18, no. 2, pp. 130–132, 2002.

[59] L. P. Biro, N. Q. Khanh, Z. Vertesy, Z. E. Horvath, Z. Osvath, A. Koos, J. Gyulai, A. Kocsonya, Z. Konya, X. B. Zhang, G. V. Tendeloo, A. Fonseca,

and J. B. Nagy, "Catalyst traces and other impurities in chemically purified carbon nanotubes grown by CVD," *Materials Science and Engineering C*, vol. C19, no. 1-2, pp. 9–13, 2002.

[60] E. Dujardin, T. W. Ebbesen, A. Krishnan, and M. M. J. Treacy, "Purification of single-shell nanotubes," *Advanced Materials*, vol. 10, no. 8, pp. 611–613, 1998.

[61] K. B. Shelimov, R. O. Esenaliev, A. G. Rinzler, C. B. Huffman, and R. E. Smalley, "Purification of single-wall carbon nanotubes by ultrasonically assisted filtration," *Chemical physics letters*, vol. 282, no. 5-6, pp. 429–434, 1998.

[62] A. R. Harutyunyan, B. K. Pradhan, J. Chang, G. Chen, and P. C. Eklund, "Purification of single-wall carbon nanotubes by selective microwave heating of catalyst particles," *Journal of Physical Chemistry B*, vol. 106, no. 34, pp. 8671–8675, 2002.

[63] C.-J. Ko, C.-Y. Lee, F.-H. Ko, H.-L. Chen, and T.-C. Chu, "Highly efficient microwave-assisted purification of multiwalled carbon nanotubes," *Microelectronic engineering*, vol. 73-74, pp. 570–577, 2004.

[64] R. Saito, M. Fujita, G. Dresselhaus, and M. S. Dresselhaus, "Electronic structure of chiral graphene tubules," *Applied Physics Letters*, vol. 60, no. 18, pp. 2204–2206, 1992.

[65] R. H. Baughman, A. A. Zakhidov, and W. A. de Heer, "Carbon nanotubes-the route toward applications," *Science*, vol. 297, pp. 787–792, 2002.

[66] J. W. G. Wildoer, L. C. Venema, A. G. Rinzler, R. E. Smalley, and C. Dekker, "Electronic structure of atomically resolved carbon nanotubes," *Nature*, vol. 391, pp. 59–62, 1998.

[67] M. Terrones, "Science and technology of the twenty-first century: synthesis, properties, and applications of carbon nanotubes," *Annual Review of Materials Research*, vol. 33, pp. 419–501, 2003.

[68] M. S. Dresselhaus, P. C. Eklund, and R. Saito, "Carbon nanotubes," *Physics World*, vol. 33, 1998.

[69] S. Louie, "Electronic properties, junctions, and defects of carbon nanotubes," *Topics in Applied Physics*, vol. 80, pp. 113–146, 2001.

[70] P. G. Collins, M. S. Arnold, and P. Avouris, "Engineering carbon nanotubes and nanotube circuits using electrical breakdown," pp. 706–709, 2001.

[71] R. Krupke, F. Hennrich, H. V. Lohneysen, and M. M. Kappes, "Separation of metallic from semiconducting single-walled carbon nanotubes," *Science*, vol. 301, pp. 344–347, 2003.

[72] S. Banerjee, T. Hemraj-Benny, and S. S. Wong, "Routes towards separating metallic and semiconducting nanotubes," *Journal of Nanoscience and Nanotechnology*, vol. 5, no. 6, pp. 841–855, 2005.

[73] W. Liang, M. Bockrath, D. Bozovic, J. H. Hafner, M. Tinkham, and H. Park, "Fabry - perot interference in a nanotube electron waveguide," *Nature*, vol. 411, pp. 665–669, 2001.

[74] C. Berger, P. Poncharal, Y. Yi, and W. de Heer, "Ballistic conduction in multiwalled carbon nanotubes," *Journal of Nanoscience and Nanotechnology*, vol. 3, no. 1-2, pp. 171–177, 2003.

[75] B. Q. Wei, R. Vajtai, and P. M. Ajayan, "Reliability and current carrying capacity of carbon nanotubes," *Applied Physics Letters*, vol. 79, pp. 1172–1174, 2001.

[76] M. Kociak, A. Y. Kasumov, S. Guron, B. Reulet, I. I. Khodos, Y. B. Gorbatov, V. T. Volkov, L. Vaccarini, and H. Bouchiat, "Superconductivity in ropes of single-walled carbon nanotubes," *Physcial Review Letters*, vol. 86, no. 11, pp. 2416–2419, 2001.

[77] J. Zhao and R.-H. Xie, "Electronic and photonic properties of doped carbon nanotubes," *Journal of Nanoscience and Nanotechnology*, vol. 3, no. 6, pp. 459–478, 2003.

[78] N. Koratkar, A. Modi, J. Kim, B. Wei, R. Vajtai, S. Talapatra, and P. Ajayan, "Mobility of carbon nanotubes in high electric fields," *Journal of Nanoscience and Nanotechnology*, vol. 4, no. 1-2, pp. 69–71, 2004.

[79] E. W. Wong, P. E. Sheehan, and C. M. Lieber, "Nanobeam mechanics: Elasticity, strength, and toughness of nanotubes and nanorods," *Science*, vol. 277, no. 5334, pp. 1971–1975, 1997.

[80] M. F. Yu, O. Lourie, M. J. Dyer, K. Moloni, T. F. Kelly, and R. S. Ruoff, "Strength and breaking mechanism of multiwalled carbon nanotubes under tensile load," *Science*, vol. 287, no. 5453, pp. 637–640, 2000.

[81] M. F. Yu, B. S. Files, S. Arepalli, and R. S. Ruoff, "Tensile loading of ropes of single wall carbon nanotubes and their mechanical properties," *Physics Reivew Letter*, vol. 84, no. 24, pp. 5552–5555, 2000.

[82] J. Hone, M. C. Llaguno, N. M. Nemes, A. T. Johnson, J. E. Fischer, D. A. Walters, M. J. Casavant, J. Schmidt, and R. E. Smalley, "Electrical and thermal transport properties of magnetically aligned single wall carbon nanotube films," *Applied Physcis Letters*, vol. 77, pp. 666–668, 2000.

[83] J. Hone, B. Batlogg, Z. Benes, A. T. Johnson, and J. E. Fischer, "Quantized phonon spectrum of single-wall carbon nanotubes," *Science*, vol. 289, pp. 1730–1733, 2000.

[84] W. Yi, L. lu, D.-L. Zhang, Z. W. Pan, and S. S. Xie, "Linear specific heat of carbon nanotubes," *Physical Review B*, vol. 59, no. 14, pp. R9015–R9018, 1999.

[85] A. Mizel, L. X. Benedict, M. L. Cohen, S. G. Louie, A. Zettl, N. K. Budraa, and W. P. Beyermann, "Analysis of the low-temperature specific heat of multiwalled carbon nanotubes and carbon nanotube ropes," *Physical Review B*, vol. 60, no. 5, pp. 3264–3270, 1999.

[86] P. Kim, L. Shi, A. Majumdar, and P. L. McEuen, "Thermal transport measurements of individual multiwalled nanotubes," *Physcial Review Letters*, vol. 87, no. 21, pp. 215 502(1–4), 2001.

[87] W. Zhang, Z. Zhu, F. Wang, T. Wang, L. Sun, and Z. Wang, "Chirality dependence of the thermal conductivity of carbon nanotubes," *Nanotechnology*, vol. 15, pp. 936–939, 2004.

[88] F. Pico, J. M. Rojo, M. L. Sanjuan, A. Anson, A. M. Benito, M. A. Callejas, W. K. Maser, and M. T. Martinez, "Single-walled carbon nanotube as electrodes in capacitors," *Journal of the Electrochemical Society*, vol. 151, no. 6, pp. A831–A837, 2004.

[89] P. Calvert, "Nanotube composites: A recipe for strength," *Nature*, vol. 399, pp. 210–211, 1999.

[90] H. Dai, J. H. Hafner, A. G. Rinzler, D. T. Colbert, and R. E. Smalley, "Nanotubes as nanoprobes in scanning probe microscopy," *Nature*, vol. 384, pp. 147–150, 1996.

[91] S. Ghosh, A. K. Sood, and N. Kumar, "Carbon nanotube flow sensors," *Science*, vol. 299, no. 5609, pp. 1042–1044, 2003.

[92] A. M. Fennimore, T. D. Yuzvinsky, W. Q. Han, M. S. Fuhrer, J. Cumings, and A. Zettl, "Rotational actuators based on carbon nanotubes," *Nature*, vol. 424, pp. 408–410, 2003.

[93] M. Sveningsson, R. E. Morjan, O. Nerushev, and E. E. B. Campbell, "Electron field emission from multiwalled carbon nanotubes," *Carbon*, vol. 42, no. 5, pp. 1165–1168, 2004.

[94] P. Serp, M. Corrias, and P. Kalck, "Carbon nanotubes and nanofibers in catalysis," *Applied catalysis A*, vol. 253, no. 2, pp. 337–358, 2003.

[95] J. Lawrence and G. Xu, "High pressure saturation of hydrogen stored by single-wall nanotubes," *Applied Physcis Letters*, vol. 84, no. 6, pp. 918–920, 2004.

[96] N. Sinha, J. Ma, and J. T. Yeow, "Carbon nanotube based sensors," *Journal of Nanoscience and Nanotechnology*, vol. 6, no. 3, pp. 573–590, 2006.

[97] A. Modi, N. koratkar, E. Lass, B. Wei, and P. Ajayan, "Miniaturized gas ionization sensors using carbon nanotubes," *Nature*, vol. 424, no. 6945, pp. 171–174, 2003.

[98] H. E. Romero, K.Bolton, A. Rosen, and P. Eklund, "Atom collision-induced resistivity of carbon nanotubes," *Science*, vol. 307, pp. 89–92, 2005.

[99] X. W. Tang, Y. Yang, W. Kim, Q. Wang, P. Qi, H. Dai, and L. Xing, "Measurement of ionizing radiation using carbon nanotube field effect transistor," *Physics in Medicine and Biology*, vol. 50, pp. N23–N31, 2005.

[100] E. Artukovic, M. Kaempgen, D. S. Hecht, S. Roth, and G. Gr1ner, "Transparent and flexible carbon nanotube transistors," *Nano Letter*, vol. 5, no. 4, pp. 757–760, 2005.

[101] B. J. Gerbi and F. M. Khan, "Measurement of dose in the buildup region using fixed separation plane-parallel ionization chambers," *Medical Physics*, vol. 17, pp. 17–26, 1990.

[102] J. A. Rawlinson, D. Arlen, and D. Newcombe, "Design of parallel plate ion chambers for buildup measurements in megavoltage photon beams," *Medical Physics*, vol. 19, pp. 641–648, 1992.

[103] B. Nilsson, A. Montelius, and P. Andreo, "A study of interface effects in ^{60}Co beams using a thin-walled parallel plate ionization chamber," *Medical Physics*, vol. 19, pp. 1413–1421, 1992.

[104] C. Soutis, "Carbon fiber reinforced plastics in aircraft construction," *Materials science and engineering A*, vol. 412, no. 1-2, pp. 171–176, 2005.

[105] T. Chen, W. Gong, and G. Liu, "Effects of fiber-types on braking behavior of carbon-carbon composites," *Materials science and engineering A*, vol. 441, no. 1-2, pp. 73–78, 2006.

[106] M. M. Rafi, A. Nadjai, and F. Ali, "Experimental testing of concrete beams reinforced with carbon FRP bars," *Journal of composite materials*, vol. 41, no. 22, pp. 2657–2673, 2007.

[107] Y. Hamada, W. Otsu, J. Fukai, Y. Morozumi, and O. Miyatake, "Anisotropic heat transfer in composites based on high-thermal conductive carbon fibers," *Energy*, vol. 30, pp. 221–233, 2005.

[108] R. I. Baxter, R. D. Rawlings, N. Iwashita, and Y. Sawada, "Effect of chemical vapor infiltration on erosion and thermal properties of porous carbon/carbon composite thermal insulation," *Carbon*, vol. 38, pp. 441–449, 2000.

[109] W. U. Laub, T. W. Kaulich, and F. N1sslin, "Energy and dose rate dependence of a diamond detector in the dosimetry of 4-25 MV photon beams," *Medical Physics*, vol. 24, no. 4, pp. 535–536, 1997.

[110] P. W. Hoban, M. Heydarian, W. A. Beckham, and A. H. Beddoe, "Dose rate dependence of a PTW diamond detector in the dosimetry of a 6 MV photon beam," *Physics in Medicine and Biology*, vol. 39, pp. 1219–1229, 1994.

[111] J. F. Fowler and F. H. Attix, *Radiation Dosimetry Vol. 2.* New York, New York: Academic, 1966.

[112] Y. Zhou, A. Gaur, S.-H. Hur, C. Kocabas, M. A. Meitl, M. Shim, and J. A. Rogers, "p-channel, n-channel thin film transistors and p-n diodes based on single wall carbon nanotube network," *Nano letters*, vol. 4, no. 10, pp. 2032–2035, 2004.

[113] N. V. Hieu, L. T. B. Thuy, and N. D. Chien, "Highly sensitive thin film NH_3 gas sensor operating at room temperature based on SnO_2/MWCNTs composite," *Sensors and Actuators B*, vol. 129, no. 2, pp. 888–895, 2008.

[114] Y. D. Lee, K.-S. Lee, Y.-H. Lee, and B.-K. Ju, "Field emission properties of carbon nanotube film using a spray method," *Applied Surface Science*, vol. 254, pp. 513–516, 2007.

[115] Z. Wu, Z. Chen, X. Du, J. M. Logan, J. Sippel, M. Nikolou, K. Kamaras, J. R. Reynolds, D. B. Tanner, A. F. Hebard, and A. G. Rinzler, "Transparent, conductive carbon nanotube films," *Science*, vol. 305, pp. 1273–1276, 2004.

[116] T. V. Sreekumar, T. Liu, S. Kumar, L. M. Ericson, R. H. Hauge, and R. E. Smalley, "Single-wall carbon nanotube films," *Chemistry of Materials*, vol. 15, pp. 175–178, 2003.

[117] M. A. Meitl, Y. Zhou, A. Gaur, S. Jeon, M. L. Usrey, M. S. Strano, and J. A. Rogers, "Solution casting and transfer printing single-walled carbon nanotube films," *Nano Letters*, vol. 4, pp. 1643–1647, 2004.

[118] D. Stauffer and A. Aharony, *Introduction to Percolation Theory*. London, Washngton, DC: Taylor & Francis, 1992.

[119] G. Deutscher, R. Zallen, and J. Adler, *Percolation Structures and Processes*. New York, New York: American Institute of Physics, 1983.

[120] C. H. Liu and S. S. Fan, "Nonlinear electrical conducting behavior of carbon nanotube networks in silicone elastomer," *Applied Physics Letters*, vol. 90, no. 4, pp. 041 905(1–3), 2007.

[121] F. Du, J. E. Fischer, and K. I. Winey, "Effect of nanotube alignment on percolation conductivity in carbon nanotube/ploymer composites," *Physical Review B*, vol. 72, no. 12, pp. 121 404(1–4), 2005.

[122] S. Kumar, J. Y. Murthy, and M. A. Alam, "Percolating conduction in finite nanotube networks," *Physical Review Letters*, vol. 95, no. 6, pp. 066 802(1–4), 2005.

[123] L. Hu, D. S. Hecht, and G. Grner, "Percolation in transparent and conducting carbon nanotube networks," *Nano Letters*, vol. 4, no. 12, pp. 2513–2517, 2004.

[124] G. S. May and C. J. Spanos, *Fundamentals of Semiconductor Manufacturing and Process Control*. Hoboken, New Jersey: John Wiley & Son, Inc, 2006.

[125] J. Donald C. Thelen and D. D. Chu, "A low noise readout detector circuit for nanoampere sensor applications," *IEEE Journal of Solid-State Circuits*, vol. 32, no. 3, pp. 337–348, 1997.

[126] M. Breten, T. Lehmann, and E. Bruun, "Integration data converters for picoampere currents from electrochemical transducers," *Proceedings of*

IEEE International Symposium on Circuit and Systems (ISCAS 2000), pp. V709–712, 2000.

[127] Texas Instruments, "ACF2101 low noise dual switched integrator," 2008, http://www.ti.com/.

[128] ——, "OPA241 Single-supply micropower operational amplifiers," 2008, http://www.ti.com/.

[129] ——, "ADS8509 16-bit 250-ksps serial CMOS sampling analog-to-digital converter," 2008, http://www.ti.com/.

[130] Atmel, "ATmega8 8-bit AVR with 8K bytes in-system programmable flash," 2008, http://www.atmel.com/.

[131] Maxim, "MAX232A +5V-powered multichannel RS-232 drivers/receivers," 2008, http://www.maxim-ic.com/.

[132] Texas Instruments, "uA7800 series positive-voltage regulators," 2008, http://www.ti.com/.

[133] Microchip, "TC7662A charge pump DC-to-DC converter," 2008, http://www.microchip.com/.

[134] ON Semiconductor, "MC14028B BCD-to-decimal decoder/binary-to-octal decoder," 2008, http://www.onsemi.com/.

[135] Texas Instruments, "CD4069UB CMOS hex inverter," 2008, http://www.ti.com/.